SENSITIVITY TO ARROYO DEVELOPMENT SCENARIOS: INSIGHTS FROM A DISTRIBUTED HYDROLOGIC MODEL

by

Robert Louis Wyckoff

Submitted in partial fulfillment of the requirement for the

Degree of Master of Science in Hydrology

Department of Earth and Environmental Sciences

New Mexico Institute of Mining and Technology

Socorro, NM

December 2007

ABSTRACT

Rainfall-runoff relationships in semi-arid environments are highly non-linear due to the spatial and temporal variability of precipitation and watershed antecedent soil moisture conditions. Specifically within dryland regions, precipitation is often short in duration, limited in spatial extent, and characterized by high intensities. When combined with seasonal periods of elevated basin wetness, rainfall in semi-arid watersheds can lead to large flood and flash flood events within ephemeral channels. Because channel network geomorphology strongly influences flood wave generation and propagation in semi-arid watersheds, it is important to understand geomorphologic controls on streamflow behavior for both flood forecasting and water resources management. Specifically, semi-arid channel networks have experienced rapid geomorphological change that can significantly impact the timing, peak magnitude, and duration of flood events.

As an example, during the initial incision stage of arroyo development, streams cut downward through the valley alluvium forming deep, narrow channel networks. Down-cutting through valley fill increases arroyo cross sectional area, thus allowing flood transmission through the channel network without incurring discharge losses to overbank flow. In addition, upslope extension of the channel network head results in the dissection of watershed terrain. The increase in arroyo drainage density reduces overland

runoff path lengths and concentrates hillslope runoff in the channel network, which can lead to progressively larger flood events.

Furthermore, during the latter stages of arroyo development, establishment of riparian vegetation on the inner floodplain promotes arroyo stability. Vegetative root systems anchor streambank sediments and also increase the resistance to streamflow along channel margins. As flood waves interact with vegetation, sediment deposition occurs and the arroyo network narrows and aggrades thereby increasing the propensity for overbank flow. Consequently, observed flood events may decrease in magnitude once arroyos shift from a generally down-cutting and widening phase to a period of channel aggradation.

In this study, the TIN-based Real-time Integrated Basin Simulator (tRIBS) is used to simulate rainfall-runoff transformations and flood production within a large (> 1000 km^2) semi-arid watershed under different scenarios of arroyo development. In the initial phase of the study, model parameters are calibrated using observed stream gauge data from the Upper Río Puerco in northwestern New Mexico. Model calibration is focused on simulating flood events that developed in early September 2003 in response to widespread convective activity associated with the North American Monsoon.

Results for the calibration phase of the study demonstrate that the tRIBS model reproduces the major sequence of flood events observed in the Upper Río Puerco during September 2003 despite large uncertainties in calibrated soil parameter values and NEXRAD rainfall estimates (e.g, spatial and temporal resolution, absolute magnitude).

However, tRIBS does not consistently replicate time to peak discharge, peak discharge magnitudes, or rapid recession limb characteristics observed in the stream gauge discharge time series.

Following model calibration, parameters for the Upper Río Puerco tRIBS simulation are used in a series of modelling exercises designed to investigate streamflow response under different scenarios of arroyo development. Model simulations attempt to quantify changes in watershed flood production according to a conceptual hypothesis of arroyo development formulated from observations within Río Puerco watershed by *Elliott et al* (1999). Within a small test basin watershed (< 20 km^2), combinations of channel length, width, and roughness are used to simulate streamflow response to different phases of the arroyo geomorphological cycle. Following simulations in the test basin, model runs are performed in the Upper Río Puerco for similar variations in tRIBS channel network representation.

Results for model simulations that investigate different stages of arroyo incision reveal the greatest model sensitivity to changes in channel network length. Channel network extension associated with arroyo incision increases flood event magnitude and decreases time to peak. As arroyo headcuts migrate upslope, the distance to the channel decreases, which results in quick runoff arrival at the stream network. Once runoff is in the channel, longer stream networks efficiently route water to the basin outlet.

tRIBS model simulations that considered different parameterizations of channel roughness demonstrated a slight increase in peak discharge and a decrease in time to peak

for lower roughness values. However, for the basin scales and flood events explored in this study, model sensitivity to changes in channel roughness is limited. Likewise, the different channel width representations utilized in this study had minimal influence on simulated streamflow response. As a result, for this work, the effect of arroyo development is to magnify flood events primarily through the dissection of the watershed terrain with minor contributions from changes in channel roughness or width.

ACKNOWLEDGMENTS

Special thanks to my advisor, Dr. Enrique R. Vivoni, for his guidance during my studies at the New Mexico Institute of Mining and Technology. Additional thanks to Dr. John Wilson and Dr. Dave Love, who served on my thesis committee and provided contributions and inspiration that improved this M.S. thesis. Discussions with Alex Rinehart, Kinwai Tai, and Ricardo Mantilla provided intellectual stimulation that also enhanced this work.

Dr. Hongjie Xie supplied the GIS NEXRAD dataset instrumental to modelling efforts performed within this study. High resolution streamflow estimates provided by Robert Gold and Phillip Bowman at the Albuquerque United States Geological Survey (USGS) were also greatly appreciated.

Finally, I could not have completed this work without the encouragement and support offered by my family and Kelly Donahue.

TABLE OF CONTENTS

LIST OF FIGURES

LIST OF TABLES

This thesis is accepted on behalf of the
Faculty of the Institute by the following committee:

_____

Advisor

_____

_____

_____

_____

_____

Date

I release this document to the New Mexico Institute of Mining and Technology.

_____

Student's Signature Date

CHAPTER 1 - INTRODUCTION

Semi-arid watersheds demonstrate interrelated variability in stream channel geomorphological properties and flood wave characteristics at multiple time scales. At smaller time intervals (i.e., hours to days), large flood and flash-flood events quickly turn dry ephemeral channels into flowing rivers capable of transporting significant discharge volumes through watershed drainage networks (*Shannon et al*., 2002). Heightened streamflow imparts added shear stresses on channel walls and may lead to an increase in channel cross sectional area through lateral streambank erosion and streambed trenching (*Simon and Darby*, 1999; *Hooke and Mant*, 2000*; Coppus and Imeson*, 2002). Furthermore, sediment deposition downstream from the point of erosion can substantially impact channel network geomorphology and streamflow conveyance (*Coppus and Imeson*, 2002). Consequently, particular sections of the stream network may undergo erosion while other reaches experience streambed aggradation.

While individual flood events may alter localized reaches of channel networks, widespread changes in stream network geomorphology occur over time scales of years to centuries with significant implications for regional flood generation and propagation. For example, during the mid-to-late 1800s widespread arroyo development occurred throughout many watersheds in the southwestern United States (*Cooke and Reeves*, 1976). As networks cut downward through valley alluvium, stream channels

accommodated progressively larger flow volumes, sediment-transport capacities, and peak discharges (*Elliott et al.*, 1999; *Simon and Darby*, 1999). Additionally, channel network extension and gully formation caused an overall increase in network drainage density (*Bull and Kirkby*, 2002). For example, *Peterson* (1950) noted that the San Simon Creek located in southern Arizona increased 70 miles in length over a span of 44 years following arroyo incision. Similar dissection of watershed terrain across much of the southwestern Untied States has led to a decrease in average hillslope path lengths, which can also contribute to high magnitude flood events (*Bull and Kirkby*, 2002).

In response to pervasive arroyo development, researchers have attempted to formulate explanations for the primary causes of channel incision (*Rich*, 1911; *Bryan*, 1925; *Peterson*, 1950; *Leopold* 1951a; *Leopold*, 1951b*; Schumm and Hadley*, 1957). The majority of explanations attribute arroyo formation to at least one (or a combination) of the following phenomenon: climate change, vegetation or land use change, large flood events, and intrinsic geomorphic threshold factors (*Schumm*, 1999; *Bull and Kirkby, 2002*). Despite the attention paid to the causal mechanisms of network incision in the southwestern United States, little focus has been placed on the changes in streamflow behavior associated with arroyo development.

Understanding streamflow response to regional network incision is important in both a scientific and resources management context since arroyo development impairs agricultural land, increases fluvial sediment loads, and leads to larger flood generation. During the latter half of the 19th century, agricultural lands were degraded as headcuts migrated across the landscape. Whereas overbank flow formerly provided natural crop

irrigation, incised networks retained larger streamflow volumes due to the increased height of channel walls (*Bryan*, 1925; *Antevs*, 1952; *Schumm*, 1999). Incised networks also cause the deterioration of water quality and reduction of aquatic biodiversity due to increased sediment concentrations (*Shields et al.*, 1998). In addition, the nature of streamflow magnitude, volume, and timing within degraded channel networks is significantly altered. Whereas rainfall events previously caused extended low-magnitude flow events, incised river networks focus runoff into the channel network leading to increased flood magnitudes over shorter streamflow durations (*Antevs*, 1952). The reduction in hillslope length may further lead to higher runoff ratios for precipitation events with similar intensities, duration, and spatial extent. Thus, the changing nature of flood events and increased sediment concentrations associated with incised semi-arid channel networks could negatively impact communities that rely on surface water as an agricultural and municipal resource.

In this study, the physically-based TIN-based Real-time Integrated Basin Simulator (tRIBS) hydrological model is applied to the Upper Río Puerco watershed in northwestern New Mexico. The Upper Río Puerco is selected for study because of three primary factors: (1) its size (> 1000 km^2) does not impose excessive computational demands within a modelling context; (2) USGS stream gauge observations are available at a location near the watershed outlet for comparison with model results; and (3) the watershed possesses a history of incision dynamics. The initial phase of the study examines whether tRIBS can accurately replicate a series of monsoon flood events that occurred in the Upper Río Puerco during the first two weeks of September 2003.

Following model calibration, parameter values are used in a series of simulations designed to investigate streamflow behavior within different stages of arroyo development. Numerical experiments follow a conceptual hypothesis of arroyo development initially proposed by *Elliott* (1979) and expanded by *Elliott et al*. (1999).

Within the *Elliott et al*. (1999) arroyo evolutionary hypothesis, stream channels begin as non-incised networks. Vertical incision occurs in response to any system perturbation that causes either an increase in stream power or a decrease in sedimentary resistance to erosional forces (*Bull and Kirkby*, 2002). The arroyo incision stage is followed by a period of channel widening. Increased sediment loads associated with the mass wasting of channel walls supply sediment volumes greater than the transport-capacity of the arroyo network. In-channel sediment deposition leads to the sequence's inner floodplain development stage. As riparian vegetation is established on the inner floodplain, the decrease in frictional forces and increase in form drag due to flood wave interaction with plant biomass reduces streamflow velocity (*Griffin et al*., 2005). The reduction in velocity limits erosional forces on stream bank sediments and promotes a depositional environment (*Simon and Darby*, 1999). This phase of the arroyo development conceptual model is called the channel and inner floodplain stabilization stage. In the final stage of the sequence, the inner floodplain and arroyo streambed aggrade to levels slightly below the pre-incision valley floor.

Distributed physically-based models such as tRIBS, provide an opportunity for quantifying streamflow response to the large-scale arroyo evolution hypothesis presented by *Elliott et al.* (1999) through the explicit representation of channel network properties.

In this study, numerical experiments concurrently vary total channel length, channel width, and channel roughness as a method of investigating streamflow response to variable arroyo network geomorphology. Initial channel length estimates are based upon visual comparisons between a Geographic Information System (GIS) derived drainage network and observed watershed drainage density in 1 m orthophotographs. Streamflow response to network extension is examined through applied variations in total network length. Initial channel widths used in the tRIBS simulations are based upon GIS measurements of channel cross sections in orthophotographs. Both wider and narrower channel width representations are then used within different numerical experiments depending on the specific phase of arroyo development. Different values of Manning's roughness coefficient approximate variability in channel roughness due to changes in network geometry and potential floodwave interaction with riparian vegetation. Roughness values are selected based upon tRIBS model calibration and field measurements for different arroyo networks found in the literature.

The remainder of this study adheres to the following format. Chapter 2 briefly discusses distributed hydrologic modelling before describing components of the tRIBS model that are especially relevant to this study. Chapter 3 provides basin description for the Upper Río Puerco watershed. Chapter 3 also includes a more detailed discussion of the *Elliott et al.* (1999) conceptual model of arroyo development as well as the hydrometeorological conditions that led to the September 2003 flood event in the Upper Río Puerco. Chapter 4 discusses tRIBS model setup, results following calibration, and interpretations. Chapter 5 presents the numerical experimental approach for testing the

arroyo incision hypothesis in a small test watershed as well as the Upper Río Puerco. Discussion of these results also takes place in Chapter 5. Chapter 6 presents conclusions and future work.

CHAPTER 2 - MODEL INTRODUCTION AND DESCRIPTION

2.1 Introduction

In 1969, Freeze and Harlan unveiled their prototype for a physically-based, distributed, hydrologic model utilizing coupled nonlinear partial differential equations for both saturated and unsaturated flow (*Beven*, 2001*; Loague and Vanderkwaak*, 2004). At the time, Freeze and Harlan offered an alternative to the lumped-systems rainfall-runoff modelling approach, which characterized watersheds through "black box" empirical techniques (*Freeze and Harlan*, 1969). Over the subsequent 30 years, many distributed hydrologic modellers have followed the Freeze and Harlan blueprint and, with advancing computer capabilities, distributed models have added increasingly sophisticated hydrologic process representations (e.g., solute transport, sediment erosion, snowmelt runoff) (*Jakeman and Hornberger*, 1993; *Ebel and Loague*, 2006; *Liston and Elder*, 2006). However, despite additional complexity, distributed models still remain an alternative to lumped-systems modelling for hydrologic prediction and analysis (*Ivanov et al.*, 2004b).

Unlike a distributed approach, lumped parameter models utilize state variables to depict average basin hydrologic properties and preserve mass balance through the

transfer of mass fluxes between interconnected reservoirs (*Wagener et al.*, 2001; *Reggiani and Schellekens*, 2003). Although lumped parameter models reliably predict integrated catchment response in the form of an outflow hydrograph, basin dynamics are not resolved in sufficient detail to capture the watershed's internal nonlinear response to precipitation (*Jakeman and Hornberger*, 1993; *Ebel and Loague*, 2006). Nevertheless, lumped hydrologic models remain a viable option for addressing flood predictions especially when long streamflow records are available for model calibration.

In contrast, distributed hydrologic models attempt to explicitly characterize the inherent spatial and temporal variability of a watershed's response to meteorological forcing. The rainfall-runoff transformation process is approximated through physically-based mathematical representations of both surface and subsurface hydrologic processes (*Beven*, 1989, 2006; *Grayson et al.*, 1992a; *Ivanov et al.*, 2004a). In order to accurately simulate the various hydrologic components necessary for reproducing detailed catchment response, distributed models discretize the computational domain into numerous individual elements. Within each element, equations are solved for both the required state variables and fluxes exchanged between adjacent model elements (*Freeze and Harlan*, 1969; *Beven*, 1989; *Reggiani and Schellekens*, 2003).

Despite characterizing internal watershed dynamics, distributed models possess interrelated problems including overparameterization, application of point-scale non-linear equations to larger computational model-elements, and different viable parameter sets leading to equally acceptable model results (or equifinality) (*Beven*, 2001). As a result of parameter uncertainty issues, models typically undergo calibration exercises

until an acceptable match between model output and a catchment metric (e.g., watershed outlet hydrograph) is reached. However, achieving agreement in terms of integrated watershed response does not directly imply correct representation of internal basin physics. In fact, the general lack of overwhelming success in predicting watershed hydrologic response suggests that distributed models fail to properly quantify many aspects of internal catchment response to precipitation (*Grayson et al.*, 1992b). Consequently, distributed models are frequently disregarded in favor of simpler lumped-systems approaches.

Despite these potential drawbacks, distributed models can lead to greater hydrologic understanding as a hypothesis testing tool. For example, streambed infiltration, hillslope runoff reinfiltration, soil crusting and cracking, vegetative photosynthetic response, and variation in stream channel properties within a given storm event (e.g., active width, depth, and channel roughness) may be important components governing the total semi-arid watershed response to precipitation. Distributed models allow the explicit representation of watershed dynamics, evaluation of basin sensitivity to different hydrologic processes, and the opportunity to identify concepts requiring improved characterization through additional field study and data collection. In this study, the tRIBS (Triangulated Irregular Network based Real-time Integrated Basin Simulator) is utilized to investigate runoff generated during a large monsoon runoff event as well as model sensitivity to variation in channel roughness, channel length, and channel width within a large semi-arid watershed.

2.2 Model Description

tRIBS is a fully distributed hydrologic model that simulates unsaturated soil moisture redistribution through the development of infiltration fronts within the vadose zone (*Ivanov et al.*, 2004a). The model couples a single moving infiltration wave with a variable groundwater surface to depict soil moisture transfers between the unsaturated and saturated subsurface. Topographic representation within the model is implemented using a Triangulated Irregular Network (TIN), which allows significant computational savings especially when modelling large watersheds (e.g., > 100 km^2). In response to rainfall forcing, tRIBS simulates distributed catchment hydrologic processes including canopy interception, evapotranspiration, infiltration, soil moisture redistribution, hillslope runoff, and channel flow (Figure 2.1). The following sections describe tRIBS model components relative to this study. The reader is referred to *Ivanov* (2002) and *Ivanov et al.* (2004a, 2004b) for a complete review of model development.

2.3 Topographic Representation through Triangulated Irregular Networks

Topography is one of the principal controlling factors dictating both the nature of runoff at the hillslope scale and the resultant watershed response to precipitation (*Bogaart and Troch*, 2006). Thus, incorporating correct topography within a distributed model framework is essential for accurate simulation of rainfall-runoff processes (*Vivoni et al.*, 2004). Although high resolution terrain datasets are readily available, model domains with large spatial scales (e.g., 10^2 - 10^6 km^2) typically sacrifice detailed topography for reasonable simulation time by resampling data to coarser resolutions or generating

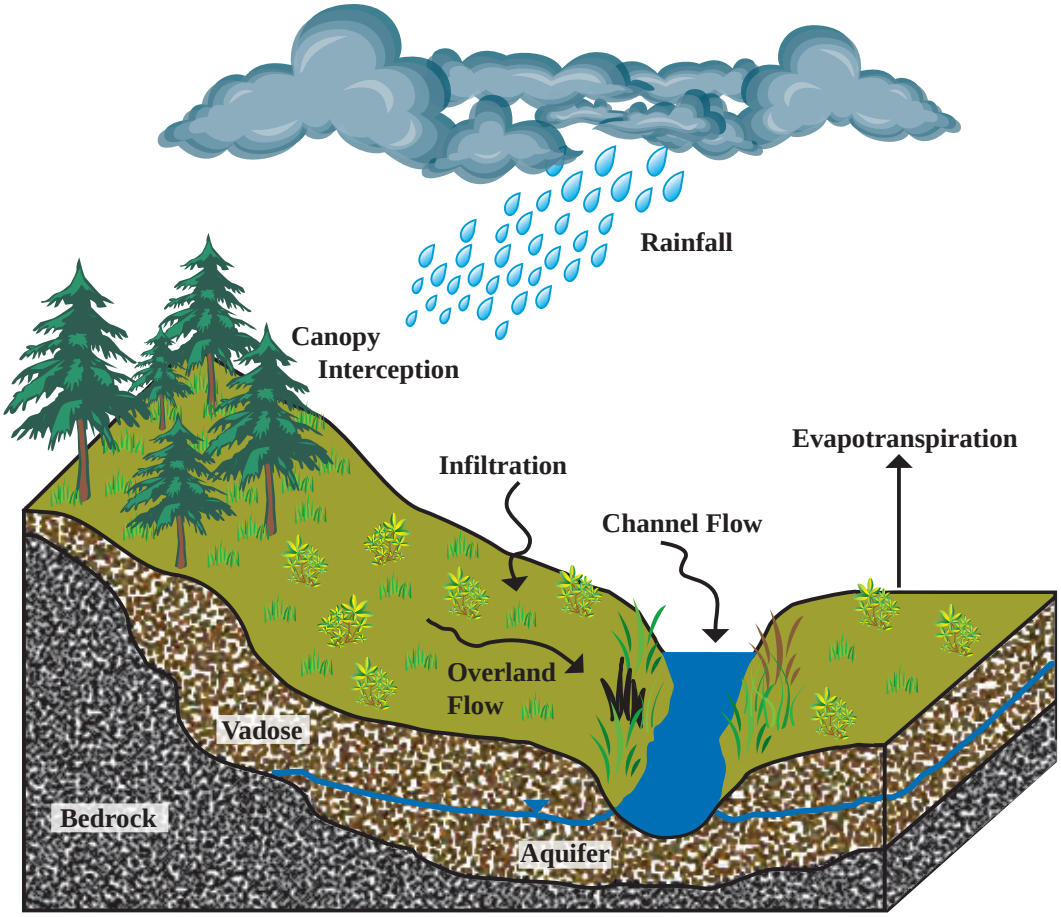

Figure 2.1 TIN-based Real-time Integrated Basin Simulator (tRIBS) conceptual representation of modelled hydrologic processes

topographic indices based upon elevation distribution (*Refsgaard et al.*, 1992; *Downer et al.*, 2002). Many of these data aggregation techniques significantly alter hydrologically important landscape properties including slope, aspect, and curvature (*Zhang and Montgomery*, 1994; *Kienzle*, 2004). Consequently, terrain representations utilized within the model domain no longer reflect existing catchment topography, which leads to incorrect representation of hydrological processes. Nonetheless, incorporation of model elements that retain important landscape characteristics within a distributed modelling framework is achievable. For example, *Vivoni et al.* (2004) demonstrated that

Triangulated Irregular Networks (TINs) successfully preserve the distribution of basin terrain features including slope and curvature.

A Triangulated Irregular Network (TIN) consists of a variable resolution triangular mesh and preserves significant watershed topographic features through the linear piecewise interpolation of Digital Terrain Models (DTMs) (*Nelson et al.*, 1999; *Vivoni et al.,* 2004). TINs possess the distinct advantage of representing terrain variability at multiple resolutions through the nonuniform distribution of triangle vertices (*Kumler,* 1994*; Nelson et al.*, 1999; *Vivoni et al.*, 2005). Regions of topographic variability and hydrological importance are resolved at high resolutions, while regions exhibiting less variability are characterized with reduced detail. Varying the resolution within the computational domain maximizes available computational resources while simultaneously maintaining important topographic features within the modelled catchment (*Goodrich et al.*, 1991). In Figure 2.2, regions of the DEM characterized by large distances between contour lines (e.g., plateaus) are represented in limited detail in the corresponding TIN. As the contour lines become tightly spaced, additional triangles are required within the TIN to capture the increase in terrain slope.

In order to generate a triangulated mesh, a sampling algorithm extracts point elevation values from a grid-based Digital Elevation Model (DEM). Various procedures are available for creating a subset of elevation data points including both the Drop Heuristic (DH) as well as the Very Important Point (VIP) method (*Kumler*, 1994). The DH slope-preserving method recursively samples the entire grid while ensuring each selected elevation point is within a certain specified vertical tolerance (Z_r) of the

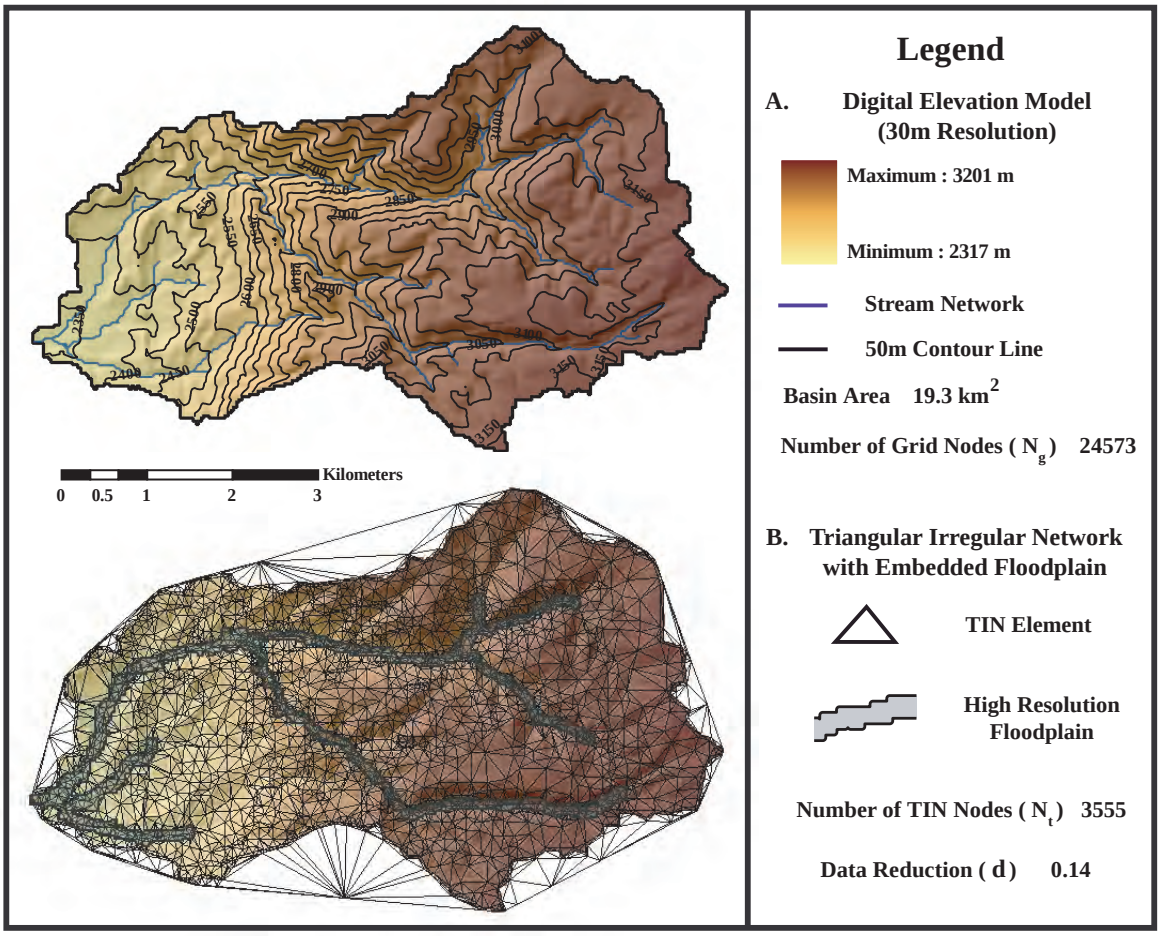

Figure 2.2 Resampling of a Digital Elevation Model to a Triangulated Irregular Network. (A) USGS 30m DEM overlying a GIS derived hillshade. Stream network generated through D-8 constant area threshold methodology; (B) TIN overlay derived from USGS 30m DEM with the Arcinfo Lattictin tool (Z_r = 10 m) including the high resolution floodplain embedded with the VIP procedure (v = 10 %).

corresponding DEM (*Lee*, 1991). Within ArcInfo GIS, the Latticetin command utilizes a modified version of the DH methodology. In contrast, the VIP method samples a 3x3 grid area and determines the significance of a specific node based upon the surface change along four transects passing through the central grid cell (*Lee*, 1991; *Kumler* 1994). For the VIP procedure, the triangular mesh retains a specified percentage (v) of the total number nodes present in the DEM. *Vivoni et al.* (2004) demonstrated that in comparison to the VIP methodology, the Latticetin (DH) approach produces a

topographic surface that accurately replicates hillslope transition to the valley floor, maintains triangles of similar size, and exhibits lower root mean square error (RMSE) when compared to the original DEM. For this study, watersheds are represented using the Latticetin methodology, while a high resolution floodplain is embedded within the triangulated mesh through the VIP procedure (Figure 2.2).

Once an elevation dataset is extracted from the original DEM, constrained Delaunay triangulation linearly connects each node to create a triangulated mesh (*Little and Shi*, 2001). Constrained triangulation ensures the preservation of naturally occurring breaklines including stream networks and the basin boundary (*Tsai*, 1993). The resultant TIN exhibits a substantial reduction in the overall number of nodes in comparison to the original DEM. The extent of terrain aggregation is captured through the horizontal point density (d) defined as:

$$d = \frac{n_t}{n_g}, \qquad 2.1$$

where n_t is the number of TIN nodes and n_g is the number of DEM nodes. As d approaches unity, the number of TIN nodes increases towards the total number of grid cells included within the DEM, thereby retaining detailed resolution throughout the model domain. Alternatively, as d decreases towards zero, terrain aggregation increases and TINs exhibit a coarse triangular mesh.

TIN structure and the degree of data aggregation are highly dependent on catchment terrain variability. Basins demonstrating large ranges in elevation (Δz) and high standard deviations (σ) require a greater number of TIN nodes per unit area than

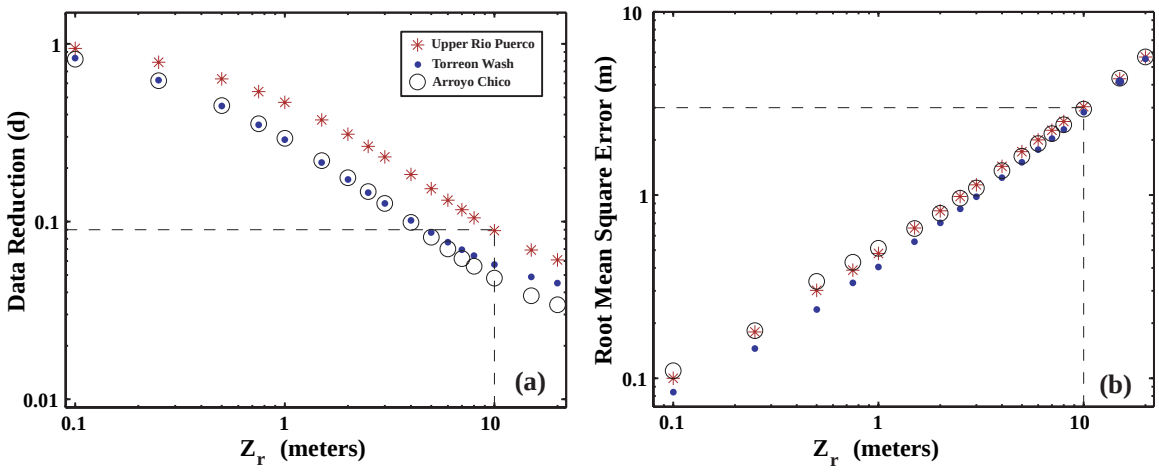

Figure 2.3 Data Reduction and Root Mean Square Variation As a Function of the Vertical Tolerance Parameter.

Table 2.1 DEM Characteristics for Three Semi-Arid Watersheds. *A* is basin area; *r* is DEM cellsize; n_g is the number of DEM grid cells; μ is the mean elevation; σ is the elevation standard deviation; Δ*z* is the elevation range

Watershed	A (km^2)	r (m)	n_g (#)	μ (m)	σ (m)	Δz (m)
Upper Río Puerco, NM	1118.61	28.04	1,422,546	1801.72	267.72	1422.86
Torreon Wash, NM	1334.13	28.04	1,709,336	2056.19	89.10	677.13
Arroyo Chico, NM	2220.68	28.04	2,824,061	2154.37	191.30	1439.30

watersheds exhibiting flatter topography. Figure 2.3a shows *d* as a function of vertical resolution (Z_r) across a series of TIN resolutions (Z_r values range from 0.1 m to 20 m) for three different semi-arid watersheds. To achieve the same proportion of data reduction (*d*), catchments with rugged terrain (e.g., Upper Río Puerco) require a higher vertical tolerance thus incorporating greater error within the land surface representation. As the range of elevation (Δ*z*) and standard deviation (σ) decreases, the terrain becomes more level (e.g., Torreon Wash) and less horizontal resolution is required for a given Z_r. For example, if Z_r is held constant at 10.0 m, Torreon Wash (Δ*z* = 677.13 m; σ = 89.10 m)

utilizes only 5.7% (d = 0.057) of the original DEM while the Upper Río Puerco (Δz = 1422.86 m; σ = 677.13 m) retains 8.9% (d = 0.089) of its respective DEM. This implies that watersheds exhibiting significant terrain heterogeneity require additional points for achieving a particular vertical tolerance in comparison to basins characterized by less irregular topography.

The root mean square error provides a metric for determining whether the TIN accurately represents watershed topography as compared to the original DEM:

$$\text{RMSE} = \sqrt{\frac{1}{N}\sum_{i=1}^{N}(z^i_{\text{DEM}} - z^i_{\text{TIN}})^2} \quad , \qquad 2.2$$

where z^i is the either the ith node of the DEM or the TIN and N is the total number of nodes selected from the DEM. As TINs utilize progressively higher vertical tolerances, error accumulates due to the loss of topographic accuracy and the RMSE subsequently increases (*Vivoni et al.,* 2005). In Figure 2.3b, the greatest error differences between watersheds occur at lower values of vertical tolerance (e.g., $Z_r \leq 1.5$ m). As TIN resolution decreases (e.g., $Z_r = 10$ m), RMSE values approach similar magnitudes despite inherent topographic and size differences across various watersheds.

2.4 tRIBS Computational Element Derivation Using Triangulated Irregular Networks

tRIBS employs a finite control volume approach to calculate both vertical fluxes departing a given cell as well as horizontal fluxes transferred between neighboring model elements (*Ivanov et al.,* 2004a). Computational cells in the form of Voronoi polygons

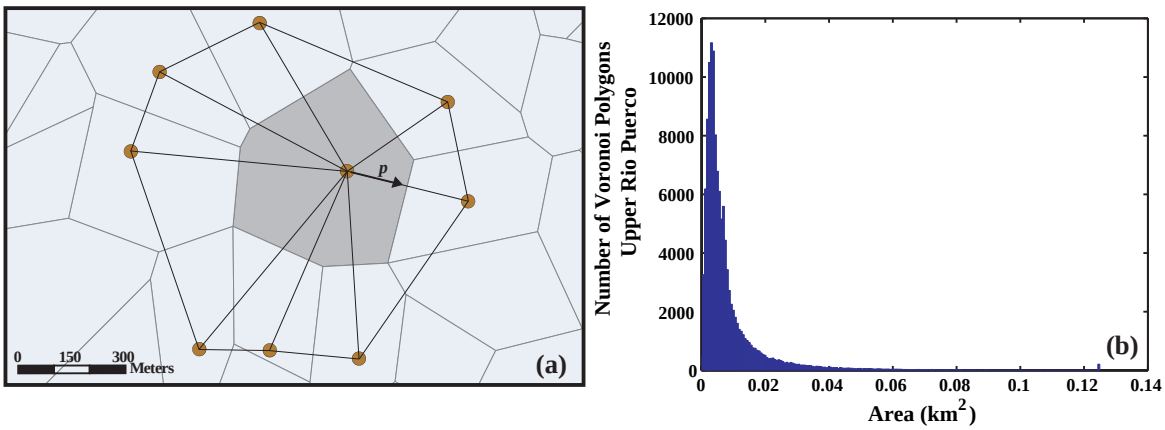

Figure 2.4 Voronoi Polygon and Area Histogram. (a) Voronoi polygon (dark grey fill), TIN edges (black lines) and Voronoi nodes (circles) used to construct Voronoi geometry. Path of steepest descent is defined by the directional arrow in the *p* direction. (b) Histogram demonstrating Voronoi area size distribution for the Upper Río Puerco. Figure 2.4a after *Ivanov et al. (*2004a).

(Figure 2.4a) are derived by connecting the extended perpendicular bisector of each TIN edge to form an irregular network of polygons (*Dingman*, 2002; *Ivanov et al.*, 2004a). Since the triangulated mesh provides the basis for Voronoi cell development, model computations occur for element sizes significantly larger than the original digital terrain model. As an example, a TIN with Z_r = 10 m for the Upper Río Puerco results in an average Voronoi polygon area of 8,952 m^2, whereas a DEM grid cell has a constant area of 786.2 m^2. Furthermore, the Voronoi cell size distribution is skewed towards the right (Figure 2.4b) resulting in a median tRIBS element area of 4,960 m^2 and a range of 478,400 m^2 (Table 2.2).

An additional method for comparing Voronoi polygon area and DEM grid size is to calculate an equivalent cell size (R_L) as:

$$R_L = \sqrt{\frac{A}{n_V}} \quad , \qquad 2.3$$

Watershed Representation Cell Area Statistics	C_A (m^2)	C_M (m^2)	n (#)	R_L (m)	σ_A (m^2)	ΔA (m^2)
Upper Río Puerco, DEM	786.2	786.2	1,422,546	28.04	0	0
Upper Río Puerco, Voronoi	8,952	4,960	124,420	94.82	13,688	478,400

Table 2.2 DEM and Voronoi Polygon Cell Size Comparisons. C_A is average cell area; C_M is the median cell area; n is the total number of nodes in the terrain model; R_L is an equivalent cell size if nodes were evenly distributed across basin area; σ_A is the cell area standard deviation; ΔA is the cell area range. Voronoi polygons derived from TIN with $Z_r = 10$.

where A is the basin area and n_V is the number of Voronoi nodes. R_L provides the model element edge length if the number of Voronoi nodes were distributed across a watershed and used to generate an evenly gridded terrain surface. As the number of Voronoi nodes approaches the number of TIN nodes, R_L approaches the value of the DEM cell width (*Tucker et al.,* 2001, *Vivoni et al.,* 2005). For the Upper Río Puerco, the equivalent grid length of each Voronoi polygon is ~95 m or approximately three times the edge length of the original DEM (Table 2.2).

As demonstrated in Figure 2.4a, Voronoi cells are defined in the direction of steepest descent across each individual model element (p) and the direction perpendicular to the plane of maximum slope (n) (*Ivanov,* 2002*; Ivanov et al.,* 2004a). One dimensional equations conserve mass in the n orientation, while fluxes between elements are calculated using the Voronoi cell edge length normal to the p direction (*Ivanov et al.,* 2004a). Runoff generated at a single node is routed to the stream network along triangle edges, which collectively define a pathway following the maximum hillslope gradient (*Tucker et al.,* 2001; *Ivanov et al.,* 2004a).

2.5 Review of Relevant Hydrologic Processes within tRIBS

Within the tRIBS model, physically-based mathematical representations of surface and subsurface processes are used to calculate horizontal and vertical hydrological fluxes for each Voronoi polygon. The following sections summarize important tRIBS model components including the evapotranspiration model, tRIBS infiltration and runoff mechanisms, and channel and hillslope runoff routing methodologies.

2.5.1 Rainfall Interception and Evapotranspiration

Evapotranspiration simulations include the canopy water balance representation introduced by *Rutter et al.* (1971 and 1975). The method attempts to reproduce changes in canopy storage (C) by allocating a proportion of rainfall into an interception term. Canopy drainage (D) and scaled potential evaporation (E_p) terms are then subtracted from rainfall intercepted by plant cover, yielding the canopy storage within a given time interval:

$$\frac{dC}{dt} = (1-p)R - D - \frac{C}{S}E_p \,, \qquad 2.4$$

where S is the canopy capacity, p is the free throughfall coefficient, and R is the rainfall rate. Canopy capacity (S) reflects the water remaining within the canopy structure following complete saturation and an extended period of drainage. Whereas C is a variable, S is regarded as an intrinsic property of the plant canopy (*Eltahir and Bras,* 1993). Drainage from canopy interception (D) implicitly accounts for both leaf drip and stemflow and is calculated as:

$$D = Ke^{g(C-S)}, \qquad 2.5$$

where K is a drainage rate coefficient and g is an exponential decay parameter (*Shuttleworth,* 1979; *Ivanov et al.,* 2004a). Parameters *p, S, K,* and *g* require calibration, values assigned from field data, or values found in the literature (*Eltahir and Bras,* 1993).

Precipitation that reaches the land surface is portioned into a throughfall and stemflow fraction as well as rainfall on bare soil. Within tRIBS, net precipitation (P_{Net}) is calculated as:

$$P_{Net} = v(pR + D) + (1 - v)R, \qquad 2.6$$

where v is the fraction of the voronoi polygon covered by vegetation (vegetative fraction). The first term in Equation 2.6 represents rainfall that reaches the land surface as a result of canopy throughfall or or canopy drainage. The second term in Equation 2.6 represents the proportion of rainfall that occurs over bare soil.

Evapotranspiration calculations are partitioned into evaporation from a wet canopy (E_{wc}), evaporation from bare soil (E_s), and plant transpiration (E_{dc}), which is conceptually similar to the procedure found in *Wigmosta et al.* (1994). tRIBS determines the latent heat flux (λE) at the ground surface with the Penman-Monteith approach and uses λE as an approximation for actual evaporation (E_a) (*Ivanov et al.,* 2004a). The Penman-Monteith model consists of an energy balance approach and mass transfer procedure designed to estimate evaporation from a soil surface by including surface and aerodynamic resistance terms:

$$\lambda E = \frac{\Delta(R_n - G) + \gamma \frac{\rho_m \lambda_v \delta q_a}{r_a}}{\Delta + \gamma(1 + \frac{r_s}{r_a})}, \qquad 2.7$$

where Δ is the slope of the Clausius-Clayperon relationship, R_n is is net radiation, G is ground heat flux, γ is the psychometric constant, ρ_m is the moist air density, λ_v is latent heat of vaporization, δq_a is specific humidity, r_a is the aerodynamic resistance, and r_s is the stomatal resistance (*Penman,* 1948; *Monteith,* 1965). The reader is referred to *Ivanov et al.* (2004a) for the net radiation and ground heat flux equations implemented in the tRIBS model.

The potential evaporation (E_p) term is expressed as:

$$E_p = E_a \left[\frac{\Delta + \gamma(1 + \frac{r_s}{r_a})}{\Delta + \gamma} \right], \qquad 2.8$$

where E_a is the actual evaporation and is equivalent to λE. Potential evaporation (E_p) is further used to calculate evaporation from bare soil (*Deardorff,* 1978):

$$E_s = (1 - v)\beta_e E_p, \qquad 2.9$$

where v is the vegetative fraction defined for the model element and β_e represents a soil moisture reduction factor for the near surface portion of the soil column:

$$\beta_e = \min(1, \frac{\theta_{100}}{0.75\theta_s}), \qquad 2.10$$

where θ_{100} is the soil moisture content within the top 100 mm of the soil surface and θ_s is the soil moisture at saturation (*Deardorff,* 1978). Multiplying θ_s by 0.75 provides an

approximate field capacity value for a given soil type. Field capacity is the soil water content retained against the force of gravity once drainage has reached an inappreciable rate (*Dingman*, 2002).

Evaporation rate from a wetted canopy (E_{wc}) depends upon the degree of saturation within the plant canopy:

$$\begin{aligned} E_{wc} &= vE_p,\ E_{dc} = 0,\ C \geq S \\ E_{wc} &= \frac{C}{S} vE_p,\ E_{dc} > 0,\ 0 \leq C \leq S \end{aligned} . \qquad 2.11$$

When canopy storage (C) is greater than the canopy capacity (S), evaporation occurs at the potential rate. If the canopy storage (C) is less than the canopy capacity (S), then the canopy maintains less moisture than its total potential and E_{wc} includes a fractional wetness term (C/S). Transpiration then occurs as:

$$E_{dc} = \beta_t (E_p - \frac{E_{wc}}{v}) \left[\frac{\Delta + \gamma}{\Delta + \gamma(1 + \frac{r_s}{r_a})} \right], \qquad 2.12$$

where β_t accounts for fluctuations in soil moisture content that lead to plant stress by imparting constraints on root soil water uptake (*Ivanov et al.*, 2004a). Equation 2.12 suggests that once the canopy layer reaches saturation, plant transpiration cannot occur. The transpiration stress factor β_t is represented as:

$$\beta_t = \min(1, \frac{\theta_{top} - \theta_r}{0.75\theta_s - \theta_r}), \qquad 2.13$$

where θ_{top} is the soil moisture content within the first meter of the soil column and θ_r is the residual soil moisture content for a particular soil texture (*Brooks and Corey*, 1964;

Ivanov et al., 2004a).

2.5.2 Infiltration and Runoff Mechanisms

Underlying Model Assumptions

Infiltration process representation relies upon the kinematic approximation for unsaturated soils found in *Cabral et al.* (1992). These conditions presuppose that gravitational forces dictate unsaturated flow mechanisms and any redistribution of soil moisture due to capillary pressure gradients is negligible (*Cabral et al.*, 1992; *Ivanov et al.*, 2004a). The directions both normal (*n*) and parallel (*p*) to the hillslope define flow orientation, however soil properties within a single model cell vary only in the direction perpendicular to the soil surface (*Cabral et al.*, 1992; *Ivanov et al.*, 2004a). Within a particular model element, saturated conductivity exponentially decreases with increasing soil column depth. *Beven* (1984) demonstrated that this approximation for non-uniform soils could adequately describe vertical heterogeneity with respect to hydraulic conductivity. Furthermore, a soil anisotropy ratio of parallel to normal hydraulic conductivities provides an approximation of soil layering (*Garrote and Bras*, 1995; *Ivanov et al.*, 2004a). tRIBS expands upon the *Cabral et al.* (1992) model and includes an effective wetting front capillary pressure component designed to simulate changes in soil moisture content across an infiltrating soil moisture pulse (*Ivanov et al.*, 2004a).

Infiltration Under Saturated Conditions due to Surface Ponding

Infiltration under ponded saturated conditions occurs whenever the rainfall rate (R) is greater than the hydraulic conductivity at the soil surface (K_{0n}) and is frequently modelled using the Green-Ampt equation (*Beven*, 2002a; *Downer et al.*, 2002). The original version of the Green-Ampt model assumes that a descending moisture wave maintains constant matric potential across its wetting front irrespective of time or location within the soil column (*Childs and Bybordi*, 1969; *Hillel*, 1998). The transitional region between the wetting front and unsaturated region of the soil profile is characterized by a distinct and level plane of separation (*Hillel*, 1998; *Ivanov,* 2002). Additionally, the saturated soil profile behind (above) the advancing moisture pulse is characterized by constant hydraulic conductivity and soil moisture content, while the entire soil column retains a uniform pore size distribution (*Hillel*, 1998; *Dingman*, 2002). As a result, the Green-Ampt model does not represent fingered infiltration patterns due to preferential flow paths.

tRIBS describes infiltration under ponded conditions using a modified version of the Green-Ampt equation found in *Childs and Bybordi* (1969) and *Beven* (1984):

$$q_n(N_f) = -K_{eff}\left[\frac{h_f(N_f)}{N_f} - 1\right] \qquad 2.14$$

where $q_n(N_f)$ is the infiltration rate normal to the hillslope, K_{eff} is the harmonic mean of conductivities for the saturated length, $h_f(N_f)$ is the effective capillary pressure head at the wetting front, and N_f is the wetting front depth (*Ivanov et al.*, 2004a). To account for compaction and the overall reduction of soil permeability with depth, K_{eff} is determined

as:

$$K_{eff}(N_f) = K_{0n}\frac{fN_f}{e^{fN_f}-1}, \qquad 2.15$$

where f is a dimensionless conductivity decay parameter and K_{0n} is the saturated conductivity in the direction normal to the land surface (*Ivanov*, 2002). Below the wetting front location, pore spaces remain unsaturated and consequently exhibit less than atmospheric pore pressures. The effective capillary pressure head $h_f(N_f)$, resulting from soil moisture values less than saturation, is expressed as:

$$h_f(N_f) = \psi_b \frac{1-S_{ei}^{3+\frac{1}{\lambda(N_f)}}}{3\lambda(N_f)+1}, \qquad 2.16$$

where ψ_b is the air entry bubbling pressure (*Ivanov et al.*, 2004a). In *Ivanov* (2002) the effective saturation (S_{ei}) is represented as:

$$S_{ei} = \frac{\theta(N_f)-\theta_r}{\theta_s-\theta_r}, \qquad 2.17$$

where $\theta(N_f)$ is the soil moisture content at the wetting front depth, θ_r is the residual soil moisture content, and θ_s is the soil moisture content at saturation (equivalent to the soil porosity). The pore size distribution index within the soil profile at the wetting front depth (λ) is represented as:

$$\lambda(N_f) = \lambda_0 e^{-\left(\frac{fN_f}{2}\right)}, \qquad 2.18$$

where λ_0 is the pore-size distribution index near the soil surface (*Ivanov et al.*, 2004a). If we rewrite Equation 2.14 as:

$$q_n(N_f) = -K_{eff}\frac{h_f(N_f)}{N_f} + K_{eff} \qquad 2.19$$

and allow

$$\psi_{is}(N_f) = -K_{eff}\frac{h_f(N_f)}{N_f}, \qquad 2.20$$

then ψ_{is} represents the infiltration hindrance due to negative pore pressures in the unsaturated zone. The second K_{eff} term in Equation 2.19 expresses the infiltrating flux due to the force of gravity alone (*Ivanov*, 2002). Finally, the direction perpendicular to the soil surface and the vertical direction corresponding to gravitational forces do not always coincide. Thus, to derive the flow vector normal to the hillslope, the model element angle (α) requires representation within the infiltration model:

$$q_n = K_{eff}(N_f)\cos\alpha + \psi_{is}(N_f), \qquad 2.21$$

where q_n is the infiltrating flux per unit area (*Ivanov et al.*, 2004a). Infiltration is modelled under ponded saturated conditions whenever the rainfall rate (R) is equal to or greater than q_n (*Ivanov,* 2002).

Infiltration Occurring Under Unsaturated Conditions

When the rainfall rate falls below the soil infiltration capacity, water redistribution within the soil column occurs under unsaturated conditions (*Cabral et al.*, 1992; *Ivanov et al.*, 2004a). Within the model, the conductivity decay parameter (*f;* Equation 2.14) dictates that water transmission in the vertical direction occurs rapidly at the soil surface in comparison to the soil water conductance rate deeper within the profile (*Cabral et al.*, 1992). If infiltration occurs over a sustained duration, a wetted wedge may develop with

an overlying region of unsaturated soil (*Cabral et al.*, 1992).

Provided the increase in soil moisture at depth does not generate a perched (where perched implies saturated) soil layer, tRIBS models infiltration fluxes under unsaturated conditions. To account for variation in rainfall, an equivalent rainfall rate (R_e) is defined as the constant intensity that leads to an identical moisture content within the unsaturated region of the soil column under steady-state conditions (*Garrote and Bras*, 1995; *Ivanov et al.*, 2004a). Because rainfall is redistributed over an entire time step, water infiltrating the model element contributes to the development of a single wetting front. If rainfall occurs over multiple time steps, infiltrating water supplements the already existing moisture wave. That is, tRIBS cannot simulate the progression of multiple independent moisture waves through the soil column. Determining R_e requires definitive soil moisture values at both the wetting front and the top front. The soil moisture profile is expressed as:

$$\theta(R,n) = \left(\frac{R}{K_{0n}}\right)^{\frac{1}{\varepsilon}} \left(\theta_s - \theta_r\right) e^{\frac{fn}{\varepsilon}} + \theta_r, \quad \text{for } 0 \le n \le N_f \qquad 2.22$$

where R is a constant rainfall rate, $\varepsilon = (2 + 3\lambda) / \lambda$, and n is depth perpendicular to the land surface (*Ivanov*, 2002). Equation 2.22 states that under equilibrium conditions, soil moisture above the wetting front decreases exponentially as soil depth (n) approaches the soil surface (*Cabral et al.*, 1992). Above the wetting front, the unsaturated conductivity, $K(N_f)$, is equivalent to R_e:

$$R_e = K_n(\theta,n)=K_{0n}\left(\frac{M_u-\theta_r N_f}{\frac{\varepsilon}{f}(\theta_s-\theta_r)(e^{\frac{fN_f}{\varepsilon}}-1)}\right)^{\varepsilon}, \qquad 2.23$$

where M_u is the moisture in the wetted wedge between the land surface and the depth of the wetting front. Using Equation 2.22, the unsaturated flow in the direction normal to the hillslope is expressed as:

$$\psi_{ie}(N_f,\theta_i,\theta_e)=-K_{sn}(N_f)\frac{h_f(N_f,\theta_i,\theta_e)}{N_f} \qquad 2.24$$

where ψ_{ie} is the matric suction gradient across the wetting front, θ_i is the moisture content at the wetting front depth (N_f) of the initial soil moisture profile, and θ_e is the maximum soil moisture value of the wetted wedge (*Ivanov*, 2002). Matric suction is calculated in a manner similar to Equations 2.16 through 2.18 but modified for unsaturated soils. The reader is referred to *Ivanov* (2002) for a more comprehensive description.

Perched Infiltration

If infiltration continues for a sufficient duration, the equivalent rainfall rate diminishes to the saturated conductivity value at the wetting front depth, N^* (*Ivanov*, 2002):

$$R_e = K_{sn}(N^*), \qquad 2.25$$

The location within the soil profile where soil saturation develops is:

$$N^*(R_e)=\frac{1}{f}\ln\left(\frac{K_{0n}}{R_e}\right), \qquad 2.26$$

where $N^*(R_e)$ is the depth of the perched layer (*Cabral et al.*, 1992). Similar to previous

calculations, the moisture flux in the normal direction occurs as:

$$q_n(N_f, N_t) = K_{eff}(N_f, N_t)\cos\alpha + \psi_{is}(N_f), \qquad 2.27$$

where N_t is the location of the top front, ψ_{is} is the matric suction used in Equation 2.20, and K_{eff} is the harmonic mean from saturation level up to the top front:

$$K_{eff}(N_f, N_t) = K_{0n}\frac{f(N_f - N_t)}{e^{fN_f} - e^{fN_t}}, \qquad 2.28$$

For a detailed description of the tRIBS infiltration model the reader is referred to *Cabral et al*., (1992), *Garrote and Bras* (1995), and *Ivanov* (2002).

Subsurface Moisture Transfer Between Voronoi Elements

Within tRIBS, the vertical and horizontal calculations for soil moisture redistribution occur independently, which allows for moisture flux accounting both above top front and below the wetting front (*Ivanov*, 2002). However, the kinematic assumptions discussed previously still remain when calculating horizontal fluxes. Lateral transmission of soil moisture occurs as:

$$Q = \sin\alpha\left[[N_t R_e(a_r - 1)] + [K_{0n}\frac{a_r}{f}(e^{-fNt} - e^{-fN_f})] - \left[K_{0n}\frac{f(N_f - N_t)^2}{e^{fN_f} - e^{fNt}}\right]\right], \qquad 2.29$$

where Q is the discharge per unit width from the unsaturated region of the Voronoi polygon and a_r is the ratio of the normal to perpendicular saturated conductivities (*Ivanov*, 2002). The reader is directed to *Ivanov* (2002) for additional discussion of subsurface soil moisture redistribution between model elements.

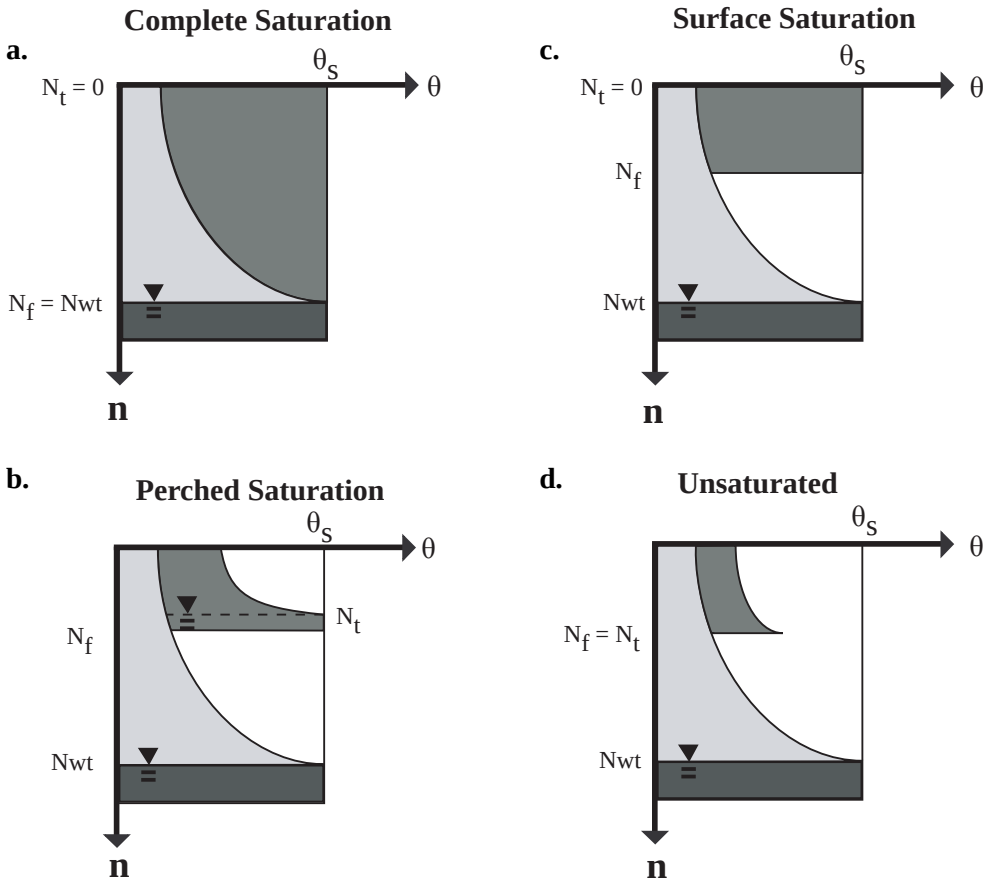

Figure 2.5 Potential tRIBS model element soil moisture profiles. Soil moisture profile at the time of runoff production determines whether overland flow is classified as saturation excess, infiltration excess, perched subsurface stormflow, or groundwater exfiltration. The lightest color gray represents the initial soil moisture profile. The medium gray represents different stages of wetting front (N_f) and top front (N_t) development. The darkest gray represents the position of the groundwater table (*Nwt*). From *Ivanov* (2002)

Runoff Mechanisms

tRIBS is capable of generating infiltration excess, saturation excess, perched subsurface storm flow, and groundwater exfiltration. Runoff type is determined by the soil moisture distribution within a particular model element. Four different soil moisture profiles are represented within tRIBS: (1) Complete Saturation; (2) Perched Saturation; (3) Surface Saturated; and (4) Unsaturated (Figure 2.5) (*Ivanov*, 2002).

Runoff due to completely saturated conditions occurs when the wetting front (N_f) reaches the water table (N_{wt}), while the top of the front (N_t) remains at the land surface (Figure 2.5a). Under this condition, the soil column is completely saturated and no longer possesses the ability to store additional soil moisture contributions. Any further rainfall that occurs once a Voronoi element reaches complete saturation results in saturation excess runoff.

Lateral subsurface soil moisture transfer between model elements may occur as subsurface flow from upstream model elements is routed to downstream cells. Perched return flow is generated whenever water is routed from an unsaturated model element to a downstream saturated cell and runoff is produced (Figure 2.5b). Groundwater exfiltration takes place if an upstream saturated pixel contributes soil moisture to a saturated downstream model element (*Ivanov*, 2002).

Surface saturation occurs when the top front is at the land surface but the wetting front remains above the water table (Figure 2.5c). This condition may emerge as soil moisture redistribution at depth slows due to the saturated hydraulic conductivity decay parameter. Return flow may be produced if inflow into the Voronoi polygon is greater than the outflow rate and the downward flux of moisture in the direction normal to the land surface (*Ivanov*, 2002).

Perched saturated flow may take place when the top of the wetting front is below the soil surface, while the bottom of the moisture wave is above the water table (Figure 2.5b). Consequently, a saturated lens develops within the model element. Perched

conditions may lead to saturated excess runoff production if the wetting front continues to expand and the top of the moisture wave reaches the soil surface. If the perched layer develops at the top of the soil column infiltration excess runoff may occur.

Runoff produced during unsaturated conditions occurs when the rainfall rate is greater than the vertical redistribution of water near the soil surface (Figure 2.5d). This type of runoff production is typically referred to as infiltration excess or Hortonian runoff. Infiltration excess runoff is often the primary mechanism considered for overland flow generation in semi-arid environments (*Beven*, 2002). This assumption has resulted in semi-arid watershed hydrologic models, including the MEDALUS slope catena model and CASC2D, that only generate runoff through infiltration excess mechanisms (*Beven*, 2002; *Downer et al.*, 2002).

2.5.3 Groundwater Model

tRIBS uses a quasi-three dimensional cascade groundwater model that routes lateral soil moisture fluxes across TIN edges (*Ivanov et al.*, 2004a). Transmissitivity (T) of the phreatic aquifer is a non-linear function of the water table depth (N_{wt}), bedrock depth (κ), and the saturated hydraulic conductivity decay parameter (f) (*Ivanov et al.*, 2004a):

$$T = \frac{a_r K_{0n}}{f}(e^{-fN_{wt}} - e^{-f\kappa}). \qquad 2.30$$

For a more complete description of the tRIBS ground water model see *Ivanov* (2002).

2.5.4 Hyrologic Hillslope Routing

In tRIBS, a hydrologic routing scheme transfers water from the hillslope to the channel network. Runoff follows TIN edges from its point of generation at a hillslope node to an 'outlet' channel node. The hillslope travel time (t_τ) is calculated as:

$$t_\tau = \frac{l_h}{v_h(\tau)}, \qquad 2.31$$

where l_h is the hillslope runoff length. Hillslope velocity varies in both time and space as:

$$v_h(\tau) = c_v \left[\frac{Q(\tau)}{A_c} \right]^r, \qquad 2.32$$

where $Q(\tau)$ is the discharge at the outlet stream node at time τ, A_c is the contributing area of the outlet node, and c_v and r are constant parameters of the watershed (*Ivanov et al.*, 2004a).

2.5.5 Hydraulic Streamflow Routing

Once runoff from the hillslope reaches the channel, flow is routed through the stream network using a kinematic wave equation. The continuity equation for one-dimensional free surface flow that varies as a function of time is expressed as:

$$\frac{dF}{dt} + \frac{dQ}{dx} = R_b, \qquad 2.33$$

where F is the cross sectional area, Q is discharge in the x direction, and R_b is the lateral water influx from the hillslopes contributed to the channel per unit length (*Ivanov et al.*, 2004a). Assuming the channel cross sectional area approximates a rectangle, tRIBS uses Manning's equation to paramaterize the discharge term in 2.33:

$$Q = \frac{\sqrt{i_o}}{\eta} H^{5/3} b, \qquad 2.34$$

where H is depth, i_o is channel slope, η is channel roughness, and b is channel width (*Ivanov et al.*, 2004a). For this, study the channel width is provided to the model using a geomorphic power law which is discussed in section 4.2.

2.6 Summary

The review of tRIBS provided here relies heavily upon the work of *Ivanov* (2002) and *Ivanov et al.* (2004a) and no additional model development was preformed as part of this thesis. The discussion is meant to demonstrate where important parameters such as the conductivity decay parameter (f), saturated hydraulic conductivity (K_{0n}), Manning's roughness coefficient (η), and anisotropy ratio (a_r) appear within the mathematical equations that represent hydrologic processes. Chapter 4 and 5 further discuss model sensitivity to soil parameters and channel network representation. The reader is referred to the equations presented here in order to best interpret model output.

CHAPTER 3 - RÍO PUERCO DESCRIPTION

3.1 Introduction

The Río Puerco, located in west-central New Mexico, is an ephemeral arroyo that spans ~16,000 km^2 of diverse terrain from its headwaters along the Continental Divide, to the confluence with the Río Grande near the northern boundary of the Chihuahuan Desert (*Vivoni et al.*, 2006). Following only the Pecos River, the Río Puerco is the second largest tributary of the Río Grande in New Mexico (*Bryan and McCann*, 1936). Basin elevation ranges from 3,447 m at Mount Taylor to 1,436 m at the watershed outlet near Bernardo, NM. Major sub-watersheds include the Upper Río Puerco, Torreon Wash, Arroyo Chico, and the Río San José (Figure 3.1).

Along its north-south oriented main axis, the Río Puerco landscape shifts from a wetter high-alpine climate to a semi-arid environment with increasing proximity to the basin outlet. Annual precipitation totals average 323 mm/yr at Cuba, NM and 212 mm/yr at Bernardo, NM (*Griffin et al.*, 2005). Interrelated gradients in topography, rainfall, ecology, and channel geometry all have substantial impacts on the location and magnitude of runoff production in the basin (*Heath*, 1983; *Gorbach et al.*, 1996). However, the most dynamic and studied aspect of the Río Puerco has been the evolution of channel geomorphology following arroyo incision during the late 1800s.

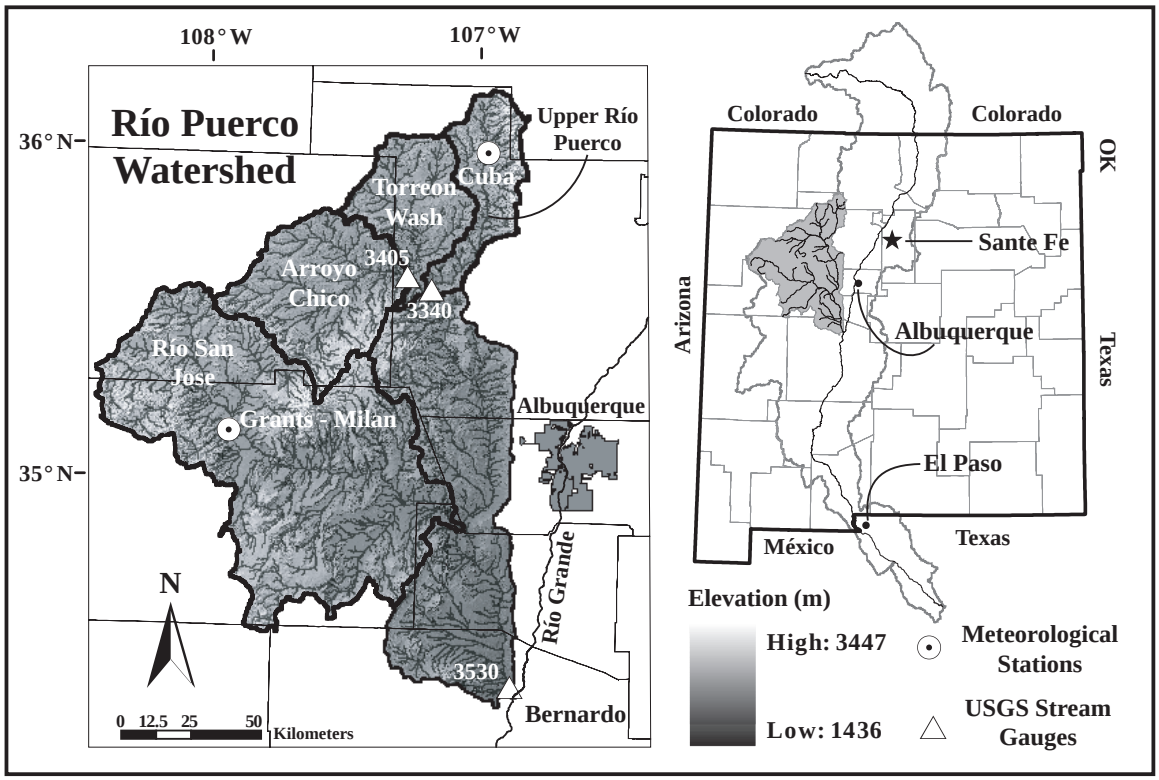

Figure 3.1 General Location of Río Puerco Watershed, NM. Includes locations of active USGS stream gauges, major subwatersheds, and meteorological stations within the basin. USGS stream gauge station number 3340 refers to the Río Puerco Above Arroyo Chico near Guadalupe NM, 3530 refers to the USGS stream gauge Río Puerco near Bernardo, NM, and 3405 refers to USGS stream gauge Arroyo Chico near Guadalupe, NM.

3.2 Arroyo Incision

In the latter half of the 19th century, ephemeral channel networks throughout the southwest United States began to incise into valley alluvium. Before arroyo development, many stream networks were reportedly unable to accommodate large floods (*Huntington*, 1914; *Bryan*, 1925). Consequently, stream discharge periodically overtopped channel banks and inundated valley floors (*Bryan*, 1925). Anecdotal evidence suggests that some southwestern watersheds had vegetation, including cottonwood stands and wetlands, which formed riparian corridors that bordered stream

networks (*Bryan*, 1925; *Antevs*, 1952; *Cooke and Reeves*, 1976). Natural meadows extensive enough to support hay production populated valleys in the Río Puerco, NM and San Simon Valley, AZ (*Bryan*, 1928; *Peterson*, 1950). As late as 1895, an area north of the confluence of the Río Puerco and the Río San Jose supplied one livery in Albuquerque, NM with 10 tons of hay per month (*Bryan*, 1928).

While grasslands suitable for grazing were known to exist during the mid-to-late 1800s, their spatial extent has remained a matter of uncertainty. A substantial portion of the written historical record concerning vegetation type and distribution exists in military diaries from the mid-to-late 1800s. Whether these journals are unbiased and accurately portray regional ecology is an unresolved question (*Leopold*, 1951a). Nevertheless, in effort to document semi-arid vegetation prior to major channel incision, *Leopold* (1951a) summarized written entries made by various expedition leaders who explored the Upper Río Grande and Río Puerco watersheds during the mid-1800s. The overall consensus drawn by Leopold was that although scattered areas confined to the valley bottoms were suitable for grazing, the large majority of northern New Mexico had failed to support expansive grasslands during the mid 19th century.

From many of the same diaries, *Bryan* (1928) and *Leopold* (1951a) narrate first-hand descriptions of Río Puerco geomorphology during the 1840s. Army Lieutenants J.W. Abert (1846) and J.H. Simpson (1849) report channel walls twenty to thirty feet high (*Bryan*, 1925). The military journals clearly acknowledge gullying had occurred in some reaches of the Río Puerco before 1850. Surveys performed by John W. Garreston in April and May 1885 also reveal incision had taken place along the Río Puerco south and west

of Albuquerque (in *Bettancourt*, 1980). At a single survey location, Garreston found channel banks reaching 20 feet high and arroyo widths of 72.6 to 92.4 feet (in *Bettancourt*, 1980).

However, some ambiguity remains as to the exact timing of incision and widening of arroyos both in the Río Puerco and across the southwestern United States. *Leopold* (1951a) claims that arroyo incision and widening was not pervasive within the Río Puerco until thirty-five years after Abert's and Simpson's initial observations. Leopold's conclusion is largely based upon oral histories provided to *Bryan* (1928) by residents who lived near Cabezon, NM during the mid-1880s. Inhabitants of the Upper Río Puerco valley described a stream that prior to 1885, was lined by meadows and cottonwoods and occasionally overflowed its bank. Then, in the latter half of the 1880s pervasive incision and channel widening occurred. Like *Bryan* (1928), *Duce* (1918) and *Rich* (1911) interviewed local ranchers in southern Colorado and southern New Mexico who also claimed major arroyos did not develop until the late 1870s to mid 1880s. Ultimately, whether inhabitants recollections are accurate or not, 1885 has generally been accepted as the date of widespread arroyo development across the southwestern United States (e.g., *Ellis*, 2004).

3.2.1 Consequences of Arroyo Incision

As arroyo development continued and channel walls increased in height, streams lost the ability to dissipate stream power through overbank flow (*Bryan*, 1925; *Simon and Darby*, 1999). With increased flow energy, stream networks conveyed massive sediment

loads to downstream locations. In the mid-1930s, the U.S. Soil Conservation Service estimated 20,000 acre-feet of silt had been removed from the San Simon tributary of the Gila River in San Simon Valley, AZ. Trenching of the San Simon Creek led to the formation of 70 miles of new channel over a span of 44 years. Additionally, a survey conducted by *Bryan and Post* (unpublished; 1937) found stream incision resulted in the removal of 400,000 acre-feet of sediment from the main channel and selected tributaries of the Río Puerco (in *Peterson*, 1950).

Consequences of upstream network incision included degraded water quality and reduced in-stream biodiversity at locations below the primary region of down-cutting (*Shields et al.*, 1998). Many researchers have suggested that due to the lowering of the water table below the pre-incision valley floor, traditional agricultural crops failed and plant species better adapted to a descending water table replaced indigenous vegetation (*Leopold*, 1951a; *Antevs*, 1952; *Elliott et al.*, 1999). Due to the widespread nature of channel incision and its negative effects on water quality, native ecosystems, and agriculture, the problem of arroyo incision intrigued both early 20th century naturalists and modern-day researchers. Investigation has focused primarily on the causal mechanisms underlying arroyo incision, the subsequent stages of arroyo recovery following initial network incision, and the possibility of restoring impaired watersheds to pre-incision conditions (*Elliott et al.*, 1999).

3.2.2 Arroyo Incision Hypotheses

Various hypotheses attempt to establish the fundamental driving mechanism(s) that initiated arroyo development in the southwestern United States. Most explanations can be lumped into one of the following categories proposed by *Schumm* (1999): (1) human induced; (2) climatic; (3) hydrologic; (4) geomorphologic/geologic; or (5) animal induced. It is beyond the scope of this paper to review all plausible causes of arroyo incision. However, the following section presents a review of potential explanations specific to New Mexico and the Río Puerco.

One of the original mechanisms identified as a probable underlying cause of mid-to-late 1800s arroyo incision was environmental degradation associated with the introduction of domesticated livestock (*Rich,* 1911; *Duce*, 1918). These hypotheses suggested that overgrazing, trampling, and the development of stock trails contributed to the reduction of semi-arid grassland and the compaction of soils (*Bailey*, 1935; *Peterson*, 1950; *Ellis*, 2004). Where grasses had formerly provided resistance to overland flow, the removal of vegetated cover decreased the hillslope hydraulic roughness and allowed unobstructed runoff across the land surface (*Rich*, 1911; *Bull*, 1997). Soil compaction contributed to decreased infiltration capacities and additional runoff per unit of rainfall (*Duce*, 1918; *Antevs*, 1952; *Ellis*, 2004). Together, the loss of grasses and the reduction of infiltration into the soil profile meant precipitation that had previously caused streamflow durations over a few days, now resulted in large magnitude flood events with short time to peaks and large sediment loads (*Rich*, 1911; *Antevs*, 1952).

While the timing of livestock introduction and the occurrence of arroyo incision coincided nicely, overgrazing was soon recognized as merely one possible cause of arroyo incision. Frederick S. Dellenbaugh, assigned to John Wesley Powell's second expedition down the Colorado River, argued the overgrazing hypothesis was incomplete (*Dellenbaugh*, 1912). He specifically found fault with *J.L. Rich* (1911) who had attributed arroyo incision near Silver City, NM to cattle-induced depletion of vegetation cover. Paraphrasing rancher Mr. MacMillan of the Mangas Valley near Silver City, Rich stated,

"The cattle...have kept the grass eaten so closely that there has been little opportunity for natural maturing and seeding, with the results that not only has the grass been kept closely cropped, but it has been to a large extent exterminated. Coincident with the removal of the vegetation has come an increase in the violence of floods. In the early days...heavy floods were rare. The storms were just as severe as now, but the run-off was slower. When overstocking had reduced the vegetation cover the first floods began to come, and have been coming with increased frequency and violence every year since."

However, *Dellenbaugh* (1912) contended,

"Mr. Rich presented only one phase of the subject. While the stated factor, 'removal of vegetation cover,' may in some localities, accelerate the retrograding (trenching) of streambeds, it is not, in my opinion, the cause of retrograding. I noted the same characteristics (and others probably also noted) years ago in places where there were no cattle and never had been any. "

Dellenbaugh's observations were further substantiated by *Peterson* (1950) who documented instances of arroyo incision at Fort Bayard Military Reservation, NM where grazing had been placed under strict limitations over previous decades. Across other watersheds, *Peterson* (1950) found that the introduction of domesticated cattle failed to result in any stream network entrenchment whatsoever.

Attributing arroyo incision merely to overstocked rangelands became additionally

problematic with the discovery of filled paleoarroyos in Chaco Canyon, NM and the Río Puerco watershed (*Bryan*, 1928). Evidence of archaic arroyos suggested that stream networks in the southwest had previously incised during a time period before livestock domestication. More recent work by *Love and Young* (1983) shows aggradation periods occurred in the Río Puerco between 2,000 and 3,000 years before present. Arroyo incision is assumed to have taken place between episodes of aggradation (*Elliott et al.*, 1999). Thus, arroyo incision was identified as a cyclical process and the overstocking of rangelands, while a probable contributor of mid-to-late 19th century arroyo incision, was not sufficient as the only cause of stream network trenching in the southwestern United States.

As an alternative to overgrazing, short-term changes in climate have been cited as potential factors that may initiate arroyo incision (*Bull*, 1997). Researchers adopting the climate change hypothesis argue arroyo incision was only accelerated, not caused, by overstocked rangelands. In an oft cited quote, *Bryan* (1928) alleges "the introduction of livestock and the ensuing overgrazing should be regarded as a mere trigger pull which timed a change about to take place." Climate-change theorists attributed arroyo incision to a wide range of often contradictory conditions - increased precipitation, drought, and variation in intra-annual rainfall intensities have all been offered as possible explanations.

Huntington (1914) proposed that a drier climate regime would promote the reduction of vegetative cover and hence, increase erosion on mountain slopes. The transfer of sediment from the hillslope to the channel supplied sediment volumes greater than the transport capacity of the stream. Subsequent in-channel settling of suspended

material led to network aggradation. In contrast, a shift to a wetter climate was thought to foster an increase in vegetation density and stabilize hillslope soils. Discharge with lower sediment concentrations would possess greater erosive power due to the added ability to convey sediment and lead to arroyo incision.

Others such as *Bryan* (1928) and *Antevs* (1952) concurred that drier conditions would lead to vegetative die-off. Rather than culminate in stream aggradation, the loss of vegetation was believed to diminish impedance to overland flow, increase stream power, and contribute to arroyo initiation (*Betancourt*, 1980; *Bull*, 1997; *Schumm*, 1999). While conceptually appealing, the theory is largely unsupported by climatic records. *Thornthwaite et al.* (1941) found no significant trends in annual temperature and precipitation values across the Southwest during the most recent period of arroyo incision (in *Leopold*, 1951b). Thus, the absence of increased aridity during the latest occurrence of widespread channel entrenchment across the southwestern United States left the hypothesis regarded as unsubstantiated (*Elliott et al.*, 1999; *Ellis* 2004). More recently, *Molnár and Ramírez* (2001) found that when precipitation records were grouped into climatic divisions, there is evidence for decreased precipitation from 1895 - 1904 in northwestern New Mexico. While the authors claim this date coincides with the beginning of the latest cycle of arroyo incision, their evidence of increased aridity postdates most documentation of arroyo development in the Río Puerco and across the southwestern United States (*Rich*, 1911; *Bryan*, 1925; *Bryan*, 1928; *Leopold*, 1951a; *Antevs*, 1951; *Cooke and Reeves*; 1976).

Although climatic shifts at the annual scale were not evident, patterns in

precipitation other than cumulative yearly totals were also examined as possible causes for arroyo incision (*Cooke and Reeves*, 1976; *Ellis*, 2004). *Leopold* (1951b) hypothesized that if high-intensity events contributed a large proportion of annual precipitation, then arroyo incision might ensue. In the theory, storms characterized by elevated rainfall rates generate substantial runoff and are the primary source of erosion. Alternatively, low-intensity precipitation tends to percolate into the soil column and contribute to plant growth, thereby minimizing erosive potential.

To substantiate the hypothesis, *Leopold* (1951b) studied intra-annual rainfall records from Las Cruces, NM and Santa Fe, NM from 1850-1948. Over the period of 1850-1880, Leopold found a lower frequency of small rainfall events (0.01-0.49 in.) and an increased frequency of high magnitude events (> 1.00 in). From 1881-1948, there was an overall increase in the frequency of small rainfall events relative to larger storms. *Elliott et al.* (1999) revisited precipitation records and also documented fewer low intensity storms and more recurrent high-intensity storms from 1868 - 1880. However, both *Elliott et al.* (1999) and *Ellis* (2004) mention that the climatic conditions necessary for Leopold's model of arroyo incision initiation occur prior to 1885. Thus, either incision was occurring before the mid 1880s and poorly documented, or a time lag is required between the increase in high intensity events and arroyo incision as suggested by *Leopold* (1951b).

In addition to climate change hypotheses, intrinsic geomorphic threshold scenarios also added to the growing catalog of potential underlying mechanisms driving arroyo incision (*Bull*, 1979). *Schumm and Hadley* (1957) surveyed the longitudinal

profile of seven small watersheds in New Mexico and Wyoming that exhibited disconnected arroyos. The sampling of watersheds included Cornfield Wash in the Torreon Wash subwatershed of the Río Puerco. In each basin surveyed, gully formation was associated with the steepening of the pre-incision valley fill where the hillslope provides an indication of the channel gradient prior to arroyo incision. These results indicate that for small basins, network trenching is associated with oversteepening of the valley fill (*Schumm and Hadley*, 1957). Additionally, the incised portion of disconnected arroyos tended to occur at greater slopes in smaller basins when compared to watersheds encompassing larger area. *Schumm and Hadley* (1957) argued that basins with larger contributing areas are able to integrate more rainfall and generate floods with more substantial stream power. Enhanced erosional forces due to greater discharge magnitudes in larger basins may have allowed incision to occur on more gradual slopes.

In summary, a wide variety of causes can lead to an incised river network. Identifying a single mechanism can prove difficult since arroyos often leave little evidence as to the origin of network incision. Determining specific processes leading to arroyo development is further complicated since multiple erosional processes can work conjointly and lead to similar channel geomorphology (*Cooke and Reeves*, 1976; *Elliott et al.*, 1999; *Schumm*, 1999). Despite the problems of identifying causal mechanisms, incised networks across different climatic and geologic conditions exhibit distinct stages of development, which tend to follow similar evolutionary sequences through time (*Simon and Darby*, 1999). The following section describes one hypothesis of arroyo development partially derived from research performed in the Río Puerco watershed.

3.2.3 Arroyo Incision Conceptual Model Hypothesis

Elliott et al. (1999) propose a revised version of a multi-stage arroyo evolution hypothesis that originally conceptualized channel development based upon both aerial photographs dating back to the late 1930s as well as field work performed within the Río Puerco during the late 1970s (Figure 3.2). The first stage of the hypothesis begins with a non-incised river network (a). In this stage, large streamflow events may overtop channel banks and flood the valley floor. Overbank flow allows dissipation of stream power and limits the erosive forces imparted on the channel walls (*Simon and Darby*, 1999).

The hypothesis moves to the incision stage (b) once the stream's sediment transport capability is greater than the amount of sediment supplied to the stream. As vertical incision begins, downcutting occurs quickly and the headwall progresses upstream as the channel enters a condition of non-equilibrium. With increasing channel depth, the network accommodates progressively larger flood events, which impart higher shear stresses on the channel's wetted perimeter. Where excessive discharge previously contributed to overbank flow, flood waters remain in the channel and contribute to greater stream power and erosive potential. Increasing bank heights associated with incision are maintained through negative pore pressures (*Simon and Darby*, 1999). Incision continues until mass wasting of arroyo walls allows the channel to widen (*Simon and Darby*, 1999; *Ellis*, 2004).

Lateral erosion (c) is an important stage of arroyo recovery that helps to slow channel degradation. Formerly existing riparian corridors present in the pre-incision and

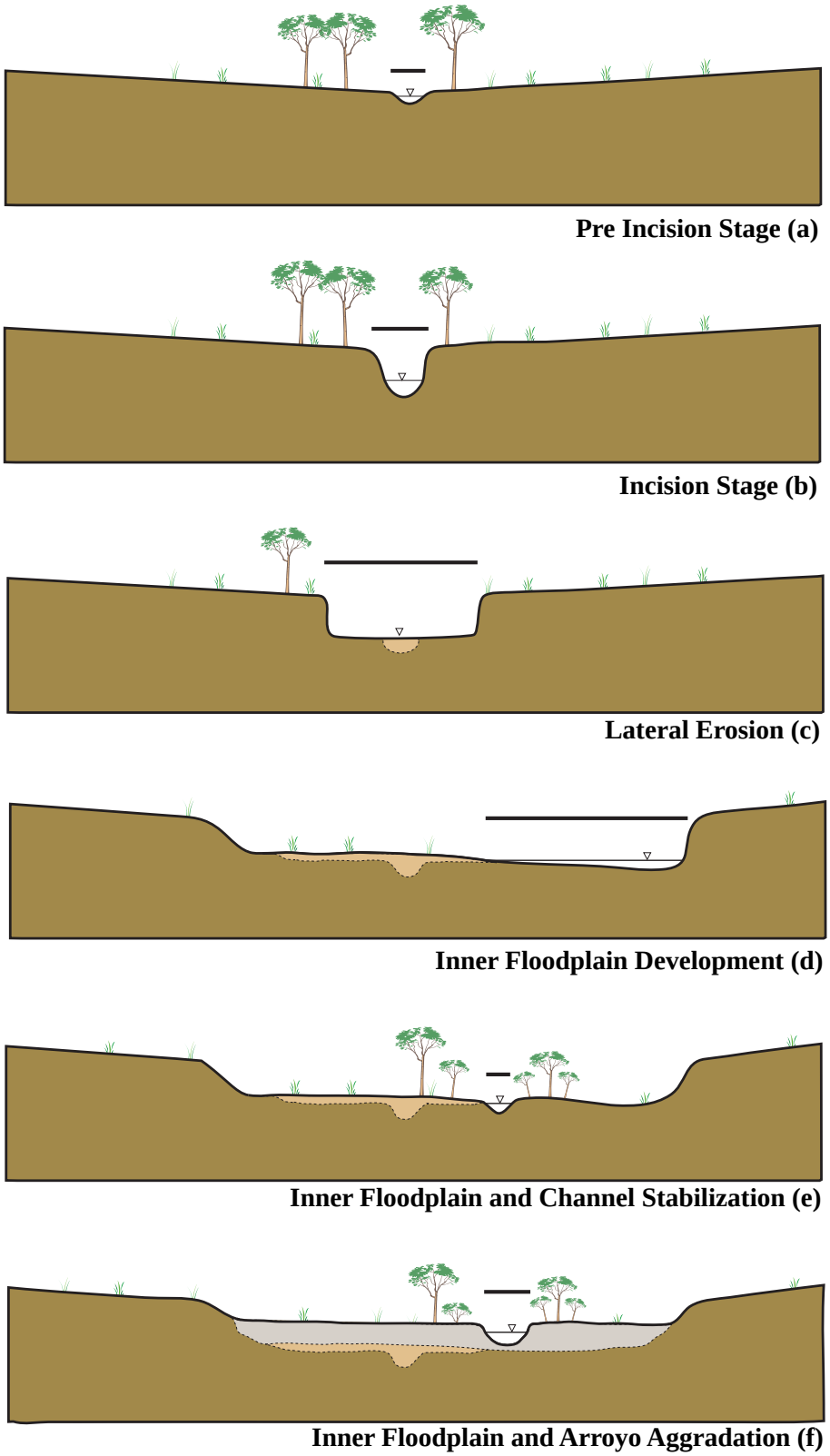

Figure 3.2 Conceptual Arroyo Geomorphic Sequence after *Elliott et al.* (1999). Bar indicates channel width.

incision stages are often removed due to the mass wasting of arroyo walls. As the channel widens, a given discharge volume that was previously confined to a deep but narrow channel now flows through a horizontally expanded cross section. Consequently, flow depth, shear stresses, and sediment transport capacity decreases (*Simon and Darby*, 1999). Furthermore, channel width adjustment also contributes sediment to downstream reaches, which leads to network aggradation and a more stable longitudinal profile (*Simon and Darby*, 1999). Lateral erosion continues until the arroyo grows sufficiently wide that streamflow is primarily confined to the center of the channel (*Ellis*, 2004).

Lateral erosion is followed by the development of an inner floodplain (d) and channel and inner floodplain stabilization (e). The reestablishment of riparian vegetation on the inner floodplain anchors soil and introduces form drag which reduces streamflow velocity and boundary shear stress applied to floodplain sediments (*Griffin et al.*, 2005). In the last stage (f), inner floodplain and arroyo aggradation results in a streambed that approaches the level of the pre-incised channel. For example, shrub encroachment and subsequent sediment deposition along reaches in the middle and lower Río Puerco has led to aggradation of both the floodplain and channel bed since the 1970s (*Griffin et al.*, 2005).

It is important to recognize a hypothesis of arroyo development is merely conceptual in nature and arroyos do not necessarily progress sequentially through each stage of the model. *Love* (1997) states that although similar geomorphic stages have been observed at some transects in the Río Puerco, changes in channel geomorphology are not strictly evolutionary. Because arroyo development is a function of adjustments to

channel gradient, vegetation, discharge, and sediment load, different stretches of the Río Puerco may appear to be at various stages within the arroyo model (*Love*, 1997). Thus, suggesting that the entire Río Puerco or even major subwatersheds are at a certain stage of arroyo development is a qualitative inference and a simplification of actual channel morphology and development.

3.3 Río Puerco Geology

The Río Puerco drains the southeastern Colorado Plateau, the Río Grande rift of the Basin and Range Province, and the Sierra Nacimiento (*Bryan and McCann*, 1936; *Heath*, 1983; *Ellis, 2004*; *Love and Connell*, 2005). The Sierra Nacimiento, which flank the northeastern edge of the Upper Río Puerco, are part of the southern Rocky Mountains and exhibit non-easily eroded metamorphic and igneous exposures (*Formento-Trigilio and Pazzaglia*, 1998; *Ellis*, 2004). Other Precambrian crystalline rocks also include the Zuni Mountains near Grants, NM and the Sierra Ladrones in the extreme southern portion of the watershed west of Bernardo, NM (*Elliott*, 1979).

The majority of basin outcrops (Figure 3.3), however, are dominated by easily eroded Tertiary and Upper Cretaceous sandstones, mudstones, and shales (*Gorbach et al.*, 1996; *Ellis*, 2004; *Griffin et al.*, 2005). Readily weathered sedimentary units account for approximately all exposed bedrock within the upper regions of the catchment. As a result, fluvial transport of fine sands, silts, and smectite clays is exceptionally high (*Ellis*, 2004). Between 1948 and 1973, the Río Puerco supplied 83% of the Río Grande's total sediment load measured ~84 km south of Bernardo, NM. In contrast to the large

proportion of sediment contributions, the Río Puerco accounted for merely 5.6% of the total Río Grande discharge over the same duration (*Gellis*, 1998). From 1973 to 1996, Río Puerco sediment load and streamflow contributions to the Río Grande decreased to 64% and 2.3% of totals respectively (*Ellis*, 2004). The apparent reduction in discharge and sediment load corresponds with a period of dense vegetation growth within riparian areas of the Río Puerco's lower reaches (*Gorbach et al*, 1996; *Molnár and Ramírez*, 2001).

In the northern portion of the watershed, the main stem of the Upper Río Puerco flows from north to south and parallels the Nacimiento Uplift. The valley surrounding the main channel is defined by sandstone cliffs to the west and highly dissected remnants of gravel capped pediments on the east (*Bryan and McCann*, 1936). In the mid-1930s, Bryan and McCann found that in areas where the Upper Río Puerco flows over sandstone formations, the channel tends to be narrow and constrained within canyon-like valleys. Where the arroyo is underlain by shales, the valley becomes wider with well defined floodplains. Within the watershed, smaller tributaries are relatively straight while sinuous higher stream order arroyos wind across the basin floor and actively erode former valley fill (*Gorbach et al*, 1996). As of 1996, one reach of the Upper Río Puerco south of Cuba, NM remained a braided stream across the complete width of the arroyo (*Gorbach et al.*, 1996).

In the Upper Río Puerco, fewer tributaries exist west of the primary channel axis. In this portion of the watershed, stream networks drain Cretaceous and early Cenozoic formations characterized by lower slope and elevation (Figure 3.3). *Bryan and McCann*

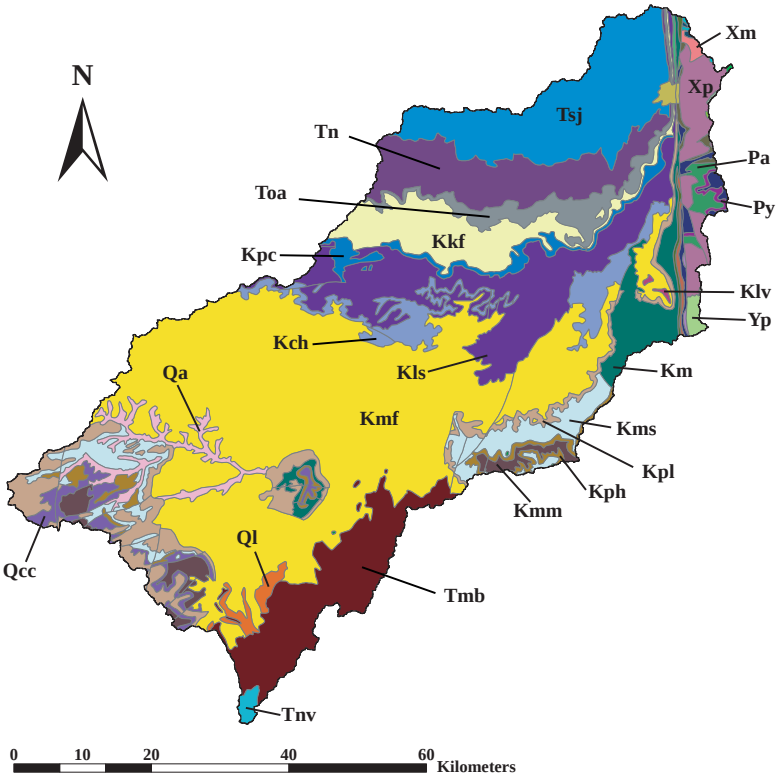

Quaternary

- Qa - Alluvium upper and middle Quaternary
- Ql - Landslide deposits and colluvium
- Qp - Piedmont alluvial deposits; upper and middle Quaternary; includes deposits of higher gradient tributaries bordering major stream valleys, alluvial veneers of the piedmont slope, and alluvial fans

Tertiary

- Ti - Tertiary intrusive rocks; undifferentiated
- Tmb - Basalt and Andesite Flows; Miocene
- Tn - Nacimiento Formation; Paleocene, San Juan Basin
- Tnv - Neogene volcanic rocks; primarily in Jemez Mountains
- Toa - Ojo Alamo Formation Paleocene, San Juan Basin
- Tps - Paleogene sedimentary units; includes Baca, Galisteo, El RIto, Blanco Basin, Love Ranch, Lobo, Sanders Canyon, Skunk Ranch, Timberlake, and Cub Mountain Formations
- Tsf - Lower and Middle Santa Fe Group; Includes Hayner Ranch, Rincon Valley, Popotosa, Conchiti, Tesuque, Chamita, Abiquiu, and other Formations; Miocene and uppermost Oligocene
- Tsj - San Jose Formation; Eocene, San Juan Basin

Cretaceous

- Kcc - Crevasse Canyon Formation; coal-bearing units are Dilco and Gibson Coal Members; other members are Bartlett Barren, Dalton Sandstone, and Borrego Pass Sandstone (or Lentil)
- Kch - Cliff House Sandstone; transgressive marine sandstone; Campanian
- Kd - Dakota Sandstone; includes Oak Canyon, Cubera, and Paguate Tongues plus Clay Mesa Tongue of Mancos Shale; Cenomanian
- Kkf - Kirtland and Fruitland Formations; coal-bearing, coal primarily in Fruitland; Campanian to Maastrichtian
- Kls - Lewis Shale; marine shale and sandstone
- Klv - La Ventana Tongue of the Cliff House Sandstone
- Km - Mancos Shale; divided into Upper and Lower Parts by Gallup Sandstone
- Kmf - Menefee Formation; mudstone, shale, and sandstone; coal bearing
- Kmm - Mulatto Tongue of the Mancos Shale
- Kms - Satan Tongue of the Mancos Shale
- Kmv - Mesaverde Group; includes the Gallup Sandstone, Crevasse Canyon Formation, Point Lookout Sandstone, Menefee Formation, and Cliff House Sandstone
- Kpc - Pictured Cliffs Sandstone; prominent cliff-forming marine sandstone
- Kph - Hosta Tongue of Point Lookout Sandstone; transgressive marine sandstone
- Kpl - Point Lookout Sandstone; regressive marine sandstone in McKinley and Sandoval Counties. The lower, Hosta Tongue, of Point Lookout is trangressive and is separated from main body by the Satan Tongue of Mancos Shale; Santonian - Campanian

Jurassic

- J - Jurassic rocks, Middle and Upper, undivided
- Jm - Morrison Formation; Upper Jurassic nonmarine rocks present only in northern one-third of state

Triassic

- @c - Chinle Group; Upper Triassic; includes Moekopi Formation (Middle Triassic) at the base in many areas

Paleozoic

- M - Mississippian rocks, undivided; Arroyo Penasco Group in Sangre de Cristo Mountains, Sierra Nacimiento, San Pedro Mountains, and Sandia Mountains; Lake Valley Linmestone in south-central New Mexico
- P - Permian rocks, undivided
- Pa - Abo Formation; red beds, arkosic at base, finer and more mature above; Wolfcampian; may include limestone beds of Pennsylvanian age (Virginilian) in Zuni Mountains. In Roledo Mountains the Abo may be considered a member of the Hueco Formation
- Pct - Cutler Formation; used in northern areas and Chama embayment only
- Py - Yeso Formation; sandstones, siltstones, anhydrite, gypsum, halite, and dolomite; Leonardian
- &m - Madera Mormation (Limestone, or Group); in Manzano Mountains includes Los Moyos Limestone and Wild Cow Formation; in Lucero Mesa includes Gray Mesa, Atrasdo, and Red Tanks Members; in Sacramento Mountains includes Beeman and Holder Formations; may include strata lumped as Magdalena Group in a few areas

Precambrian

- Xm - Lower Proterozoic metamorphic rocks, dominantly felsic volcanic, volcanoclastic and plutonic rocks (1650-1700+ Ma); includes Vadito Group; locally includes high-grade felsic gneisses of unknown age
- Xp - Lower Proterozoic plutonic rocks (older than 1600 Ma)
- YXp - Middle and Lower Proterozoic plutonic rocks, undivided
- Yp - Middle Proterozoic plutonic rocks (younger than 1600 Ma)

Figure 3.3 Geologic Map of Upper Río Puerco, Torreon Wash, and Arroyo Chico Watersheds (after *Anderson and Jones*, 1994)

(1936) state that precipitation falling on this fraction of the basin often infiltrates and discharge contributions are thought to be small relative to runoff generated on the mountain front. Streamflow originating west of the channel axis typically contains large amounts of fine grained sediment including clays, silts, and sands (*Bryan and McCann*, 1936).

3.4 Río Puerco Vegetation and Soils

Vegetation in the Río Puerco consists primarily of grasslands and pinyon juniper woodlands in addition to sagebrush and forest (*Molnár and Ramírez*, 2001). Within the Upper Río Puerco, *Francis* (1986) identified over 45 distinct plant communities at 114 sites that were allocated to one of the following categories: (1) Ponderosa or Pinyon Pine; (2) Juniper; (3) Shrubland including Artemisia (sagebrush), Chrysothamnus (rabbitbrush), Atrixpex (saltbush), and Scarcobatus (black greasewood) communities; (4) Grasslands including Gutierrezia (snakeweed), Bouteloua (blue grama), and Sporobolus (alkali sacaton) communities. In nearby Cornfield Wash within the Torreon Wash subwatershed, *Branson and Janicki* (1986) found a 380 percent increase in vegetation from 1958 to 1979. Improved vegetative production was attributed to increased precipitation as well as a reduction in grazing. Hydrologic implications of increased plant biomass include decreased sediment loads as well as reduced runoff production both of which have been observed trends in the Río Puerco over the past sixty years. A map of land cover from the United States Geological Survey (USGS) National Land Cover Dataset (NLCD 92) is used in the tRIBS hydrological model of the Upper Río Puerco and is presented in Chapter 4.

Francis (1986) identified three soil orders and three soils complexes in the Upper Río Puerco, where a complex refers to two or more soils that are well mixed and cannot be shown as an individual order on a soil map. Soil orders included Entisols, Aridsols, and Mollisols. Entisols were almost entirely confined to alluvial floodplains and often formed from sandstone and shale parent material. Soil texture within the Entisol order was highly variable and included silty-clay-loams, loamy-sands, clay-loams, and clays. The Aridsol soil order supported minimal vegetation and soil texture was primarily a fine-loam. Mollisol soils in the Upper Río Puerco were identified as young orders and exhibited either fine loamy or clayey texture. Complexes consisted of basalt, gypsum, and orthents (Entisols without horizon development) outcrops. As with landuse, explicit soil representation is required within the tRIBS hydrologic model and a soil texture map from the State Soil Geographic Database (STATSGO) is presented in Chapter 4.

3.5 Río Puerco Hydrometeorology

Soil and vegetative controls on rainfall infiltration combined with precipitation intensity, duration, and spatial extent are some of the most important factors dictating runoff generation in semi-arid environments (*Beven,* 2002). Precipitation during the summer months across the southwestern Untied States is driven primarily by the North American Monsoon (NAM). The NAM is a synoptic atmospheric circulation phenomena centered over northwestern México whose peripheral influence extends into the southwestern United States (*Douglas et al.*, 1993; *Gochis et al.*, 2006). Increased atmospheric water vapor in conjunction with on-shore flow resulting from thermal imbalances between the land surface and the Gulf of California and Eastern Pacific

Ocean, produces a diurnal pattern of convective activity over the core monsoon region (*Huntington*, 1914; *Stensrud et al.*, 1995; *Gochis et al.*, 2006). As a result, the NAM is the primary source of precipitation for the Sierra Madre Occidental foothills of northwestern Mexico, where roughly 70% of total annual rainfall occurs during the three months of June, July, and August (*Douglas et al.*, 1993).

While summer climatology in the southwestern United States is strongly influenced by the NAM, precipitation over the region is characterized by high spatial and temporal variability. Variability is primarily a function of proximity to mountainous terrain and the region's considerable distance from major moisture sources (*Adams and Comrie*, 1997; *Vivoni et al.*, 2006). Because Arizona and New Mexico are significantly removed from the monsoon core, the development of convective storms is reliant on low level-moisture advection into the southwestern Untied States. Historically, researchers attributed the increased atmospheric water vapor required for the development of mesoscale convective activity to the transport of moisture westward from the Gulf of México. This seemed logical since increased precipitation associated with the onset of the summer monsoon season coincides with a shift in mid-tropospheric flow from a generally dry southwest direction to a cool moist southeasterly orientation (*Douglas*, 1995; *Adams and Comrie*, 1997). However, because dewpoint temperatures at the 500 mb and 700 mb level over the Sierra Madre Occidental are greater than those observed at identical pressure heights over the Gulf of Mexico, other process(es) likely account for the increased low-level atmospheric water vapor within the NAM region during the summer months (*Douglas et al.*, 1993).

As an alternative explanation, *Hales* (1972) and *Brenner* (1974) suggested the eastern tropical Pacific could contribute the water vapor necessary for sustaining the NAM in the southwest United States through "gulf surges." These surges are frequently initiated as cloud masses traverse the mouth of the Gulf of California. *Hales* (1972) and *Brenner* (1974) hypothesized that beneath the tropical disturbances, precipitation cools the surrounding atmosphere thereby creating a region of high pressure. Evaporative cooling of the atmosphere in the southern Gulf of California is contrasted by an area of thermally induced low pressure entrenched over the deserts of the southwest United States. The pressure contrasts, in effect, create a southerly sea breeze capable of advecting moisture northward into Arizona and as far east as New Mexico (*Brenner*, 1974).

More recently, gulf surge propagation over the Gulf of California has been re-identified as an important source of summer-time low-level atmospheric moisture for the southwestern United States. Researchers involved in the Southwest Area Monsoon Project (SWAMP) have demonstrated the presence of a nocturnal low-level jet capable of transporting moisture from the northern Gulf of California into the northern Sonoran desert (*Douglas,* 1995*; Douglas,* 1998; *Fawcett et al.,* 2002). Mesoscale model results also suggested that the strengthening of southerly flow coincides with the development of gulf surges (*Stensrud et al.,* 1995). Further modelling performed by *Stensrud et al.*, (1997) indicate that the passage of mid-latitude troughs across the western United States followed a few days later by easterly waves moving away from the western Mexican coastline could induce a gulf surge event. As *Vivoni et al.* (2006) noted, gulf surges

initiated by tropical storms are also known to precede widespread convective activity in the southwest United States (*Brenner*, 1974).

Like many watersheds in western New Mexico and Arizona, the Río Puerco receives significant rainfall during the monsoon season. On average, rainfall contributions during July, August, and September account for 40-60% of total annual precipitation that falls in the watershed (*Gorbach et al.*, 1996; *Molnár and Ramírez*, 2001). Convective thunderstorms generally cover less than 10 km^2 and occur over time periods from minutes to a few hours although larger mesoscale events do occur given proper meteorological conditions (*Vivoni et al.*, 2006). Due to the limited temporal and spatial extent of precipitation, runoff may interact with drier soils down slope and reinfiltrate as runon. Overland flow reinfiltration, together with high potential evapotranspiration rates and transmission losses through the streambed, tend to support very low runoff ratios. *Molnár and Ramírez* (2001) determined only 2-3% of annual precipitation appears as channel discharge for the entire Río Puerco watershed. However, precipitation over the basin, especially under conditions of elevated antecedent soil moisture conditions, can generate substantial runoff production.

The majority of measurable discharge at the watershed outlet occurs in response to precipitation associated with the NAM. Approximately 90% of all streamflow at Bernardo takes place from May through October (*Gorbach et al.*, 1996) with ~38% of annual flow occurring during the month of August alone (*Molnár*, 2001). Streamflow magnitudes during these months are often some of the highest on record. Since 1940, the Río Puerco near Bernardo USGS streamgauge has recorded the maximum annual

discharge measurement during the months of July, August, or September ~76 % of the time (Figure 3.4a). Because the historical record at Bernardo is twelve years longer than the period of record for the Upper Río Puerco (Figure 3.4), analysis was also confined to the period of common record to allow for comparison between gauges. From 1952 - 2006, annual peak streamflow at Bernardo occurred during July, August, or September ~ 77% of inclusive years.

Monsoon floods originating within the watershed have historically caused extensive damage in the Middle Río Grande Valley above Elephant Butte Reservoir. In the late summer and early fall of 1929, two massive flood events in the Río Puerco were recorded at Bernardo, NM. On August 12, discharge was measured at 852 m^3/sec and on September 23, flood waters rose again as streamflow reached 1,068 m^3/sec. Discharge contributions from the Río Puerco and Río Salado watersheds entered the Río Grande and resulted in overbank flow at San Marcial, NM ~ 48 km south of Socorro, NM. Sediment deposition on agricultural fields adjacent to the river destroyed entire crops and the town was subsequently abandoned (*Gorbach et al.*, 1996).

While monsoon precipitation still generates occasional flooding, maximum annual discharge volumes at Bernardo have decreased over the past 60 years (Figure 3.4b). Although the annual peak flood typically occurs during the NAM, reduction in flood magnitude cannot be attributed to either lower summer rainfall totals or reduced storm intensities (*Molnár and Ramírez*, 2001). Thus, the declining trend is likely caused by alternative factors that affect runoff production or flood transmittance within the basin (*Molnár and Ramírez*, 2001).

a.

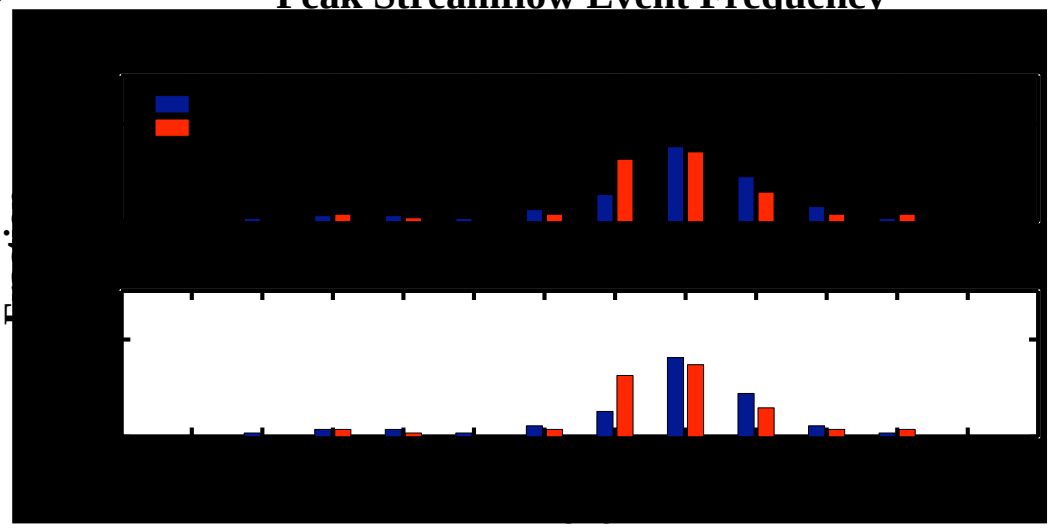

b.

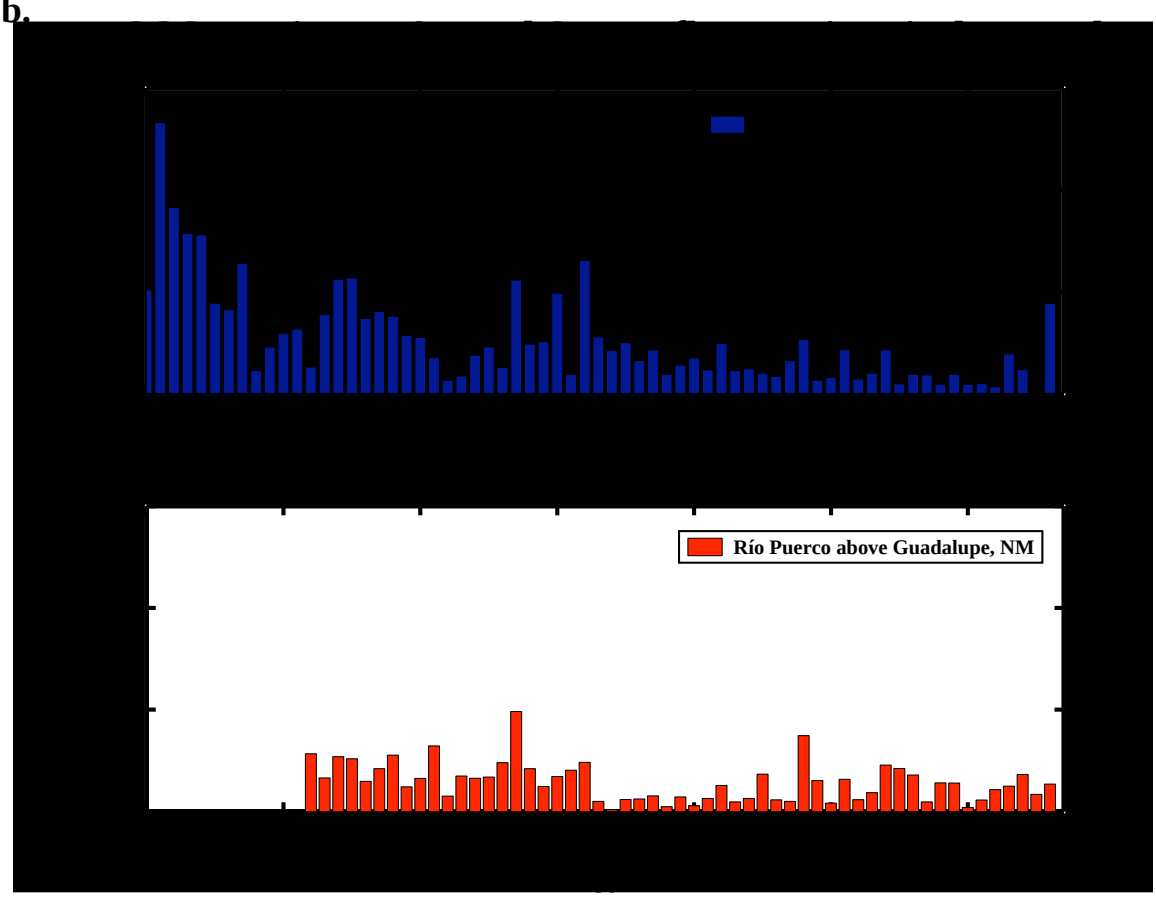

Figure 3.4 a) Peak Streamflow Event Frequency - Río Puerco Near Bernado Gauge and Río Puerco Above Arroyo Chico Near Guadalupe Gauge (b) Annual Maximum Discharge Event for the Historical Gauging Record - Río Puerco Near Bernardo Gauge and Río Puerco Above Arroyo Chico Near Guadalupe Gauge. Note, maximum flood for 2005 at Río Puerco near Bernardo is unavailable.

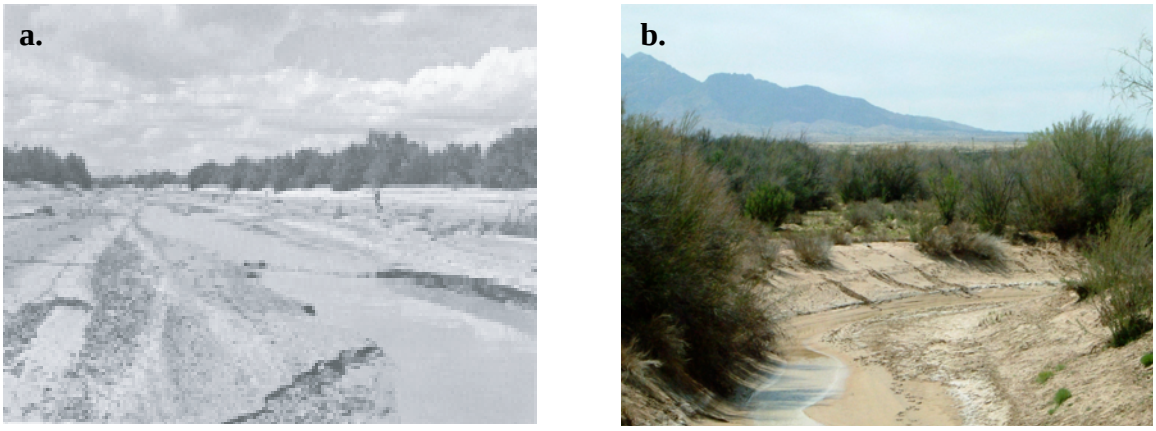

Figure 3.5 (a) Río Puerco near Bernardo looking west toward old U.S. Hwy 85 bridge, 1961 (from *Nordin*, 1963) (b) Río Puerco near Bernardo looking west toward old U.S. Hwy 85 bridge, 2007

Molnár and Ramírez (2001) suggest the reduction in peak discharge may result from increased channel transmission losses or limitations in flood conveyance due to evolution of channel geometry. Tamarisk (salt cedar) introduction in the 1920s near the watershed outlet has led to increased bank stability as well as channel and floodplain aggradation especially along middle and lower reaches of the Río Puerco (*Gorbach et al.*, 1996). USGS photographs taken during the early 1960s show that the Río Puerco downstream of the Bernardo gauge historically possessed an extremely wide cross-section with vegetation well displaced from the middle of the channel. Photographs from 2007 taken near the same reach demonstrate the encroachment of vegetation, the reduction of channel width, and the increase in channel depth (Figure 3.5). Current channel geomorphology may promote overbank flow at magnitudes that were historically contained within the channel cross section. Channel losses through overbank flow could provide a positive feedback that results in sediment deposition on floodplains, the narrowing of the active channel, and reduction in peak magnitude flood at the watershed

outlet.

Although the peak annual flood event in the Upper Río Puerco typically occurs during the monsoon season, spring streamflow is less variable and accounts for a large proportion of total annual discharge. Runoff during spring months is primarily a function of snowmelt, although frontal passages can result in heavy precipitation over the basin. Yearly snowfall totals recorded at Cuba, NM average ~ 648 mm/yr. More mountainous portions of the headwater basin tend to experience higher annual snowfall. Along the eastern slopes of the Sierra Nacimiento just outside the Upper Río Puerco watershed boundary, mean yearly snowfall totals are in excess of 3,000 mm/yr (*Molnár*, 2001). *Molnár and Ramírez* (2001) estimate 42% of total annual runoff at the Río Puerco near Guadalupe USGS streamgauge is related to spring-time runoff while 32% of the annual discharge occurs during the summer monsoon season.

Analysis of monthly streamflow averages show the Upper Río Puerco has the highest average monthly discharge in May (Figure 3.6). In contrast, the Río Puerco near Bernardo exhibits maximum monthly discharge averages during the NAM. Because streamflow in the Upper Río Puerco during the summer months is substantially less than discharge observed near Bernardo, additional runoff contributions must originate within other subwatersheds.

Previous research has suggested the Arroyo Chico is a source of large rainfall-runoff production during the NAM (*Heath*, 1983; *Molnár and Ramirez*, 2001; *Ellis* 2004). Historical data for the USGS Arroyo Chico near Guadalupe NM stream gauge

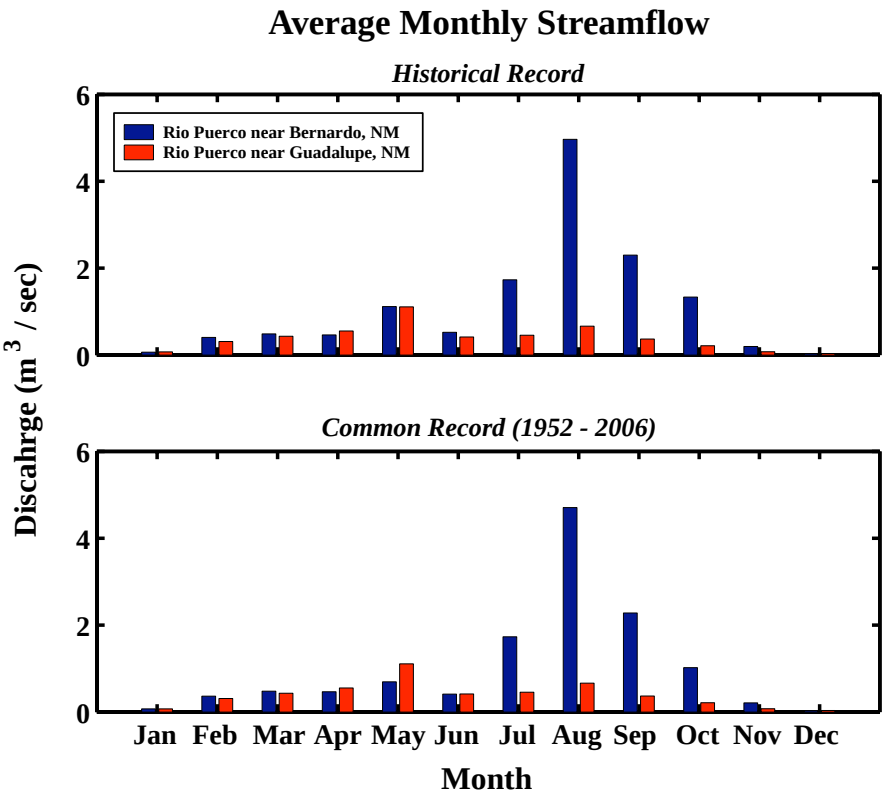

Figure 3.6 Average Monthly Streamflow for the USGS Gauge Río Puerco Above Arroyo Chico near Guadalupe, NM and USGS Gauge Río Puerco near Bernardo, NM.

(USGS Gauge # 3405 in Figure 3.1) is available from 1944 through 1986. In October 2005, the USGS reactivated the stream gauge and real-time discharge and stage data is currently available for the Arroyo Chico through the USGS National Water Information System (http://waterdata.usgs.gov).

3.5.1 Hydrometeorology Case Study

From September 3-11 2003, mesoscale thunderstorms developed over eastern Arizona and advanced into New Mexico due to the high pressure circulation pattern centered over the Four Corners region. Mesoscale scale thunderstorms are sub-synoptic systems that range in horizontal extent from fifty to hundreds of miles and have duration

times on the order of hours. The late season monsoon events may have been initiated as Hurricane Ignacio moved over Baja California from August 22 - 27 and supplied additional low level atmospheric moisture over the Gulf of California. A few days later on September 3 and 4, 2003 a gulf surge was reported in Guaymas, Sonora, suggesting that southerly flow could have advected moisture into Arizona and lead to mesoscale storm development (*Vivoni et al*., 2006).

As storms moved across the Río Puerco from southwest to northeast, they interacted with elevated terrain in the Upper Río Puerco, Torreon Wash, and Arroyo Chico Watershed. Heavy rainfall in the Upper Río Puerco resulted in a flood peak of ~ 50 m^3 /sec between 8 and 9 pm on September 10 at the gauge near Guadalupe, NM (3340). The flood propagated ~ 205 km downstream and caused multiple peak flows of ~ 78 m^3 / sec at the USGS Bernardo, NM stream gauge on September 14 between 8:15 am and 9:45 am[1]. A series of transect wells recorded fluctuations in groundwater levels as the flood pulse exited the Río Puerco and propagated through the middle Río Grande toward Elephant Butte Reservoir. The Río Puerco flood event of 2003 provided initial motivation for this modelling study in order to better understand watershed runoff response in a semi-arid basin. The following chapter describes the tRIBS model setup and calibration for the Upper Río Puerco headwater basin.

[1] Because the Arroyo Chico stream gauge was inactive during 2003, runoff contributions from the Arroyo Chico could not be determined.

CHAPTER 4 - MODEL SETUP, CALIBRATION, AND RESULTS

4.1 Introduction

Because tRIBS is a distributed model, spatial data must be acquired and converted into an appropriate format to perform hydrologic simulations. The following sections describe the data sources used for both a simple test basin (19.3 km^2) as well as the Upper Río Puerco (1119 km^2). Spatially distributed data for topography, land cover, soils, and precipitation are available from various government agencies already in GIS format or a format that may be converted into a GIS dataset. All tRIBS required datasets and the codes used to derive them are provided on a DVD which accompanies this document.

4.2 Topographic Data

Various topographic datasets are available from the United States Geological Survey (USGS). For example, the National Elevation Dataset (NED) consists of an assortment of raster products at different horizontal resolutions including 1 arc second (~30 m), $^1/_3$ arc second (~10 m), and $^1/_9$ arc second (~ 3 m). Currently, 1 arc second data is the only seamless product available for the entire United States including Hawaii, Alaska, and island territories. Vertical resolution varies by ± 7 to 15 meters depending on the source of the Digital Elevation Model (DEM) (www.seamless.gov). For New Mexico, 10 m DEMs are available for the entire state. Although this dataset provides

higher spatial resolution, analysis has shown that elevation artifacts can lead to unrealistic parallel overland flow directions during DEM processing. As a result, the NED 1 arc second product is selected for use in this study.

In order to delineate the Río Puerco watershed and its major subbasins, the NED 1 arc second product was obtained from the USGS for an area slightly larger than the region of interest. DEM processing and watershed delineation consisted of several steps, all of which were performed using either ArcInfo Workstation or the ArcHydro toolbox extension for ArcMap. Analysis began with the filling of sinks (also called pits). Sinks are grid cells that fail to drain into any of eight adjacent cells and typically occur due to data errors, sampling routines, or elevation values that are rounded to the nearest integer (ESRI, 1982-2002; *Tarboton et al.*, 1991). If sinks are not raised to the height of their pour point, the derived drainage network may be discontinuous (ESRI, 1982-2002).

Once pits are corrected, a flow direction grid is extracted from the filled DEM. Each flow direction grid cell is assigned a value that corresponds to the direction of steepest descent between neighboring cells. The flow direction grid provides the basis for construction of the flow accumulation grid. Each grid node in the flow accumulation raster is assigned a value that corresponds to the number of cells upstream of that particular point. Because each grid cell has identical area (e.g., 28.04 m by 28.04 m), multiplying a flow accumulation value by cell area gives the upstream contributing area to a given cell. The filled DEM, flow direction gird, and flow accumulation grid are all required datasets for Triangulated Irregular Network (TIN) generation.

The next major step in watershed delineation was determining the constant area threshold that reproduced accurate stream network density for the Upper Río Puerco. In ArcHydro, the user specifies the minimum number of cells that must drain to a particular node for the cell to be considered part of the stream network. Because water is only allowed to drain along the direction of steepest slope to one of eight neighboring cells, this approach is referred to as the D8 methodology (*Tarboton*, 1997). To ensure accurate network density, GIS derived drainage networks were compared to 1 m orthophotos of the Upper Río Puerco obtained from the New Mexico Resource Geographic Information System Program (RGIS) website (http://rgis.unm.edu). A constant area threshold of 315 grid cells (0.25 km^2) adequately reproduced the stream network observed in the orthophotographs and is used to delineate the stream network used in tRIBS model calibration (Figure 4.1).

High resolution orthophotographs of the Upper Río Puerco were also used to generate a geomorphic power law where stream width is plotted as a function of contributing area (Figure 4.2). Thirty locations were selected based upon network clarity in the orthophotographs along with the additional intent of sampling a wide range of contributing area values. Stream widths were measured in ArcMap and the contributing area above each transect was calculated using the flow accumulation grid. Figure 4.2 shows the location of each point used in constructing the power-law relationship. The geomorphic power law is expressed as:

$$W = aA^b \qquad 4.1$$

where W is stream width (m), a is a coefficient, A is upstream contributing area (km^2),

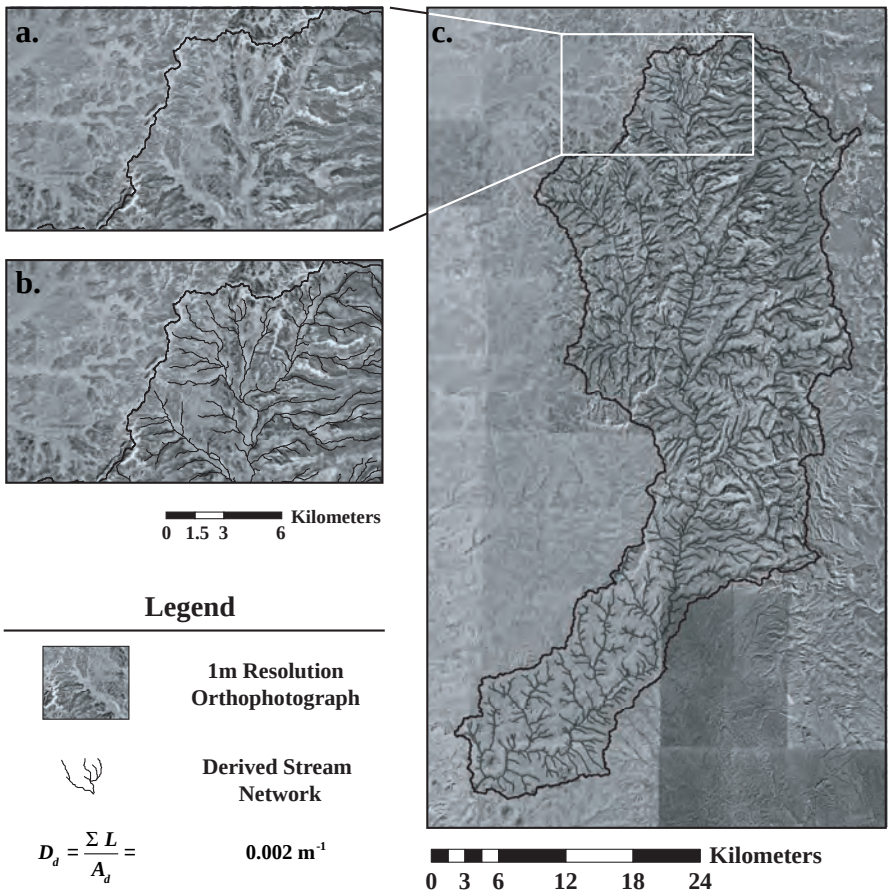

Figure 4.1 (a) 1 m orthophotograph inset with washes that approach the watershed divide (b) Orthophotograph inset with stream network overlay. There is a small displacement between orthophotographs and the GIS derived network due to slightly different geographic projections. (c) GIS derived network using constant area threshold of 0.25 km^2. This corresponds to a drainage density (D_d) of 1.47 km^{-1} where $D_d = \Sigma L / A_d$; ΣL is the total length of all stream network links and A_d is watershed area (*Dingman*, 2002)

and *b* is an exponent. Stream width measurements at lower contributing areas were predominantly sampled from the northern portion of the watershed. In this region of the basin, the stream channel and floodplain were usually observable, whereas streams with origins in the Sierra Nacimiento exhibited stream widths that were difficult to measure with confidence. Forest cover on the Nacimiento Mountain front may have obstructed photographic images of the stream channel. Recently published color orthophotographs

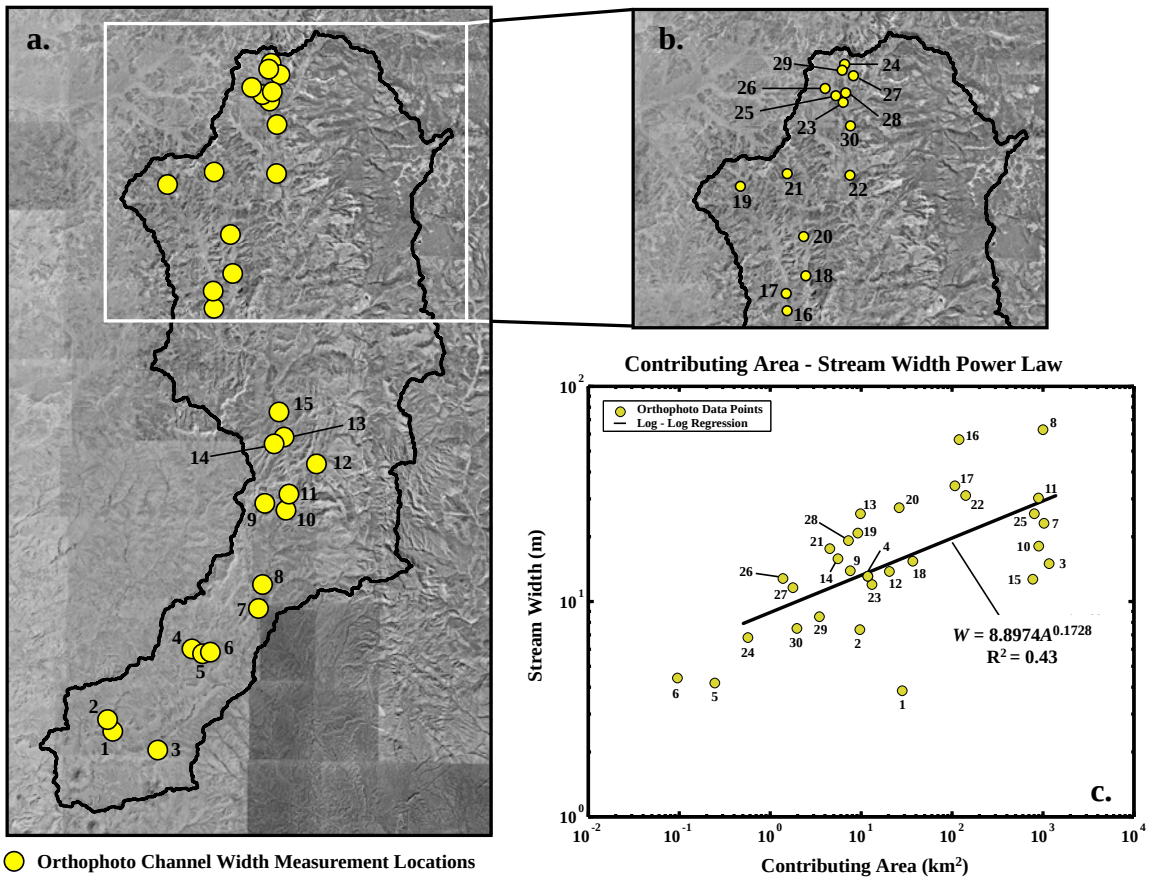

Figure 4.2 (a) Location of GIS measured channel network widths and contributing area (b) Points selected in the northern headwaters of the Upper Río Puerco (c) Geomorphic power law where stream width is a function of contributing area. The coefficient and exponent of the log-log regression provide parameter values for tRIBS representation of stream network width.

allow more definitive recognition of stream networks within this portion of the watershed but were only available following model setup and calibration.

The geomorphic power law coefficient (a = 8.8971) and exponent (b = 0.1728) are used as parameter values that allow tRIBS to estimate variation in stream channel width. The power-law relationship assumes decreasing network width with increasing distance from the watershed outlet. However, as noted in Section 3.3, Upper Río Puerco

stream width is highly dependent on local geology. The channel network tends to narrow in regions where flow occurs through sandstone formations, while channels are wider where the Upper Río Puerco flows across units of easily eroded shale. Also, changes in channel width occur as arroyos transition from a down-cutting to a widening phase and these adjustments may not occur synchronously throughout the basin. Thus, the geomorphic power law likely assigns incorrect actual channel width values to many locations throughout the watershed. Rather than attempting to accurately depict stream widths in all locations, the model parameterization applies a basin-averaged channel width for all positions along the stream network that exhibit a particular upstream contributing area. However, despite potential error, the geomorphic power law approach provides a tractable alternative to measuring actual channel widths throughout a large watershed demonstrating spatially extensive drainage networks.

TIN generation was performed using a series of ArcInfo Arc Macro Language (AML) scripts (*Vivoni et al.*, 2004). The constant area threshold value determined in ArcHydro during basin delineation was also specified in the TIN software package to preserve the same stream network representation. As discussed in Chapter 2, tRIBS requires a high resolution floodplain to accurately represent the saturation excess runoff mechanism near channel networks. Floodplain extraction from a DEM is based upon an algorithm developed by *Williams et al.* (2000), which requires an elevation and a Strahler stream order threshold as parameter values. For the Upper Río Puerco, points were considered to lie within the floodplain if their elevation was within 5 m of the elevation at the local channel outlet and points drained to a second order or higher stream link. The

polygon coverage generated by the floodplain algorithm typically contains topological errors that must be corrected prior to incorporation within the TIN. Most problems with topology were resolved by applying a 15 m buffer to the floodplain coverage. The remaining errors were corrected manually using the ArcMap editor.

The TIN used for Upper Río Puerco tRIBS model calibration was created using the Lattice TIN method at a Z_r resolution of 10 m. A floodplain was imbedded within the TIN using the Very Important Point (VIP) method. The VIP sampling routine was set to retain ten percent of the DEM nodes falling within the floodplain coverage. The TIN used for calibration efforts retained 8.9% of the original DEM nodes and exhibited a RMSE of 3.034 m (Figure 2.2). For a full discussion of TIN generation, refer to sections 2.3 and 2.4.

TIN disassembly using the ArcINFO ungeneratetin tool results in a series of Arc files (*.pnt and *.lin), which are read into the tRIBS hydrologic model. tRIBS converts the Arc files to a file (*.points) that contains the x and y coordinate, elevation, and type of each node (Figure 4.3). Node types include an outlet node, boundary nodes, interior nodes, and stream nodes. Within the model, the points file is used to construct the Voronoi mesh where each Voronoi polygon is a computational element. In areas of complex terrain and high network density, errors typically occur in tRIBS drainage network representation and stream nodes and interior nodes must be added to force the network to the drainage path created in a GIS. The most encountered problem is a stream network that crosses a subwatershed divide where ridges are poorly represented within the TIN. Adding interior nodes where stream networks should not occur and adding

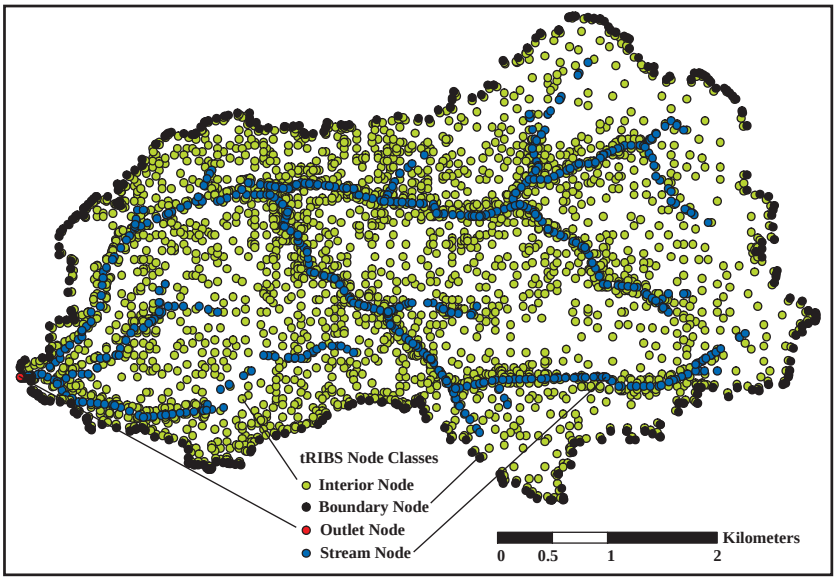

Figure 4.3 Point File Example For Small Test Basin

supplementary stream nodes where the network is supposed to drain typically constrains the stream reach to the proper location.

In the calibrated model for the Upper Río Puerco, ~258 points were added to ensure accurate tRIBS stream network representation. Additional model simulations that introduced alternative constant area thresholds to generate the Upper Río Puerco stream network required a new TIN and a new points file. Point corrections were also conducted for these models to resolve inconsistencies between GIS and tRIBS stream network representations.

4.3 Land Cover Data

tRIBS possesses mathematical representations of surface energy balance, evapotranspiration, and rainfall interception that require parameter values based upon land cover type (see Chapter 2). The 1992 National Land Cover Dataset (NLCD 92)

provides land cover classifications in a 30 m resolution raster-based format that are easily incorporated into the tRIBS model. The dataset is derived from Landsat imagery and supplemented with topographic, agricultural, census, and wetlands data as well as other land cover maps (http://seamless.usgs.gov). The NLCD 92 includes twenty-one different land cover types, which are reclassified before running tRIBS simulations.

tRIBS land cover types are numbered from 1 to *n*, with *n* being the total number of reclassified land cover types. Each number corresponds to a row in a text file that contains eleven different land cover parameter values (Table 4.1). Actual parameter values used in the Upper Río Puerco simulations are discussed in Section 4.8.2. Land cover reclassification was performed for the Upper Río Puerco according to the following design. The corresponding parameter table identification number is provided in parentheses.

The Upper Río Puerco tRIBS land cover reclassifications, water (1), shrublands (5), grasslands (6), and emergent herbaceous wetlands (8) were not altered from the NLCD 92. However, low intensity residential, commercial/industrial/residential, and urban/recreational classes from the original dataset were combined to form an urban land cover type (2). In addition, deciduous forest, evergreen forest, and mixed forest were collectively defined as forest (4). This classification could have also been listed as evergreen forest since the evergreen forest class constitutes 99.1% of all forest types in the Upper Río Puerco. Bare rock/sand/clay and quarries/strip mines/gravel pits were reclassified as bare soil (3). Finally, pasture, row crop, and fallow designations were consolidated into an agriculture class (7).

	a	b1	P	S	K	g	Al	h	K_t	r_s	V
1											
2											
3...											
n											

Parameter	Description	Units
a	Canopy Storage - Storage	[mm]
b1	Interception Storage - Storage	[-]
P	Free Throughfall Coefficient -Rutter	[-]
S	Canopy Field Capacity -Rutter	[mm]
K	Drainage Coefficient - Rutter	[mm/hr]
g	Drainage Exponential Parameter - Rutter	[mm^{-1}]
Al	Albedo	[-]
h	Vegetation Height	[m]
K_t	Optical Transmission Coefficient	[-]
r_s	Canopy-Average Stomatal Resistance	[s/m]
V	Vegetation Fraction	[-]

Table 4.1 (a) An example of the format for the land cover parameter table used in the tRIBS Hydrologic Model (b) Parameter Value Descriptions (after *Ivanov et al.*, 2004b). The Rutter method for rainfall interception was discussed in Chapter 2. Storage refers to a canopy storage approach for rainfall interception that was not used in this study.

Figure 4.4 shows land cover types prior to and following reclassification for the Upper Río Puerco. Although eight consolidated land cover types were created from the NLCD 92, tRIBS land cover representation in the Upper Río Puerco watershed is primarily allocated between shrubland (29.44%), grassland (29.22%), and forest (39.27%). Once reclassification was complete, the raster grid was converted to an ASCII text file that tRIBS calls for each simulation performed.

4.4 Soil Texture

As with land cover data, soil properties also require representation at each node within the model domain. Spatial distribution of soil texture is available in GIS format from the National Resource Conservation Service (NRCS) State Soil Geographic Database (STATSGO), which was first published in 1994. Reclassification of soils is not as straightforward as the reclassification of land cover data. Within the STATSGO dataset each soil map unit contains a unique distribution of soil texture. That is, a unit might contain 35% clay loam, 30% loam, 20% sandy loam, and 15% very cobbly loam. Frequently, a map unit fails to exhibit an overwhelming tendency towards a single soil texture. In order to limit the number of soil texture classes, any map unit including gravelly, cobbly, or stony in its soil description was reduced to its base soil texture. In the scenario provided above, this would result in a map unit with 45% loam (35% loam + 15% very cobbly loam) and the entire corresponding region would be reclassified as merely a loam. Figure 4.5 provides STATSGO soil map units and includes soil textures prior to reclassification (a) as well as soil texture distribution following data aggregation for input into tRIBS (b). Following soil reclassification, the new soils map was converted

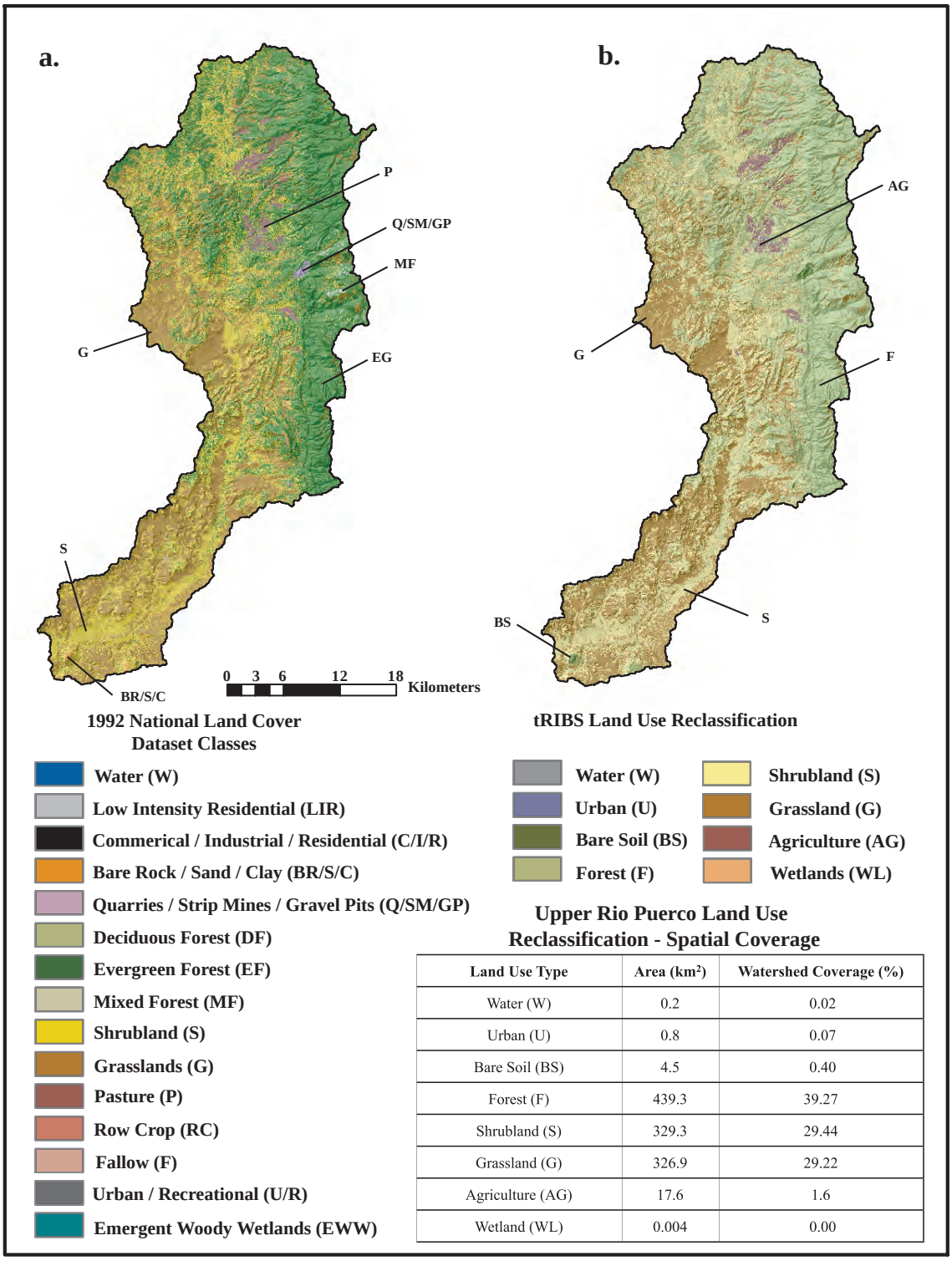

Upper Rio Puerco Land Use Reclassification - Spatial Coverage

Land Use Type	Area (km²)	Watershed Coverage (%)
Water (W)	0.2	0.02
Urban (U)	0.8	0.07
Bare Soil (BS)	4.5	0.40
Forest (F)	439.3	39.27
Shrubland (S)	329.3	29.44
Grassland (G)	326.9	29.22
Agriculture (AG)	17.6	1.6
Wetland (WL)	0.004	0.00

Figure 4.4 (a) National Land Cover Dataset (1992) classifications for the Upper Río Puerco (b) Land Cover types used for hydrologic simulations following data reclassification

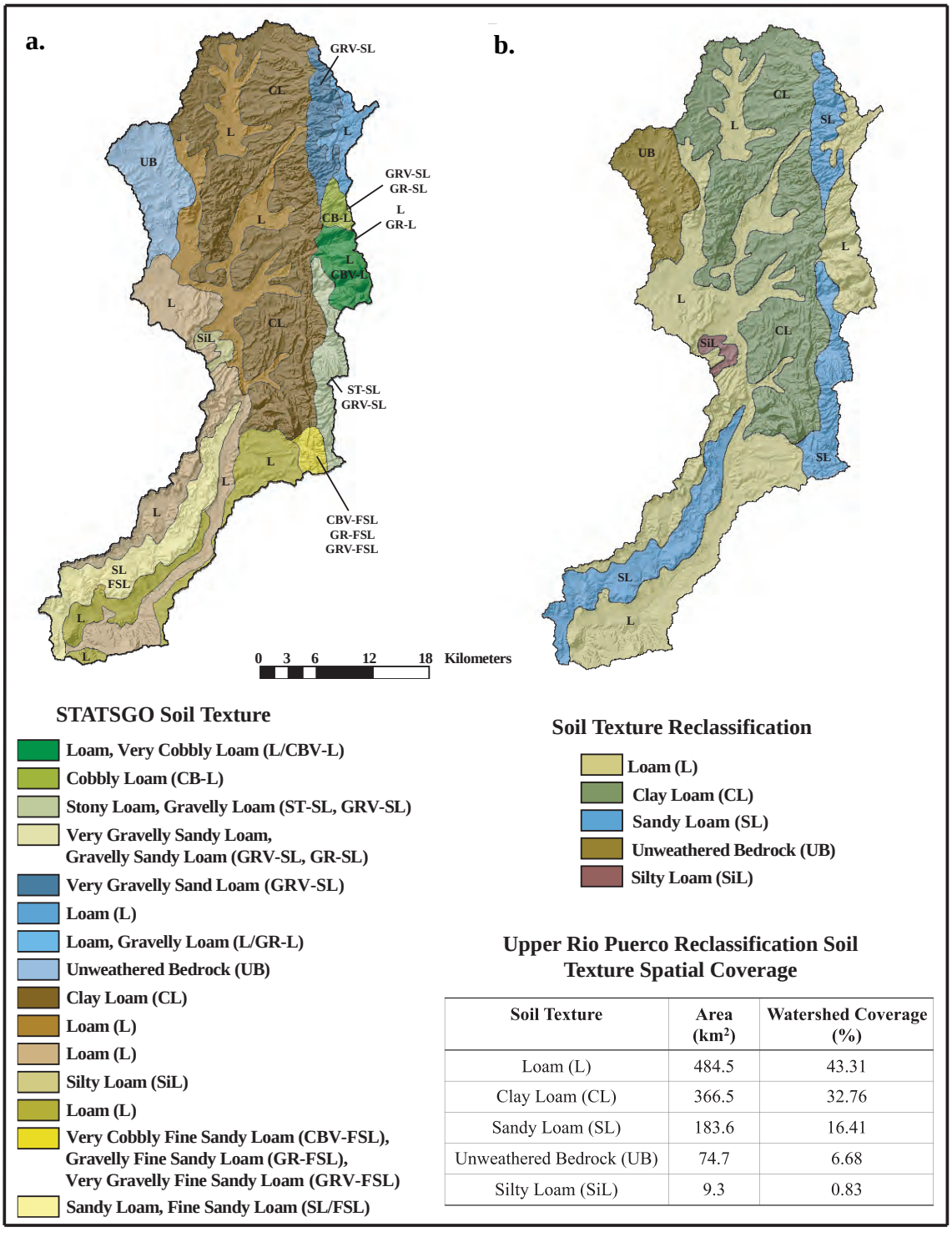

Upper Rio Puerco Reclassification Soil Texture Spatial Coverage

Soil Texture	Area (km^2)	Watershed Coverage (%)
Loam (L)	484.5	43.31
Clay Loam (CL)	366.5	32.76
Sandy Loam (SL)	183.6	16.41
Unweathered Bedrock (UB)	74.7	6.68
Silty Loam (SiL)	9.3	0.83

Figure 4.5 (a) State Soil Geographic Database soil classes (b) Soil texture classes used for hydrologic simulations following data reclassification

to an ASCII file that is used in all hydrologic simulations of the Upper Río Puerco.

Each soil texture type in the ASCII file is assigned a number 1 through *n*, with *n* being the total number of soil textures. Following soil reclassification, five soil textures were included in the Upper Río Puerco tRIBS model. These included loam (2), clay loam (3), sandy loam (4), unweathered bedrock (8), and silty loam (12), although silty loam covered a very small fraction of the total basin area. The region of unweathered bedrock corresponds to the Tertiary San Jose Formation in Figure 3.3. The number in parentheses following each soil texture indicates the soil identification number in the table of parameter values (Table 4.2). The identification numbers are not in numerical order because the table originally contained reclassified soil textures from both the Upper Río Puerco and the Jemez River watersheds. As with the land cover reclassification, a text file lists each soil texture number and its associated parameter values.

4.5 Bedrock Representation

Depth to bedrock is established using STATSGO data (Figure 4.6a). STATSGO bedrock information is derived from field measurements performed with a rod that penetrates into the soil layer. If the rod encounters bedrock before a depth of 60 inches (1.5 m), then the measurement depth is recorded. However, if bedrock is not detected, then STATSGO assigns a maximum depth of 1.5 m. Measurement locations in the Upper Río Puerco and the overall accuracy of the STATSGO bedrock data were not available.

In tRIBS, the bedrock layer is impermeable and acts as a barrier to the vertical redistribution of soil moisture. If bedrock outcrops are present at the land-atmosphere

	K_s	Θ_s	Θ_r	m	ψ_b	f	A_s	A_u	n	k_s	C_s
1											
2											
3...											
n											

Parameter	Description	Units
K_s	Saturated Hydraulic Conductivity	[mm/hr]
Θ_s	Soil Moisture at Saturation	[-]
Θ_r	Residual Soil Moisture	[-]
m	Pore Distribution Index	[-]
ψ_b	Air Entry Bubbling Pressure	[mm] (negative)
f	Decay Parameter	$[mm^{-1}]$
A_s	Saturated Anisotropy Ratio	[-]
A_u	Unsaturated Anisotropy Ratio	[-]
n	Porosity	[-]
k_s	Volumetric Heat Conductivity	$[J/m \cdot s \cdot K]$
C_s	Soil Heat Capacity	$[J/m^3 \cdot K]$

Table 4.2 (a) An example of the soil parameter table used in the tRIBS Hydrologic Model (b) Parameter Value Descriptions (after *Ivanov et al.*, 2004b).

interface, tRIBS prevents infiltration into the soil layer and all rainfall is converted to runoff. Infiltration due to fracture flow or low permeability is currently not incorporated within tRIBS bedrock representation. Consequently, the decision was made to arbitrarily increase bedrock depth and allow rainfall infiltration and runoff rates based upon soil texture parameters .

Regions of unweathered bedrock in the soil texture dataset correspond to

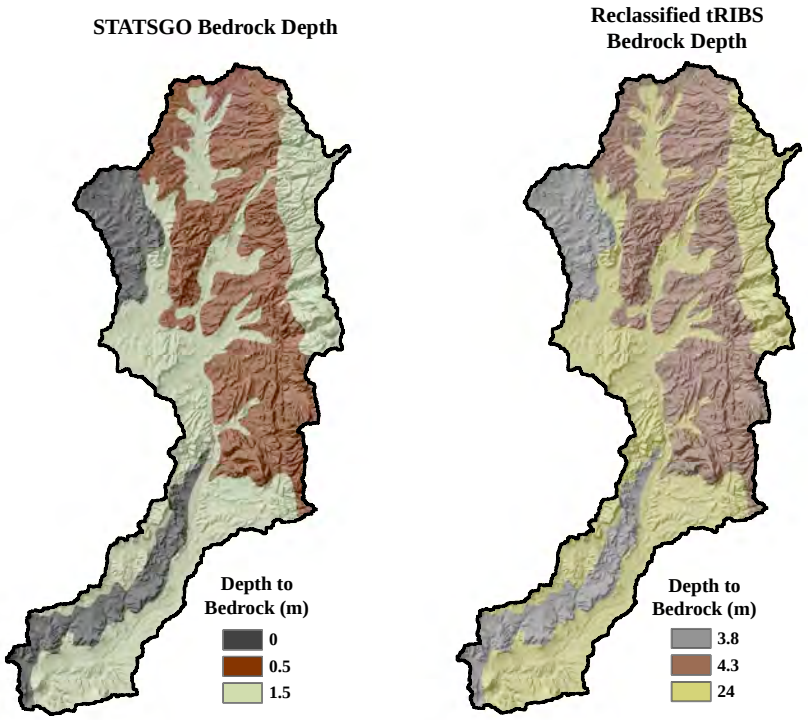

Figure 4.6 (a) STATSGO bedrock data (b) tRIBS Bedrock depth based upon STATSGO Dataset

STATSGO bedrock depth equal to 0 m. Rather then utilize a completely impervious layer at the land surface, tRIBS utilizes a bedrock depth of 3.8 m wherever STATSGO depth indicates bedrock depth at 0 - 0.49 m. This allows bedrock representation through soil texture parameterization. Soil texture parameters values for unweathered bedrock are indicative of a sandstone formation based upon literature values (see Section 4.8.2). STATSGO bedrock depth of 0.5 m corresponds to regions of clay loam soil texture in Figure 4.5. Bedrock depth over this area was also lowered an additional 3.8 m to increase the depth of the soil profile. Regions in the STATSGO dataset with bedrock depths of 1.5 m were reclassified to a depth of 24 m. Figure 4.6b shows reclassified bedrock depths. After reassigning new depths, the bedrock data was converted from a GIS shapefile to an ASCII file and used for all tRIBS simulations.

4.6 Precipitation Data

One of the primary motivations behind tRIBS model development was to capitalize on spatially and temporally distributed precipitation data provided by Next Generation Weather Radar WSR-88 (NEXRAD) (*Ivanov et al.*, 2004b). NEXRAD data from the National Weather Service (NWS) is available with different levels of preprocessing, calibration, and quality control (*Xie et al.*, 2005). This study uses Stage III rainfall data, which combines precipitation estimates from multiple radars spaced across the NWS West Gulf River Forecast Center (WGRFC). The data are checked against multiple rain gauges for accuracy and meteorological quality control is performed by trained personnel at each RFC (*Xie et al.*, 2005). The WGRFC Stage III radar product covers most of Texas and New Mexico and includes the entire Río Grande watershed north of the U.S.-Mexico border.

Radar data provided by the WGRFC is not amenable to visualization and analysis within a GIS due to the projection, file size, and multiple compression storage system (*Xie et al.*, 2005). *Xie et al.* (2005) reprojected several years of WGRFC NEXRAD Stage III data from Hydrologic Rainfall Analysis Project (HRAP) coordinates to a Universal Transverse Mercator (UTM) coordinate system. The dataset was also converted to a raster format that allows radar data visualization and analysis within a GIS.

Precipitation grids from June through October of 2003 were obtained from the *Xie et al.* (2005) dataset. However, the 4 km by 4 km spatial resolution and hourly time interval raster grids that covered the WGRFC region imposed large storage requirements

and included unnecessary rainfall data. An AML script clipped each hourly WGRFC radar grid to both the Upper Río Puerco boundary and to a region slightly larger than the accumulated area of the Upper Río Puerco, Torreon Wash, and Arroyo Chico (ATU). The script also applied a time stamp conversion that removed the original Mean Greenwich Time stamp and renamed each radar dataset using a Mountain Daylight Time mmddyyyyhh format. Each grid was reprojected to a NAD 27 datum and UTM Zone 13 projection to match other spatial datasets used in this study. Finally, the AML script converted each ATU hourly radar grid to an ASCII format for tRIBS hydrologic simulations. tRIBS resamples the ASCII file to the Upper Río Puerco boundary prior to calculations performed within a given time step.

Despite the high spatial and temporal resolution offered by NEXRAD, the accuracy of radar estimated rainfall remains a focus of investigation (see *Xie et al.*, 2006). For the Sevilleta Long-Term Ecological Research (LTER) facility just north of Socorro NM, *Xie et al.* (2006) found the NEXRAD Stage III WGRFC product overestimates the hourly conditional mean (nonzero values) across all seasons and overestimates rainfall accumulation during the monsoon season when compared to data collected by a rain gauge network. To investigate possible errors in radar estimates over the Upper Río Puerco, radar time series were compared to precipitation from the National Climatic Data Center (NCDC) rain gauge located in Cuba, NM.

Figure 4.7a shows the Cuba, NM rain gauge precipitation time series for June through October 2003. Hourly rainfall values from the rain gauge are reported in units of one tenth of an inch and were converted to millimeters to match the units used in the

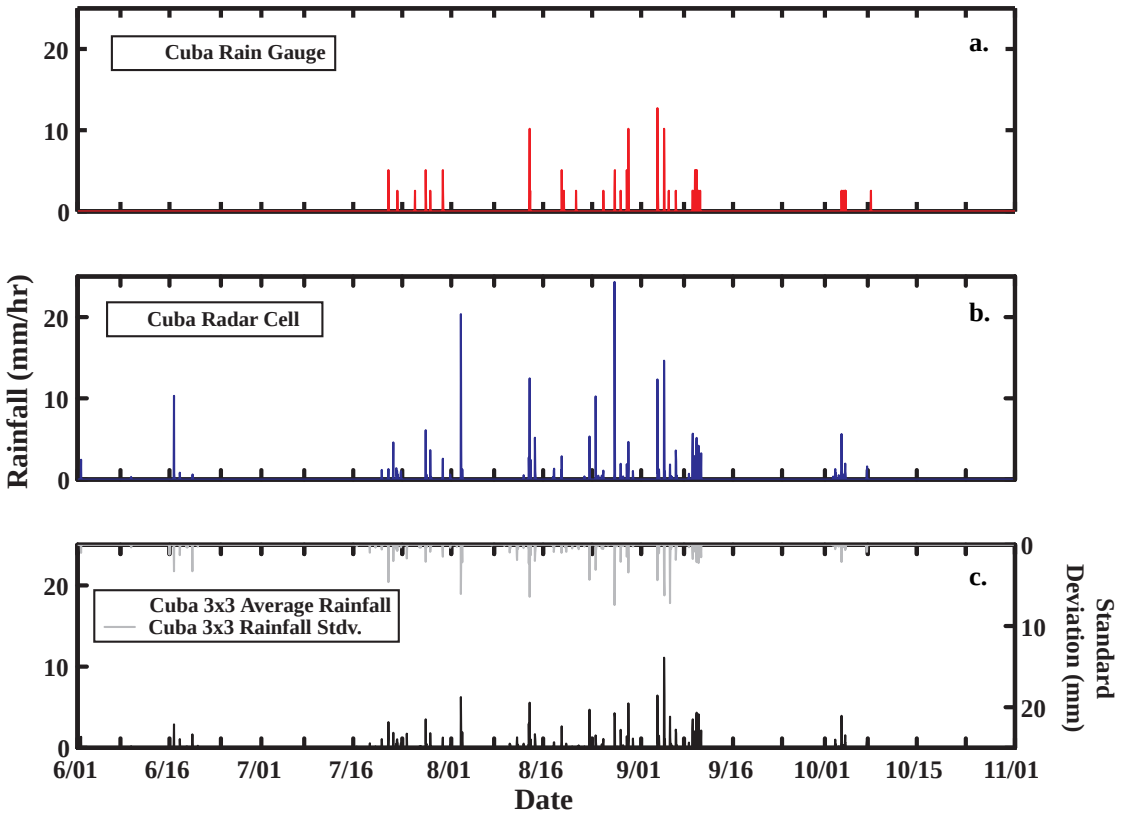

Figure 4.7 Rain Gauge and Radar Precipitation Time Series - June through October 2003. (a) National Climatic Data Center (NCDC) Cuba, NM rain gauge hourly precipitation data (b) NEXRAD pixel hourly precipitation time series that corresponds with Cuba, NM rain gauge location (c) Average hourly precipitation for the NEXRAD 3x3 pixel region with Cuba, NM at the center

NEXRAD Stage III product. Figure 4.7b plots the time series for the radar pixel that coincides with the latitude-longitude coordinates of the Cuba, NM rain gauge. The NEXRAD Stage III product includes rainfall estimates during the month of June that are not observed at the Cuba rain gauge. In Figure 4.7c, the Cuba 3x3 average rainfall is the mean precipitation value calculated from the Cuba radar pixel as well as the eight surrounding radar pixels. Since the Cuba pixel is included in the mean hourly rainfall calculation, the 3x3 regional average also contains precipitation during June that fails to appear in the rain gauge record. The standard deviation calculated using all nine pixels

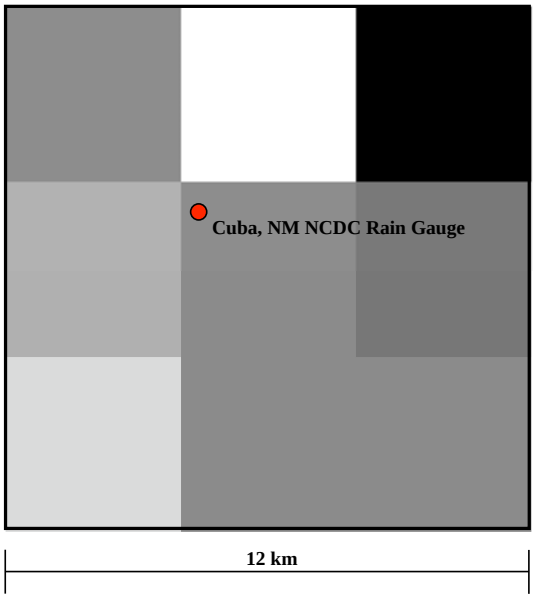

Figure 4.8 Radar 3x3 Pixel Region and NCDC Cuba, NM Rain Gauge

shows that rainfall rates are variable in space, which is typical of NAM monsoon events (see Section 3.5). Figure 4.8 shows the 3x3 radar grid, including the radar pixel that lies over the NCDC Cuba rain gauge.

Cumulative precipitation totals for the Cuba rain gauge, the Cuba radar pixel, and the average precipitation from the Cuba 3x3 region are presented in Figure 4.9. The Cuba radar cell exhibited 281 mm of cumulative rainfall over the the summer of 2003. The average of the nine radar pixels and the Cuba rain gauge had cumulative precipitation totals of 202 mm and 173 mm respectively. The difference between the total monsoon rainfall estimated by the single NEXRAD Stage III pixel and the rainfall measured at the NCDC rain gauge station suggests that radar may overestimate total monsoon precipitation in the Upper Río Puerco near Cuba, NM. It is also possible that the various geographic transformations applied to the radar data causes the incorrect cell to coincide with the rain gauge location. The better agreement between the 3x3 regional

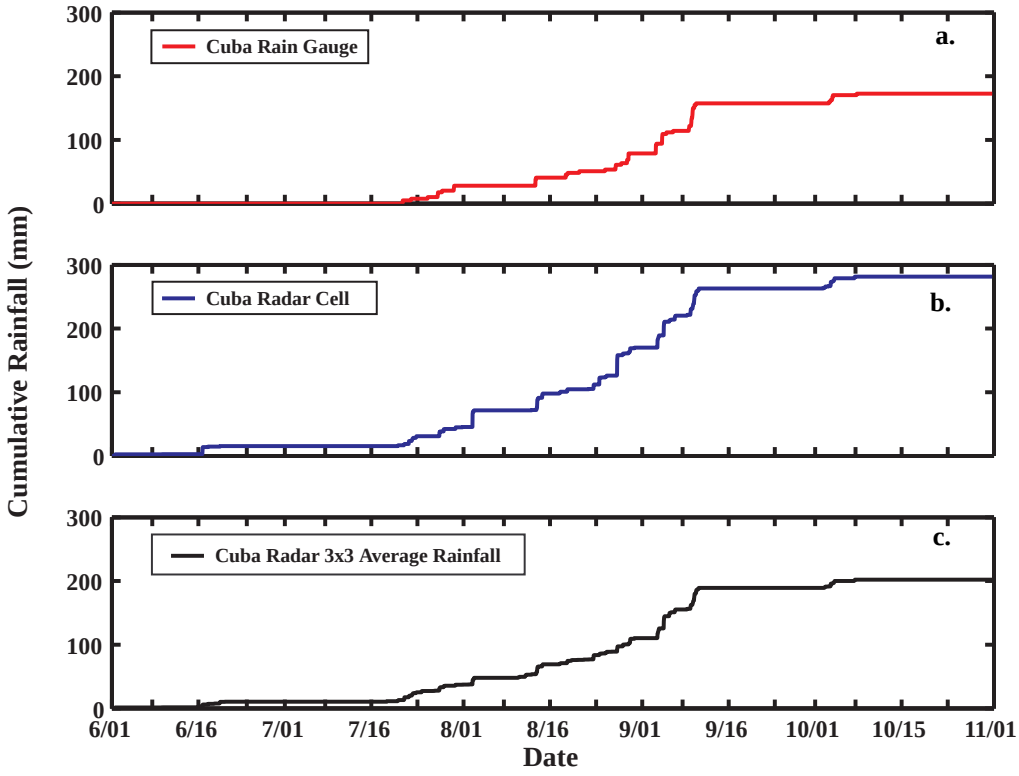

Figure 4.9 Cumulative Rainfall Totals for June through October 2003 (a) NCDC Cuba, NM rain gauge (b) Rainfall total from Cuba, NM NEXRAD WGRFC Stage III radar pixel (c) Rainfall total for the NEXRAD 3x3 pixel region with Cuba, NM pixel at the center

cumulative mean and the rain gauge data lends support to this possibility. However, similarities could also be a result of compounding underestimations and overestimations across the nine grid cells through time that ultimately result in similar monsoon rainfall totals. Without a dense rain gauge network, it is difficult to determine whether inconsistencies emerge from geoprocessing or NEXRAD estimation error.

Table 4.3 divides the Cuba rain gauge, Cuba radar cell, and the Cuba 3x3 region precipitation record into three distinct time periods: June 15 - August 2; August 5 - August 31; and September 3 - September 11. These dates correspond to three well-defined clusters of precipitation events in the Cuba rain gauge precipitation record

June 15 - August 2, 2003

	Number of Rainfall Events	Total Rainfall (mm)	Conditional Mean
Rain Gauge	8	27.94	3.49
Cuba Cell	26	56.26	2.16
Cuba 3x3 Average	50	37.55	0.75

August 5 - August 31, 2003

	Number of Rainfall Events	Total Rainfall (mm)	Conditional Mean
Rain Gauge	11	50.8	4.62
Cuba Cell	35	99.4	2.84
Cuba 3x3 Average	79	62.4	0.79

September 3rd - September 11, 2003

	Number of Rainfall Events	Total Rainfall (mm)	Conditional Mean
Rain Gauge	18	78.74	4.37
Cuba Cell	38	92.99	2.44
Cuba 3x3 Average	50	78.82	1.57

Table 4.3 Number of Rainfall Events, Total Rainfall and the Conditional Mean from each subinterval of the precipitation record.

(Figure 4.7a). The rainfall totals for the Cuba rain gauge, the Cuba radar cell, and the Cuba 3x3 regional average were calculated for each subinterval of the precipitation record. Additionally, within each time period, a rainfall event occurs if precipitation over the hour interval is greater than zero. Then, the conditional mean rainfall per event (CM) is given by:

$$CM = \frac{\text{Total Rainfall}}{\text{Number of Rainfall Events}}. \qquad 4.2$$

Results demonstrate that for all three periods analyzed, the precipitation time

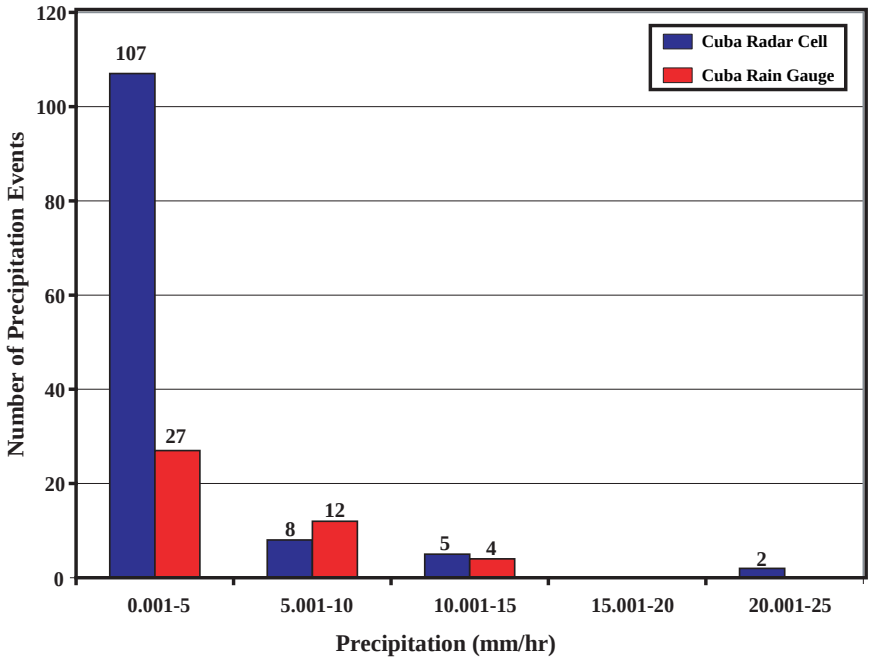

Figure 4.10 Number of hourly precipitation events grouped by intensity for the Cuba, NM NEXRAD pixel and the NCDC Cuba, NM rain gauge

series derived from the Cuba radar pixel includes substantially more rainfall events than the NCDC Cuba rain gauge data. The Cuba 3x3 regional rainfall mean time series had the most precipitation events presumably due to the larger sampling area. Rainfall totals for each subinterval of the precipitation record were highest for the radar pixel located over Cuba, NM. The total mean rainfall from the 3x3 pixel sample is less than the accumulated rainfall from the single Cuba radar pixel. This occurs because the Cuba pixel generally possesses higher hourly rainfall totals than the surrounding grid cells. Finally, despite the higher rainfall accumulation, the Cuba radar pixel CM was less than the rain gauge CM. This suggests that the differences between the Cuba radar pixel and rain gauge rainfall totals are primarily due to more frequent low intensity events recorded by NEXRAD which are not observed in the rain gauge precipitation record (Figure 4.10).

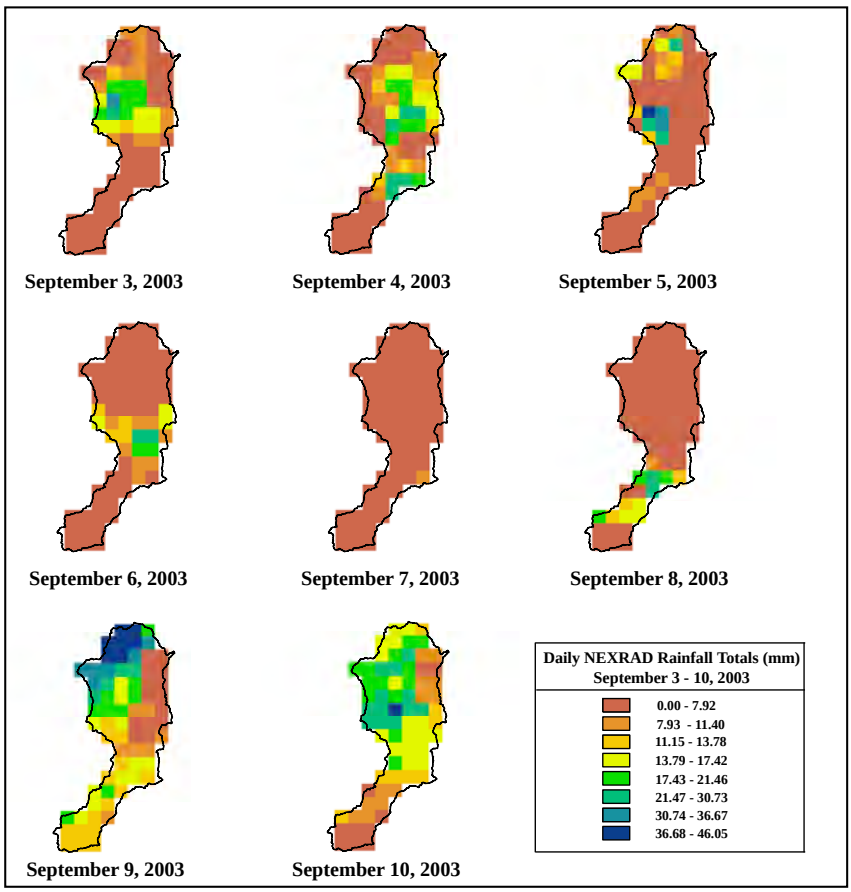

Figure 4.11 Daily NEXRAD rainfall estimation totals, which lead to the September 2003 flood event

Known problems with NEXRAD radar include treating virga, or precipitation that evaporates before reaching the land surface, as rainfall at ground level. The distance from the NEXRAD radar in Albuquerque, NM, may result in a high radar beam angle over the Upper Río Puerco near Cuba, NM. A large beam angle could lead to overestimation of monsoon rainfall totals and number of events due to the occurrence of virga.

An additional problem with NEXRAD radar estimates in the Upper Río Puerco is the possibility of a rain shadow in the northeast corner of the watershed. Figure 4.11

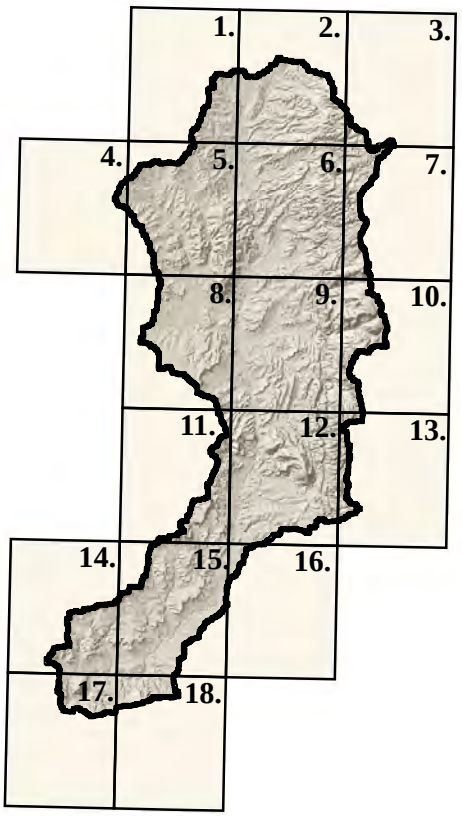

7.5′ Quadrangle Number	7.5′ Quadrangle Name	7.5′ Quadrangle Number	7.5′ Quadrangle Name
1	Five Lakes Canyon NE	10	Rancho del Chaparral
2	Regina	11	Headcut Reservoir
3	Gallina	12	La Ventana
4	Taylor Ranch	13	San Miguel Mountain
5	Arroyo Chijuillita	14	Arroyo Empedrado
6	Cuba	15	San Luis
7	Nacimiento Peak	16	Holy Ghost Spring
8	Mesa Portales	17	Guadalupe
9	San Pablo	18	Cabezon Peak

Figure 4.12 United States Geological Survey (USGS) Quadrangles for the Upper Río Puerco (http://rgis.unm.edu)

shows the daily rainfall totals that preceded the flood event of September 2003 discussed in Section 3.5.1. Despite heavy rainfall on September 9 and September 10 throughout most of the watershed, rainfall totals are consistently lower in regions that correspond to the Cuba and Nacimiento USGS Quadrangles in Figure 4.12 (Quadrangle Numbers 6 & 7). The presence of a NEXRAD rain shadow would be expected here since mountain peaks in the southern portions of these quadrangles reach upwards of 10,300 ft (3139 m) with elevation decreasing to the north and west. Complex terrain may block the radar beam in the northeastern portions of the Sierra Nacimiento leading to underestimation of rainfall on the mountain front.

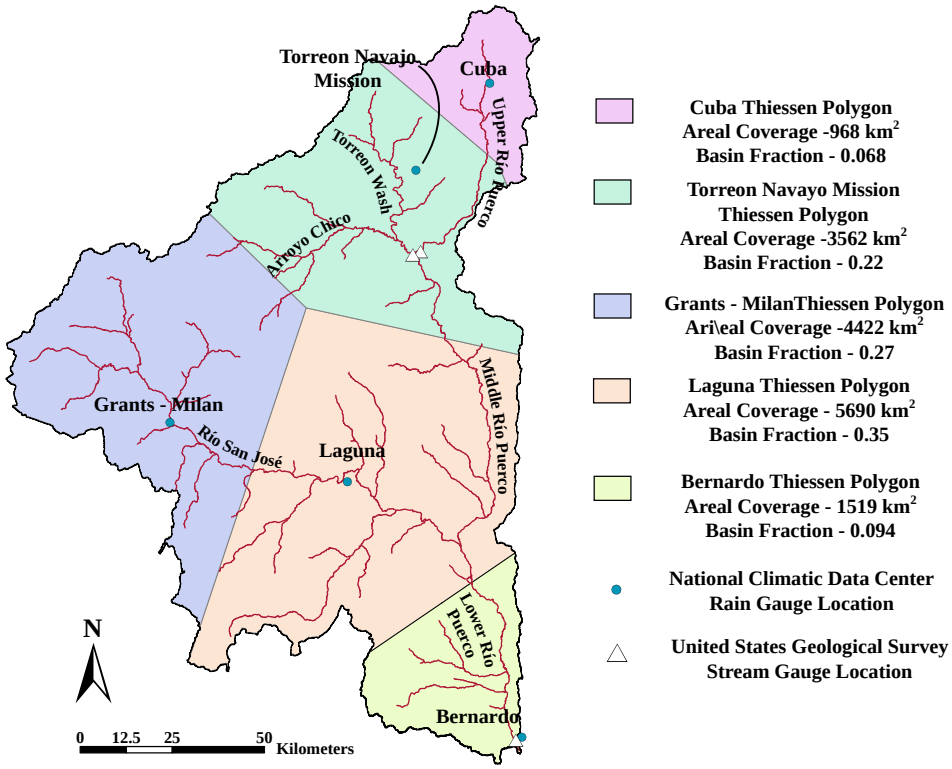

Figure 4.13 Thiessen Polygons generated from NCDC Rain Gauges in the Río Puerco

Although problems exist with the NEXRAD radar product used for tRIBS calibration, the limited number of rain gauges in the region would not provide adequate spatial distribution to capture variability of monsoon rainfall events. Figure 4.13 shows Thiessen polygons created for the entire Río Puerco based upon NCDC rain gauges in the watershed. For the Upper Río Puerco, ~ 812 km^2 (73% of the watershed) falls within the Cuba Thiessen Polygon whereas ~300 km^2 (37% of the watershed) is inside the Torreon Navajo Mission Thiessen Polygon. Consequently, if rain gauge records were used to force the tRIBS model, the southern portion of the Upper Río Puerco would only experience rainfall as indicated by the Torreon Navajo Mission rain gauge. The Torreon Navajo Mission rain gauge is a significant distance from the Upper Río Puerco and to

accept that monsoon rainfall in Torreon Wash is representative of rainfall in the southern portions of the Upper Río Puerco is likely an incorrect assumption. Moreover, within the tRIBS model, rainfall would only occur in the basin when rainfall was observed at one of the rain gauges. Any rainfall that may have occurred in other portions of the watershed and was not captured by either the Cuba rain gauge or the Torreon Navajo Mission rain gauge would not be represented. So, for this study, NEXRAD Stage III rainfall estimates are used to force tRIBS and any errors within the data are incorporated into the model and propagated through the simulations.

4.7 Meteorological Data

tRIBS requires hourly meteorological data including atmospheric pressure, dew point temperature or relative humidity, sky cover, wind speed, and air temperature. Like other parameter values, a table in text file format is created and read by tRIBS. For the summer of 2003, the required atmospheric parameters are not provided by the NCDC rain gauge at Cuba, NM. The closest NCDC station that records meteorological data is Grants-Milan Municipal Airport (Figure 3.1). For tRIBS simulations of the Upper Río Puerco, atmospheric pressure, relative humidity, wind speed, and air temperature values were obtained from the Grants-Milan weather station. Sky cover was obtained from Albuquerque International Airport.

tRIBS requires sky cover input on a scale from 0 (no clouds) to 10 (overcast). NCDC provides different sky cover observations which include clear skies, few clouds, scattered clouds, broken clouds, and overcast skies. The NCDC describes each

classification as follows: clear implies no clouds below 12,000 ft; few is $^{0}/_{8}$ - $^{2}/_{8}$ sky cover; scattered is $^{3}/_{8}$ - $^{4}/_{8}$ cloud cover; broken is $^{5}/_{8}$ - $^{7}/_{8}$ cloud cover; and overcast is $^{8}/_{8}$ sky cover. Within tRIBS the clear skies designation was given a value of zero, few clouds condition was assigned a value of 3, scattered clouds was given a value of 5, broken skies were designated as 8, and overcast skies were assigned a value of 10. Whenever tRIBS detects rainfall over a Voronoi polygon, cloud cover is automatically set to 10 for that model element.

Frequently, the NCDC provides different sky covers for various heights above ground level. As a result, assignment of cloud cover for multiple sky conditions was difficult. When mixed sky descriptions were provided, the lowest to middle sky condition typically was chosen for that time step. If a lower sky fraction had been repeated for multiple hours prior to the time step of consideration, then the lower sky cover fraction was usually chosen as the value for that hour. Often conditions could have legitimately been assigned a cloudier condition. This was not done for concern regarding the accuracy of the NCDC dataset. When parameter values were set using either the mean or maximum cloud cover, the dataset became overly cloudly to such an extent that the NCDC observations seemed unrealistic for summer months in a semi-arid environment.

Also note that cloud cover at Albuquerque International Airport is not representative of sky cover over the Upper Río Puerco so the errors incurred from potentially misjudged sky cover is likely insignificant relative to the error due to the distance from the Upper Río Puerco. As an alternative, examination of the western US

Geostationary Satellite visible (daytime hours) and infrared (nighttime hours) products would provide more accurate cloud cover classification for watersheds without meteorological observations.

4.8 tRIBS Model Calibration

One of the initial motivations for physically-based hydrologic model development was simplification of parameter value identification as physically-based parameters were constrained through improved field observations (*Downer et al.*, 2002). However, optimism surrounding improved distributed model performance through governing equations that use physically-based parameters has not been fully realized (see *Reed et al.*, 2004). Distributed models inherently require an intensive amount of spatially and temporally distributed data and fulfilling the demands for parameter values derived from field measured values is not typically feasible since most watersheds suffer from low data availability. Consequently, many users of distributed models assign parameter values found in the literature and then adjust parameter values to improve the fit between a modelled hydrograph and stream gauge data (*Downer et al*., 2002; *Ivanov et al*., 2004b).

Previous applications of the tRIBS model have not utilized parameter values determined by field measurements for the basin of interest (*Ivanov et al*., 2004a, 2004b). Parameter values have been assigned based upon published values and are then calibrated to approximate modelled results with observed streamflow. The following sections describe model calibration approach, assignment of parameter values, and final results for the Upper Río Puerco 2003 monsoon storm event simulations.

4.8.1 Calibration Approach

Although parameter optimization routines are in development, the tRIBS model currently relies on a manual calibration approach. Due to the number of parameters found in tRIBS, not all parameter values are adjusted during model calibration. *Ivanov et al.* (2004b) suggested a methodology focused on achieving reasonable model results through calibration of parameters bearing the greatest influence on tRIBS sensitivity. Similar techniques have been applied with the CASC2D distributed model in semi-arid watersheds (*Downer et al.*, 2002). tRIBS calibration begins for a single flood event with efforts focused on varying saturated hydraulic conductivity (K_s), conductivity decay parameter (f), and anisotropy ratio (A_s and A_u) values to achieve a reasonable modelled hydrograph. If rainfall occurs over a specific portion of the basin, only soil textures experiencing significant amounts of precipitation may require calibration.

Once the model hydrograph for a single flood event is considered acceptable, calibration efforts move to longer periods of the streamflow record and attempt to simulate multiple flood events. Typically, additional parameter adjustment is required during this step to account for naturally occurring changes in antecedent watershed conditions prior to rainfall-runoff events. In addition, hydrograph timing may require improvement through the calibration of routing parameters. These include Manning's η (Eq. 2.33) and hillslope runoff velocity parameters (c_v and r found in Eq. 2.31).

Calibration of hillslope velocity parameters may be especially important for watersheds demonstrating runoff production through the infiltration excess mechanism.

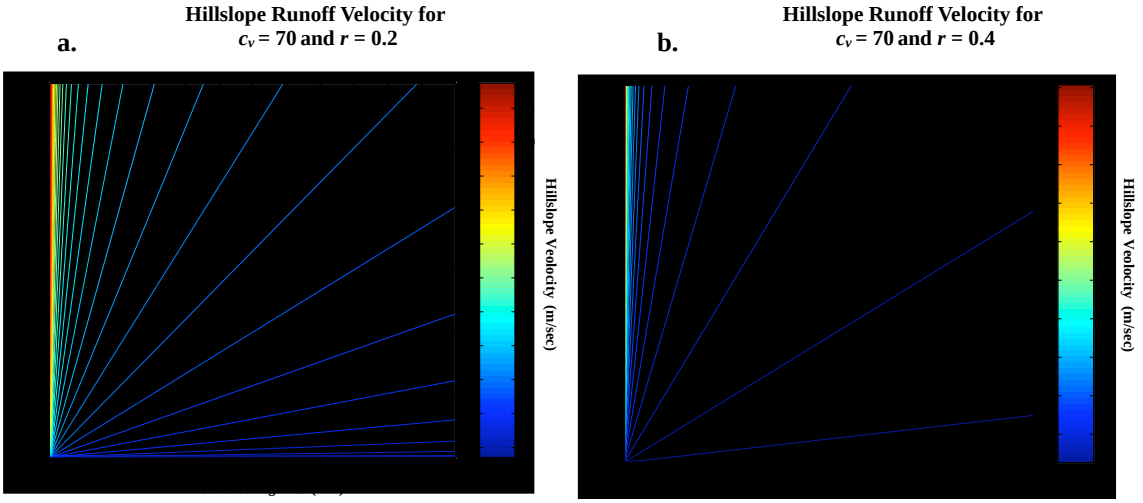

Figure 4.14 Comparison of Hillslope Velocity Due to Changes in the Hillslope Runoff Exponent

However, calibrating these parameters requires a great deal of caution since slight changes in parameter values can substantially alter hillslope runoff velocities. Inaccurate calibration can lead to better agreement between simulated and observed streamflow data at the cost of introducing unrealistic hillslope runoff rates. For example, Figure 4.14 shows runoff velocities for different hillslope runoff routing exponents. When the hillslope exponent (r) equals 0.2, runoff velocities can reach 3 m/s - 6 m/s for subbasins possessing contributing area less than ~ 300 km^2 (Figure 4.14a). High hillslope velocities may compensate for late runoff production at Voronoi elements or channel routing parameterizations that underestimate streamflow velocities. In addition, high hillslope velocities transfer the dominant model routing mechanism from the channel to the hillslope such that model sensitivity to variation in channel network density may become minimal. This occurs because hillslope velocities reach magnitudes similar to in-channel streamflow velocities. Consequently, runoff produced at a given point in the simulated watershed can consistently reach the basin outlet at roughly the same point in time

regardless of channel network density. Hillslope velocities for the parameterized Upper Río Puerco model are shown in Figure 4.14b. These parameter values are obtained from the *Ivanov et al*. (2004a) tRIBS model calibration for the Baron Fork watershed in northeastern Oklahoma.

Ivanov et al. (2004b) suggested that long inter-storm periods are suitable for calibration of the canopy average stomatal resistance (r_s) and vegetative fraction (v) land cover parameters. However, monsoon events during September 2003 produced flood events characterized by short inter-storm periods. In addition, increased cloud cover and heavy precipitation associated with monsoon events are thought to minimize the importance of evaporative fluxes during periods of flood generation. Thus, parameters associated with evapotranspiration are assigned values but are not involved in model calibration.

4.8.2 Parameter Value Data Sources and Calibrated Values

Spatially distributed field-based parameter values necessary for tRIBS simulations are unavailable for the Upper Río Puerco. As a result, parameter values are either obtained from the literature or assigned values based upon inference. For example, many tRIBS land cover parameter values are unavailable for vegetation types found in semi-arid environments. Consequently, some parameters values are assigned following consideration of potential differences between the plant species in a published field study and vegetation indigenous to the semi-arid climate found in the Upper Río Puerco.

Table 4.4 provides parameter values for land cover types found in the Upper Río

	P (-)	S (mm)	K (mm/hr)	g (mm^{-1})	Al (-)	h (m)	K_t (-)	R_s (s/m)	V (-)
Water	1.00	1.0	0.01	3.7	0.04	0.01	1.00	0.0	0.95
Urban	1.00	1.0	0.01	3.7	0.20	8.00	1.00	0.0	0.95
Bare Soil	1.00	1.0	0.01	3.7	0.30	0.01	1.00	0.0	1.00
Forest	0.48	2.4	0.12	3.7	0.15	12.0	0.45	200	0.80
Shrubland	0.70	1.5	0.20	3.9	0.16	0.75	0.55	100	0.45
Grassland	0.85	0.8	0.10	4.2	0.13	0.18	0.70	050	0.45
Agriculture	0.75	0.8	0.10	3.6	0.20	0.40	0.65	075	0.65
Wetlands	0.90	1.0	0.10	3.6	0.14	0.50	0.50	100	0.60

Table 4.4 Land Cover Parameter Values for the Upper Río Puerco tRIBS Model

Puerco calibrated model. Parameters *p* (free throughfall coefficient), *S* (canopy capacity), *K* (canopy drainage rate coefficient), and *g* (canopy drainage exponent) correspond to calculations performed within the Rutter Interception Model. Semi-arid rainfall interception studies using the Rutter Model could not be located, so parameters were assigned values thought to be reasonable for vegetation found in the Upper Río Puerco. Parameter values for a Corsican pine found in *Rutter* (1971) provided initial guidance for parameter calibration.

For this study, water, bare soil, and urban land cover types are assumed to capture minimal rainfall. All precipitation associated with these land cover types is allowed to reach the land surface by assigning a free throughfall coefficient (*p*) equal to 1. Wetlands intercept minimal precipitation, allowing 90% of rainfall to reach the ground surface uninhibited. Agricultural areas intercept slightly more precipitation and allow 75% of

precipitation to reach the hillslope. However, these land cover types possess minimal aerial coverage in the Upper Río Puerco tRIBS model and are believed to have little influence on the simulated watershed hydrologic response.

In contrast, approximately 98% of the Upper Río Puerco vegetation is classified as forest, shrubland, or grasslands. Within the model, forests intercept the highest proportion of rainfall (p = 0.52) followed by shrublands (p = 0.30) and grasslands (p = 0.15). Interception parameters found in *Bras* (1990) suggest that forests typically intercept a larger fraction of precipitation than grasses. Within the tRIBS setup for the Upper Río Puerco, grasslands have the highest drainage rates followed by shrubland and forest as indicated by the value of the canopy drainage exponent (g).

Parameters including Al (albedo), h (vegetation height), K_t (optical transmission coefficient), r_s (average stomatal resistance), and V (vegetation fraction) are found in calculations pertaining to the evapotranspiration and energy flux components of the tRIBS model. Surface albedo values were obtained from *Bras* (1990). Grass heights are also found in *Bras* (1990), while the remaining land cover heights are calibrated values based upon inference. Likewise, values for V (vegetative fraction) are not assigned based upon actual measurements but are instead given values considered reasonable for a semi-arid environment. K_t (optical transmission coefficient) and r_s (average stomatal resistance) are all assigned values found in the *Ivanov et al.* (2004a) tRIBS application to the Baron Fork watershed.

Table 4.5 provides soil parameter values for the calibrated Upper Río Puerco

	K_s	Θ_s	Θ_r	m	ψ_b	f	A_s	A_u	n	k_s	C_s
Sandy Loam	26.8 (20.18)[1]	0.412[1]	0.041[1]	0.378[1]	-146.6[1]	0.00520	65	140	0.453[1]	1	1000000
Loam	20.50 (10.32)[1]	0.434[1]	0.030 (0.027)[1]	0.252[1]	-112.2 (-111.5)[1]	0.00625	25	125	0.463[1]	1	1000000
Unweathered Bedrock	19.95[2]	0.085[2]	0.015	0.165	-373.3	0.00157	25	125	0.150[2]	1	1000000
Silty Loam	6.20 (6.80)[1]	0.486[1]	0.015[1]	0.234[1]	-207.9[1]	0.00650	65	140	0.501[1]	1	1000000
Clay Loam	0.45 (2.00)[1]	0.390[1]	0.077 (0.075)[1]	0.242[1]	-258.9[1]	0.00700	50	140	0.464[1]	1	1000000

Table 4.5 Soil Parameter Values for the Upper Río Puerco tRIBS Model. Superscripts equal to *1* indicate values from *Rawls et al.* (1982, 1983) while superscripts of *2* indicate parameter values from *Schwarz and Zhang* (2002).

simulations. Parameter values for soil textures with a superscript of *1* indicate values from *Rawls et al*. (1982, 1983) while a superscript of *2* indicates parameter values obtained from *Schwarz and Zhang* (2002). Where parameters were altered from the value found in the literature, the published parameter value is shown in parentheses. The conductivity decay parameter (f) and anisotropy ratio (A_s and A_u) are determined based upon goodness of fit between tRIBS simulated hydrograph and USGS streamflow data for the Upper Río Puerco. Volumetric heat conductivity (k_s) and soil heat capacity (C_s) are obtained from *Ivanov et al.* (2004a).

Following *Ivanov et al*. (2004b), K_s (saturated hydraulic conductivity), f (conductivity decay parameter), and anisotropy ratios (A_s and A_u) were the primary soil parameters used to calibrate tRIBS for the Upper Río Puerco. Generation of tRIBS streamflow magnitudes similar to those recorded by the USGS Upper Río Puerco near

Guadalupe, NM stream gauge required high values of f. Increased f forces K_s to decay rapidly with soil profile depth and raises the likelihood that tRIBS will generate Hortonian runoff (the reader can refer to section 2.5.2 for governing equations). High values of f also minimize model sensitivity to A_s, since the anisotropy ratio appears in equations dealing with lateral redistribution of soil moisture following saturated layer development in the soil profile.

Figure 4.15 demonstrates saturated conductivity decay with increasing soil depth for each soil texture in Table 4.5. All soils except for unweathered bedrock decay to K_s of ~ 0 mm/hr within the first 2 m of the soil column. While bedrock conductivity decays over ~ 5 m, low bedrock porosity values create a rapidly saturating layer so f is not a critical parameter for runoff generation associated with unweathered bedrock soil type.

The final set of parameter values requiring calibration are those controlling hillslope runoff routing and in-channel streamflow routing. The hillslope velocity coefficient (c_v) and hillslope velocity exponent (r) correspond to the parameterization used in the Baron Fork, OK, tRIBS simulations (*Ivanov et al.,* 2004b). These parameters result in typical hillslope runoff velocities of ~ 0.05 - 0.8 m/sec (Figure 4.14b). Manning's η, found in equation 2.33, was assigned a value of 0.065. This parameter value is considered slightly high for arroyo stream networks such as the Upper Río Puerco.

Large values of channel roughness may compensate for channel slope estimation error in the numerator of Manning's equation. DEM vertical resolution of 7 m - 15 m and

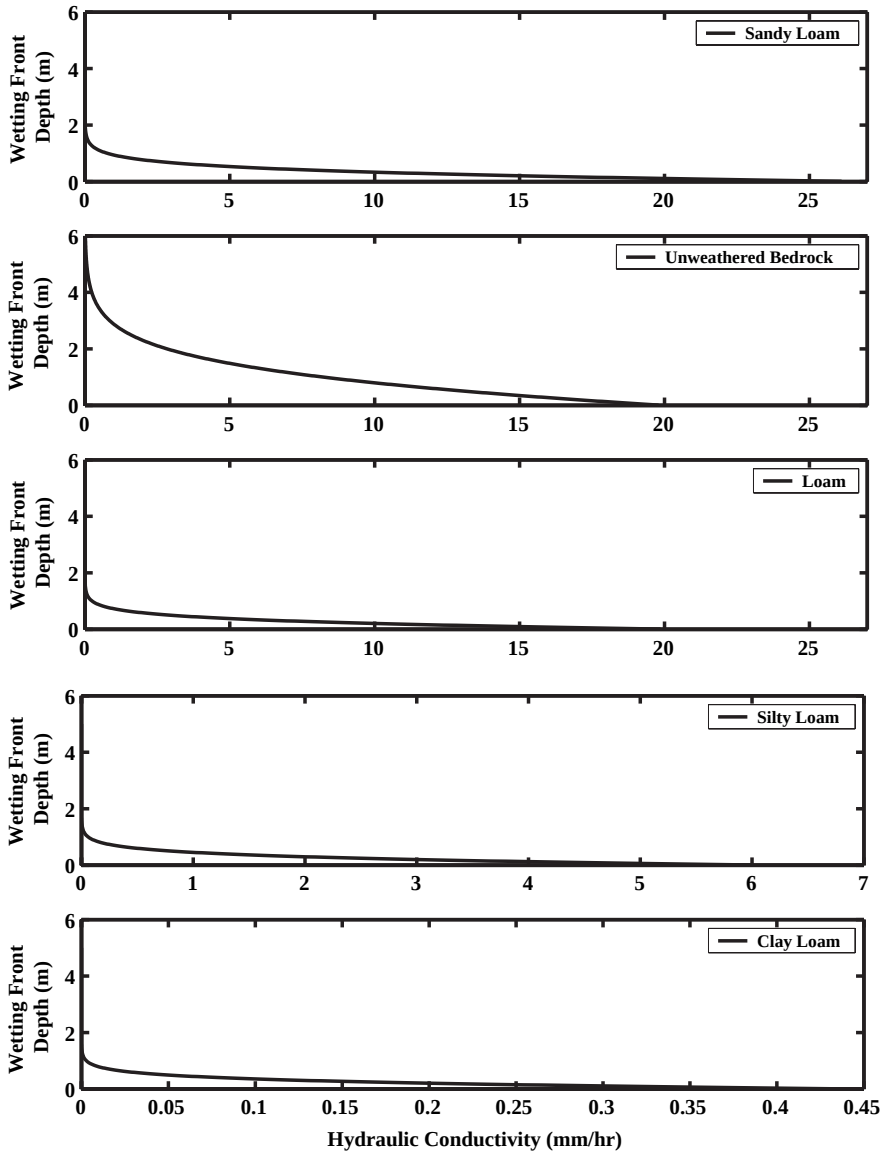

Figure 4.15 Conductivity Decay With Increasing Wetting Front Depth. Wetting Front Depth is a Proxy For Depth Into the Soil Profile.

resampling of the DEM during TIN generation could lead to large slope values between channel nodes. When higher slope values are used in Manning's equation they lead to increased discharge magnitudes. Overestimation of Manning's η may serve to lower discharge magnitudes to more reasonable values and introduce model compensation for incorrect channel slopes. Manning's η values derived from field studies in the Río

Puerco and Río Salado near Socorro, NM are discussed in Chapter 5.

Once the tRIBS model was calibrated, the initial water table depth for all subsequent model runs was determined through a drainage experiment. The model water table was set at the surface and allowed to drain for 90,000 hours. Low hydrologic decay parameters across a large portion of the watershed prevented the water table from dropping below ~ 2 m in most locations. As a result, the water table was lowered an additional 5 m to achieve a more reasonable water table depth for a semi-arid environment.

4.8.3 tRIBS Model Results and Discussion for the Upper Río Puerco

Model simulations correspond to the time period of June 1, 2003 to October 14, 2003. These dates coincide with the core of the monsoon season in New Mexico (*Douglas et al.*, 1993). Model results are shown for the entire summer of 2003 as well as the first two weeks of September 2003 in Figure 4.16. While important differences exist, the tRIBS model simulation for the monsoon season 2003 reproduces the major features of the sequence of flood events observed in the Upper Río Puerco. However tRIBS does not consistently produce accurate estimates of streamflow timing, magnitude, or hydrograph shape during the simulation period.

For example, a minor flood event recorded by the USGS gauge on August 12, 2003 is generated by tRIBS, however the modelled event occurs ~ 70 hrs later than the USGS observation (Figure 4.16a). In addition, the modelled hydrograph recession limb gradually approaches zero, while the USGS observed discharge values rapidly subside

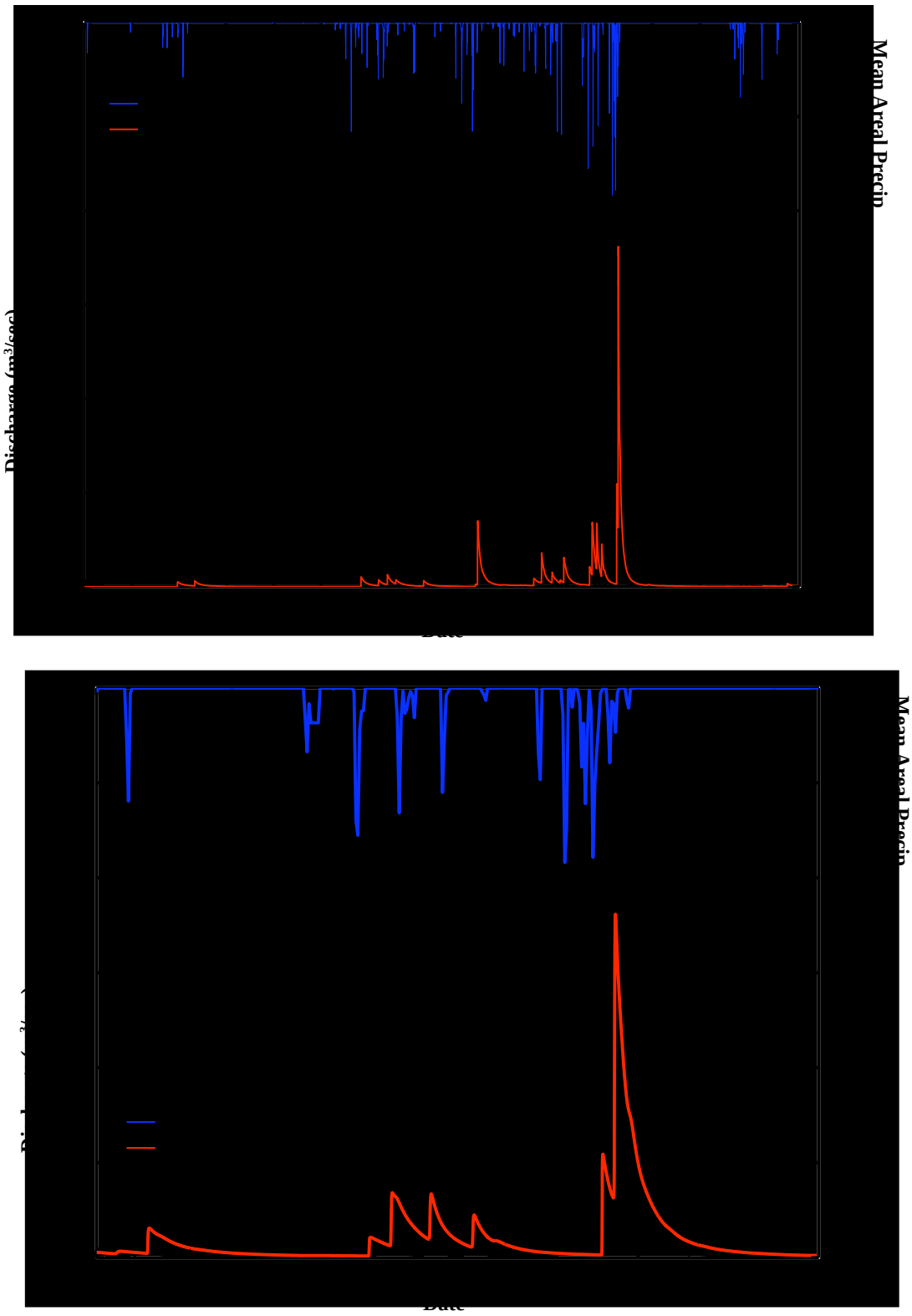

Figure 4.16 Upper Río Puerco tRIBS Model Results a) Summer 2003 b) Early September 2003.

following the hydrograph peak. Simulated streamflow peak magnitude for this particular event is comparable to the USGS stream gauge data.

The three streamflow events from September 5 through September 8 are also inaccurately reproduced by the tRIBS calibrated model (Figure 4.16b). The first of these tRIBS modelled streamflow events corresponds to model hour 2317 in Figure 4.16b. This particular simulated discharge peak underestimates the corresponding USGS recorded maximum by 20.2 m^3/sec (54 %). Furthermore, the tRIBS hydrograph peak lags the gauge data maximum by 3 hours. Streamflow magnitude estimation for the flood at tRIBS hour 2338 improved however, the tRIBS hydrograph peak occurs 3.5 hours later than the USGS recorded flood event. In this case, tRIBS underestimates peak discharge by merely 2.77 m^3/sec (14.2 %). The final flood within this three event cluster is produced by tRIBS at model hour 2360. Again, tRIBS underestimates peak discharge. For this flood, peak discharge is underestimated by 9.4 m^3/sec (45.5 %). The lag time between the USGS flood maximum and the tRIBS peak discharge increased to 4.5 hours. Recession limbs for all three of these events are exceedingly long whereas USGS discharge data shows a steep hydrograph recession. Additionally, each one of the September 5 - September 8 tRIBS simulated events occurs between 16 - 18 hours after rainfall events recorded by NEXRAD radar (Figure 4.16b). Despite time lags between the observed and simulated streamflow hydrographs, the difference is small compared to time required for flood peaks to reach the watershed outlet following high-intensity convective rainfall events (Figure 4.16).

For the major streamflow event of September 11 2003, the USGS stream gauge

records a series of smaller flood events before the arrival of the large flood pulse. tRIBS does not reproduce these events. However, tRIBS adequately captures the timing of the rising limb for the major flood event. Unlike underestimation of peak streamflow observed in earlier events, tRIBS overestimates peak discharge for the large flood event by 40.8 m^3/sec (45.1 %). In this case, the overestimation of the discharge peak is accommodated by the gradual recession curve so that runoff volumes under the main flood pulse are similar for the simulated and observed hydrographs. Integrating under the tRIBS model hydrograph and the USGS hydrograph from September 10 through September 16 yields total flow volumes of 4.2 x 10^6 m^3 and 3.9 x 10^6 m^3 respectively. Hence, tRIBS overestimates streamflow volumes for this event by 7.1 %.

The wide variety of temporally and spatially distributed output datasets from the tRIBS model provide an opportunity to investigate why simulations are limited in their ability to reproduce observed streamflow in a large semi-arid watershed. For example, the runoff hydrograph shows the runoff generation mechanisms used in tRIBS for the Upper Río Puerco model (Figure 4.17). Infiltration excess is the only significant runoff type generated by tRIBS for the entire simulation period. Low saturated hydraulic conductivity or high conductivity decay parameter values increases the likelihood of runoff generation via infiltration excess. Both these conditions are found in the calibrated soil values used for the Upper Río Puerco simulation. Other distributed models developed for semi-arid environments including KINEROS and CASC2D use only an infiltration excess runoff generation scheme (*Michaud et al.*, 1994; *Downer et al.*, 2002). Consequently, tRIBS parameter values that lead to infiltration excess runoff is not an

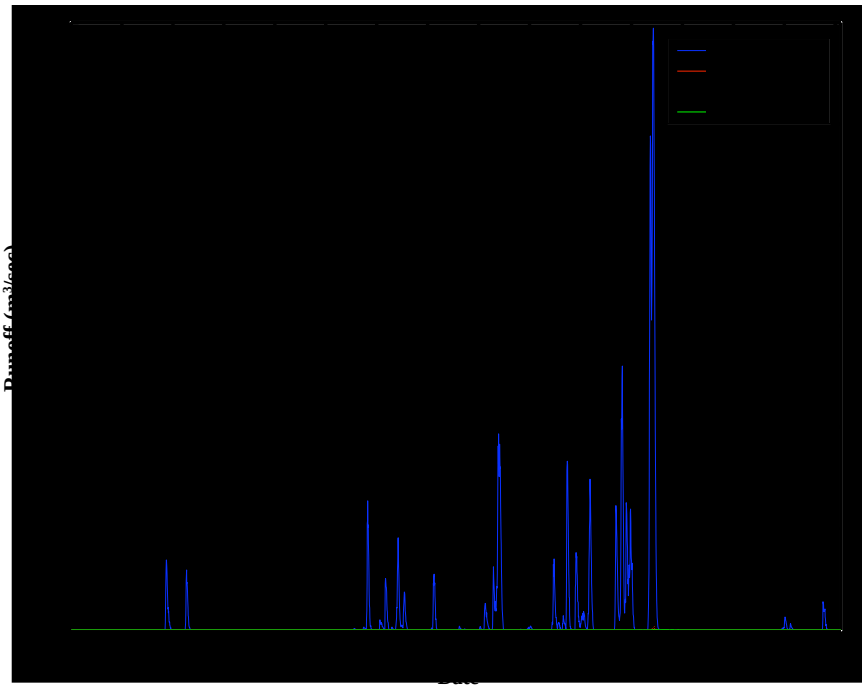

Figure 4.17 Upper Río Puerco tRIBS Model Runoff Mechanisms for the Summer 2003 Simulation Period. Runoff mechanisms other than infiltration excess runoff plot either zero values or negligible magnitudes. Runoff discharge is determined at the watershed outlet but calculations are not performed using the kinematic wave equation routing methodology. Instead, runoff types are routed using the distance to the channel outlet with uniform channel velocity.

unreasonable outcome for a semi-arid watershed.

The runoff mechanism hydrograph reveals that the extended hydrograph tails observed in Figure 4.16 are not due to slower runoff generation mechanisms such as perched subsurface stormflow, ground water exfiltration, or saturation excess processes. This suggests the lengthy recession curves observed in the simulation hydrographs are due to either delayed runoff generation or to runoff that is not efficiently routed from the point of production to the watershed outlet.

Figure 4.18 maps streamflow velocities at model hour 2439 during the largest September 2003 discharge peak in the tRIBS hydrograph. Main channel velocities are

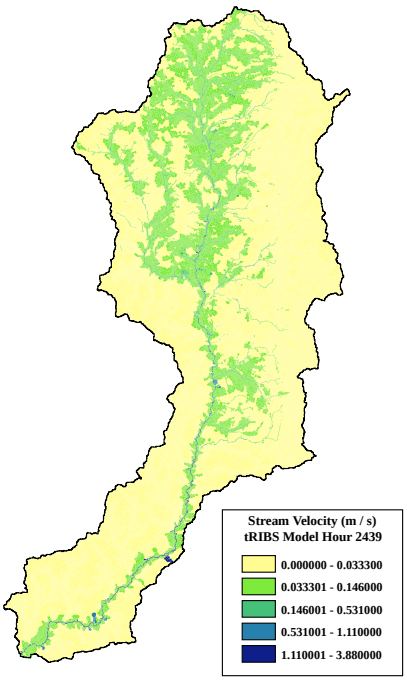

Figure 4.18 Upper Río Puerco Stream Flow Velocities at Hour 2439

considered reasonable to slightly high. For example, *Vivoni et al.* (2005) estimated that the September 11 flood pulse travelled at a velocity of 0.7 m/s between the Río Puerco near Guadalupe, NM and the Río Puerco near Bernardo, NM USGS stream gauges. However, lower flood wave velocities based upon USGS streamflow measurements may be a result of decrease in channel slope or higher infiltration losses within this stretch of the Río Puerco south of Guadalupe, NM.

Within the tRIBS Upper Río Puerco simulation, once hillslope runoff reaches a channel node, water is routed relatively quickly through the channel network to the watershed outlet. In addition, the distribution of hillslope velocities as a function of contributing area and discharge shown in Figure 4.14b appear reasonable. Consequently, it is unlikely that the long recession curves in the tRIBS model are due to unreasonably

slow hillslope or channel travel velocities. This does not remove the possibility that some hillslope lengths in the model may be overestimated. Even if hillslope velocities are reasonable, long travel paths to the nearest channel node could result in the extended hydrograph recession curves observed in Figure 4.16.

tRIBS also allows the placement of interior hydrograph nodes that record discharge at points along the channel network. Interior nodes can expedite calibration efforts by isolating regions within a watershed that contribute to large flood production following initial tRIBS calibration. Efforts to further improve tRIBS model results can then focus on soil and land cover parameters corresponding to regions of elevated runoff production.

In Figure 4.19, thrity-one interior nodes are positioned within four major Upper Río Puerco subbasins and the lower segment of the Upper Río Puerco main stem. Subwatersheds include: (1) Arroyo Chijuillita; (2) Señorito, San Pablo, and San Miguel Canyons; (3) Arroyo San Jose; (4) and the Río Puerco[1]. Interior nodes are placed over a wide range of contributing areas shown in Figure 4.19b including the outlet of each one of the Upper Río Puerco subwatersheds.

Figure 4.20a provides the cumulative volumes for each interior node over the entire tRIBS simulation period. Modelled volumetric totals from the Arroyo San Jose outlet (node #21) indicate a large proportion of streamflow volume totals recorded at the Upper Río Puerco outlet emanate from within the Arroyo San Jose subbasin for these

[1]The Río Puerco headwater basin is the true continuation of the main stem from Bernardo, NM to its headwaters in the Sierra Nacimiento.

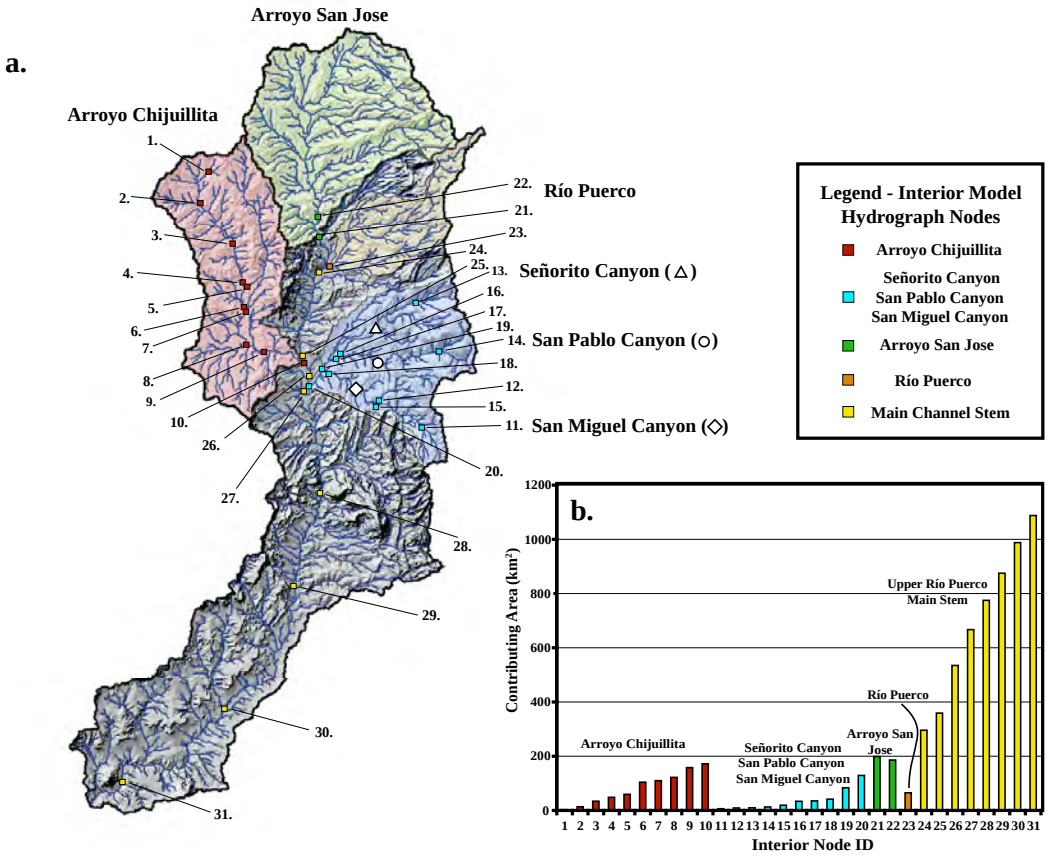

Figure 4.19 a) Upper Río Puerco tRIBS Interior Nodes b) Interior Node Contributing Area

monsoon events. Total runoff volumes recorded for the entire Arroyo Chijuillita are provided by node #10. For these storm events, runoff production within this area of the Upper Río Puerco produces moderate streamflow events but fails to generate streamflow discharge comparable to the Arroyo San Jose. Discharge volumes simulated at the outlet of the Señorito, San Pablo, and San Miguel Canyons (referred to henceforth as the Canyons) are slightly less than volumes produced by the Arroyo Chijuillita. The Río Puerco headwater basin generates the least amount of streamflow over the summer of 2003 according to the tRIBS simulation.

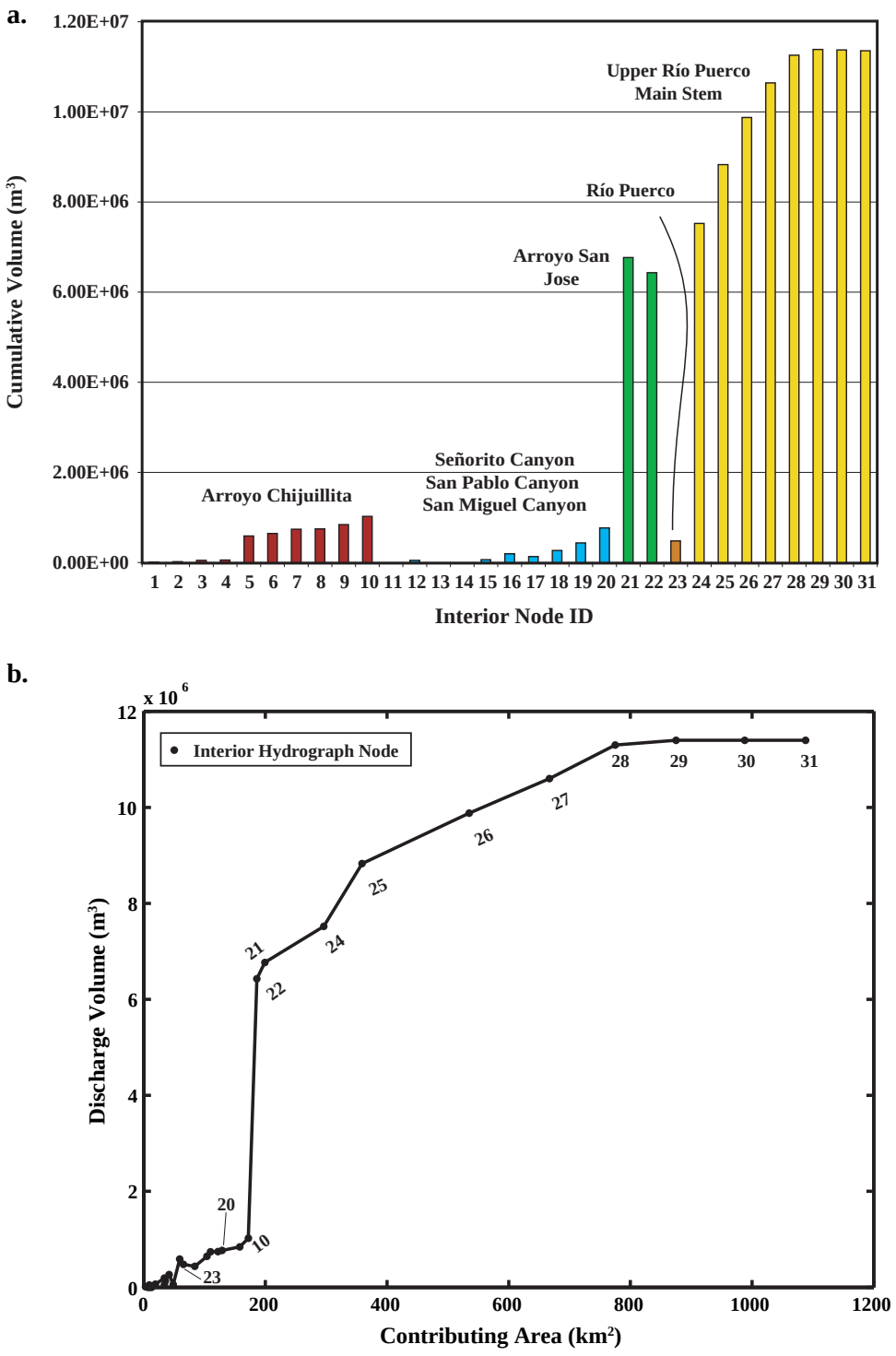

Figure 4.20 a) Upper Río Puerco Interior Node Cumulative Volumes for the Summer 2003 tRIBS Simulations b) Discharge Volume as a Function of Contributing Area for Interior Nodes

Figure 4.20b demonstrates increasing cumulative discharge as a function of contributing area. At low contributing areas, total streamflow volumes fluctuate due to the non-uniform spatial distribution of rainfall. As watershed upstream contributing area increases, total streamflow volumes also increase due to the inclusion of additional rainfall-runoff from other portions of the watershed. The large rise in total discharge volumes at 199 km^2 is due to flood generation in the Arroyo San Jose. In addition, node #28 corresponds to contributing area value of 775 km^2. Locations along the main channel for nodes #28 through #31 demonstrate little increase in streamflow volume. This suggests a potential lack of tributary discharge contributions within this stretch of the Upper Río Puerco stream network for the summer 2003. However, this finding is not conclusive since it is based upon a calibration that only provides a fair reproduction of the USGS observed hydrograph at the watershed outlet.

While streamflow volumes indicate the location of runoff production, hydrographs for interior nodes can provide information regarding the source of flood generation for each respective flood event. Based upon stream volume totals in Figure 4.20, hydrographs were produced for five interior watershed nodes. Figure 4.21 shows hydrographs from the eastern fork of the Arroyo Chijuillita (Node #5), the Arroyo Chijuillita Outlet (Node #10), the Canyons Outlet (Node #20), the Río Puerco Headwater Outlet (Node # 23), and the Arroyo San Jose Outlet (Node #21). Note that in Figure 4.21 subplots *a* through *d* use the same *y* axis however, elevated discharge values from the Arroyo San Jose forced an alternative *y* axis in subplot *e*.

Figure 4.21e reveals that the September 11 flood event was primarily generated

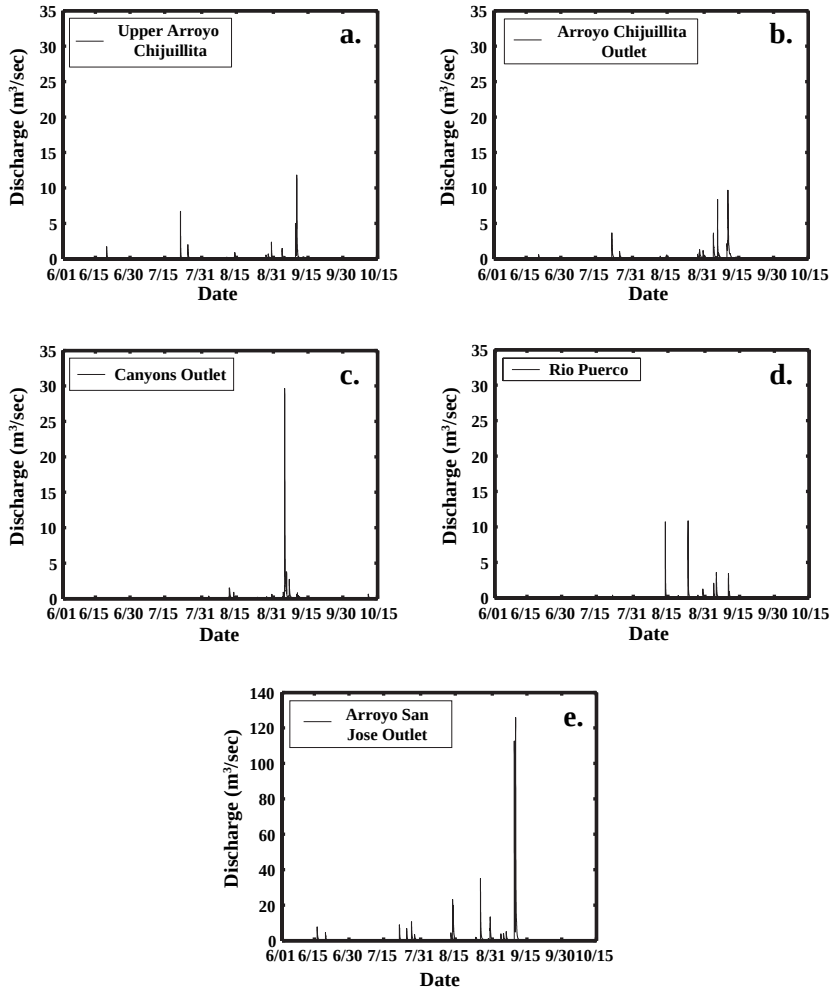

Figure 4.21 Upper Río Puerco Interior Node Hydrographs for the Summer 2003 tRIBS simulations

within the Arroyo San Jose subwatershed. Smaller streamflow contributions for this particular event are also produced from the Arroyo Chijuillita Watershed and the headwaters of the Río Puerco (Figure 4.21b and Figure 4..21d). The Canyons Outlet shows one large flood event that appears to occur earlier than the main pulse generated in the Arroyo San Jose basin (Figure 4.21c).

Figure 4.22 plots the same interior node hydrographs over the first two weeks in September. Of the five subbasins analyzed, the Canyons watershed is the main producer

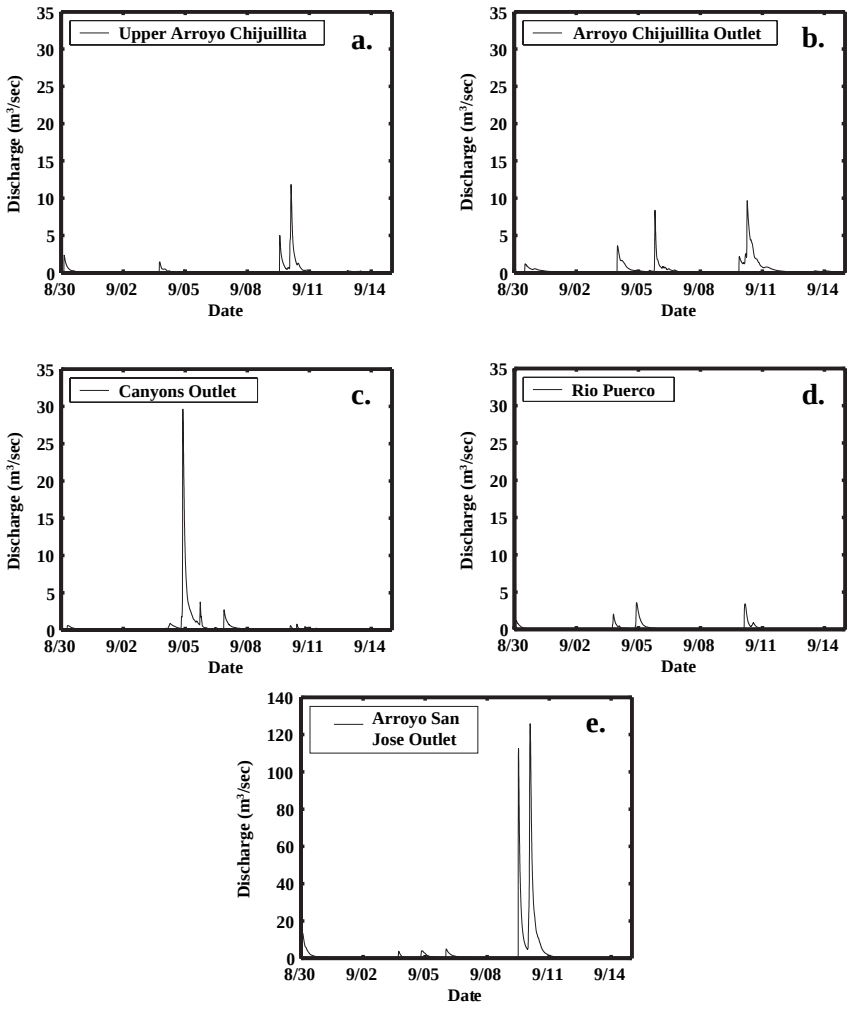

Figure 4.22 Upper Río Puerco Interior Node Hydrograph for Early September 2003 tRIBS Simulations

of streamflow that resulted in the three smaller discharge events between September 5 and September 8 2003. The Canyons Outlet did not contribute streamflow during the September 11 2003 flood event. Based upon watershed contributions to floods observed at the Upper Río Puerco outlet, investigation into soil parameterization within the Canyons and Arroyo San Jose subwatersheds can lead to additional understanding of tRIBS hydrograph reproduction for the summer of 2003.

Reexamination of the soils map in Figure 4.5 with particular attention paid to the

location of the Arroyo San Jose and the Canyons subwatershed reveals that each basin contains the same soil textures: (1) Loam; (2) Sandy Loam; and (3) Clay Loam. Calculations performed in ArcMAP show that the Arroyo San Jose spans 198.5 km^2 where 136.7 km^2 is classified as clay loam (68.9 %), 43.1 km^2 is classified as loam (21.7 %), and 18.7 km^2 is classified as sandy loam (9.42 %). The Canyons watershed covers 128.8 km^2 of the Upper Río Puerco where 54.6 km^2 is classified as clay loam (42.4 %), 51.2 km^2 is classified as loam (39.8 %), and 23.0 km^2 is classified as sandy loam (17.8 %).

Because each basin contains identical soil textures, tRIBS model performance cannot be substantially improved by calibrating soil types unique to each subwatershed unless each soil texture class is treated independently depending on its location in the Upper Río Puerco watershed. In addition, similar soil texture percent coverage of each subbasin suggests that if soil calibration concentrates on improving model performance within the the Canyons, changes in parameter values will also have similar implications for the Arroyo San Jose and vice-versa. As an example, assigning parameter values that impose less permeable soils within the Canyons watershed would force earlier runoff production and higher runoff magnitudes. This could potentially improve tRIBS representation of the September 5 - September 8 flood event. However, these changes could have the same effect for the September 11 event and lead to a worse model calibration.

Table 4.5 also shows loam and sandy loam are relatively permeable while clay loam is not. Thus, the clay loam parameter values produce quick runoff response to

rainfall forcing. Streamflow associated with rising hydrograph limbs is likely produced by clay loam soil textures. However, sandy loam and loam soil textures have higher saturated conductivity. Although the conductivity decay parameter causes a rapid decrease in conductivity with depth, both these soil textures possess soil moisture storage capacity. Thus, for storms with precipitation intensities less than 20.5 mm/hr (Loam K_s) but greater than 0.45 mm/hr (Clay Loam K_s), the clay loam generates runoff while loam and sandy loam fills available pore space until the vertical redistribution of soil moisture is less than the rainfall rate. Late runoff generation due to the filling of loam and sandy loam pore spaces could partially explain the longer tails observed in the tRIBS hydrograph recession limbs.

To investigate whether decreased permeability of loam and sandy loam soil texture corrects event timing, improves peak discharge estimates, and reduces hydrograph recession periods, an additional model simulation was performed for the soil parameterization shown in Table 4.6. Sandy loam and loam K_s values were reduced and f values were increased to minimize soil permeability within the Upper Río Puerco tRIBS model (shown in bold font). The previous conductivity decay rate and the new parameterized decay rate are shown in Figure 4.23 Sandy loam and loam conductivities still decay to ~ 0 mm/hr within the top 2 m of the soil profile however, the starting point of conductivity decay is substantially reduced.

tRIBS model results are shown in Figure 4.24. Peak flow magnitudes and timing of initial hydrograph peaks are substantially improved over the previous model simulation especially for the September 5 through September 8 events. However, the

	K_s	Θ_s	Θ_r	m	ψ_b	f	A_s	A_u	n	k_s	C_s
Sandy Loam	**4.80** (20.18)[1]	0.412[1]	0.041[1]	0.378[1]	-146.6[1]	**0.00875**	65	140	0.453[1]	1	1000000
Loam	**2.50** (10.32)[1]	0.434[1]	0.030 (0.027)[1]	0.252[1]	-112.2 (-111.5)[1]	**0.00900**	25	125	0.463[1]	1	1000000
Unweathered Bedrock	19.95[2]	0.085[2]	0.015	0.165	-373.3	0.00157	25	125	0.150[2]	1	1000000
Silty Loam	6.20 (6.80)[1]	0.486[1]	0.015[1]	0.234[1]	-207.9[1]	0.00650	65	140	0.501[1]	1	1000000
Clay Loam	0.45 (2.00)[1]	0.390[1]	0.077 (0.075)[1]	0.242[1]	-258.9[1]	0.00700	50	140	0.464[1]	1	1000000

Table 4.6 Adjusted Soil Parameter Values for the Upper Río Puerco tRIBS Model. Superscripts equal to *1* indicate values from *Rawls et al.* (1982, 1983) while superscripts of *2* indicate parameter values from *Schwarz and Zhang* (2002).

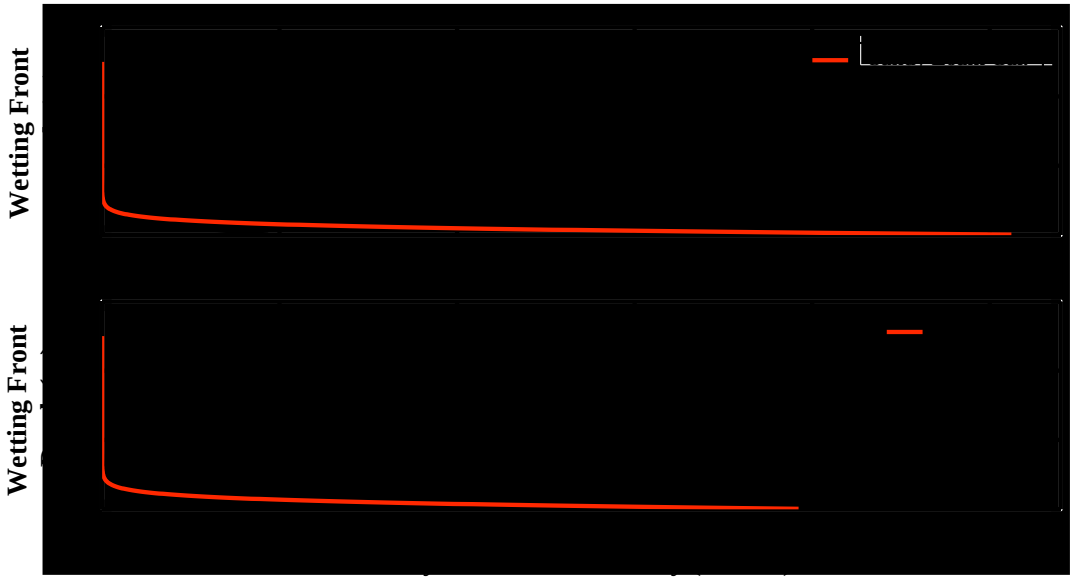

Figure 4.23 Conductivity Decay With Depth for New Loam and Sandy Loam Parameterization shown in Table 4.6

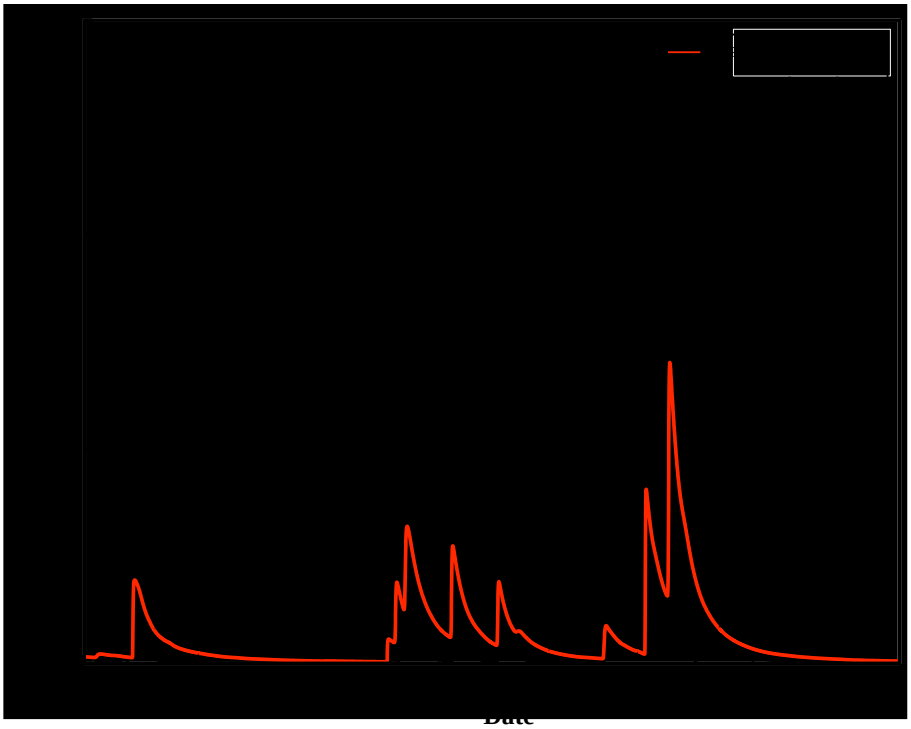

Figure 4.24 Summer 2003 Upper Río Puerco Simulation for Loam and Sandy Loam with Reduced Permeability

extended recession limbs still impose a large overestimation of streamflow volumes for this event. The change in soil parameter values also altered the peak hydrograph on September 11. The redistribution of runoff volumes reduced the tRIBS model September 11 peak magnitude compared to the previous calibrated simulation. Timing of the main flood event remained the same as the previous simulation. However, flood volumes are shifted to earlier time periods, which causes a large event preceding the September 11 discharge peak that is not observed in the USGS stream gauge record. Reducing loam and sandy loam permeability did not improve the extended hydrograph tails observed in the tRIBS model hydrographs.

Despite possible improvements from reducing rainfall infiltration into the soil column, the new parameter values introduce questions of whether the parameter values

are realistic. The parameterization used in Table 4.6 creates clay loam, loam, and sandy loam soil textures that introduce a relatively impervious land surface over most of the Upper Río Puerco. Without investigation into wetting front depth for different soil textures found within the watershed, acceptable values for *f* remain unknown.

Reduction of land surface permeability in the tRIBS model may account for problems introduced by the hourly-interval NEXRAD data product. Previous work performed by *Assouline et al.* (2007) demonstrated temporal averaging of precipitation at the hourly scale results in an underestimation of time to ponding. Similar to *Assouline et al*. (2007), NEXRAD data used for the Upper Río Puerco occurs at hourly intervals suggesting that runoff timing may be misrepresented due to NEXRAD temporal resolution. Consider that a storm with 25 mm/hr intensity for twelve minutes will appear as an hourly rainstorm at 5 mm/hr in the NEXRAD radar dataset. If infiltration excess runoff is produced by an intense storm in the Upper Río Puerco with durations shorter than one hour, tRIBS soil hydraulic conductivities need to be lower than actual watershed values to generate runoff observed in the stream gauge hydrograph. Furthermore, rainfall that actually occurs on the sub-hourly scale may result in flood events of short duration. Averaging precipitation intensity to the hourly scale may require impervious soils to match the hydrograph magnitudes but lead to modelled streamflow durations that are longer than observed flood events. Note also that spatial averaging of storm events with areal coverage less than NEXRAD pixel scale can lead to similar attenuation of rainfall intensities.

Although applying parameters that render the soil layer relatively impervious to

rainfall improves tRIBS hydrograph timing and magnitudes, reducing soil permeability also removes any possibility of modelled subsurface flow. *Beven* (2002) suggests that subsurface flow in semi-arid environments may be an important runoff generation mechanism that hydrologic models often ignore. Furthermore, *Wilcox et al*. (1997) demonstrated that subsurface storm flow may result from development of a perched water table following wet periods for a small hillslope near Los Alamos, NM. Consequently, if soil moisture accumulated over the duration of the monsoon season and resulted in subsurface perched flow contributions during the September 11 event, tRIBS parameterization would not represent this runoff mechanism due to the impervious nature of the soil profile.

In addition to limiting model hydrologic representation, impervious soil representation also maximizes runoff volume production. This may lead to overestimation of runoff volumes as observed in Figure 4.24. Currently, any runoff generated on the hillslope within tRIBS must be routed to the channel outlet so volumetric losses from the time of runoff production to the time of exit from the watershed is not possible. Losses due to reinfiltration into the soil column downslope from the point of runoff generation (runon) and streambed losses are considered important processes in semi-arid watershed hydrology (*Beven*, 2002) and their absence in the tRIBS model physics may result in difficulties calibrating the model for semi-arid watersheds.

For example, flood wave attenuation and streamflow losses in the Upper Río Puerco are likely based upon watershed geometry alone. Consider that 78% (874 km^2) of

the watershed's contributing area lies above node # 29 in Figure 4.19. Downstream of this node, the channel has little potential for additional streamflow contributions from major subwatersheds. In fact, the Upper Río Puerco flows over 12 miles from node #29 to the watershed outlet. Lack of major tributary inflows, evaporative losses, and streamflow loss through the channel bed are all conceivable processes within this reach of the network. If streamflow losses are an important component of the rainfall - runoff process, accommodation within other portions of the tRIBS model, such as increasing soil permeability, is unlikely to reliably compensate for delays in peak flow or flood wave attenuation.

For a basin of the size and complexity of the Upper Río Puerco, naming a single calibration as better or worse than another based upon hydrograph fit alone is a dangerous proposition. The number of degrees of freedom involved with a model containing over 100,000 nodes and the absence of physical data that could constrain model parameters can lead to multiple independent model representations that reproduce adequate hydrographs for a given flood event. A distributed model application for a watershed where parameter values possesses large uncertainties such as the Upper Río Puerco, presents a modeller with the means to reproduce an observed hydrograph while incorrectly portraying basin physics. If internal watershed processes are not correctly represented due to unrealistic parameter values, conclusions based upon the model may be incorrect despite achieving a suitable reproduction of a particular flood event.

Furthermore, problems are not limited to parameter uncertainty which pertains only to the physical representations currently incorporated within the distributed model.

Model error may also exist with respect to the omission of observed hydrologic process specific to a particular watershed. In the context of tRIBS, the model currently lacks representation of potentially important semi-arid watershed processes such as overbank flow, stream bed infiltration loss, and runon.

Consequently, simulations performed in Chapter 5 should be viewed primarily in the context of a tRIBS model sensitivity study that uses a conceptual model of arroyo development to guide further tRIBS applications. Additional model simulations utilize the Upper Río Puerco parameterization with higher loam and sandy loam permeability found in Table 4.5. Despite problems with model calibration and process representation, certain modelling scenarios provide insight into streamflow response to arroyo development. Other simulations reveal different degrees of sensitivity to changes in channel network representation and conclusions with respect to arroyo development should be made with caution. These issues are discussed further in Chapter 5.

CHAPTER 5 - MODEL SENSITIVITY AND ARROYO DEVELOPMENT SCENARIOS

5.1. Introduction

Since tRIBS is a distributed model that explicitly represents each stream segment within the entire drainage network, model sensitivity to network length, channel width, and Manning's roughness coefficient may provide insights into streamflow changes occurring in response to different stages within a conceptual model of arroyo development. As discussed in Chapter 3, two major components of arroyo geormorphological change are adjustments in channel width and channel length. tRIBS is able to represent hypothetical stages of arroyo incision and recovery by utilizing different combinations of channel network lengths and channel width geomorphic power laws. In addition, variations in channel roughness due to changes in channel geometry or the establishment of riparian vegetation on the floodplain can be approximated through alteration of Manning's roughness coefficient. Before investigating model response to different channel network representations within the Upper Río Puerco watershed, sensitivity experiments were conducted for a small synthetic test basin. Beginning with a simplified example minimizes land use and soil type variability and their influence on runoff production and timing.

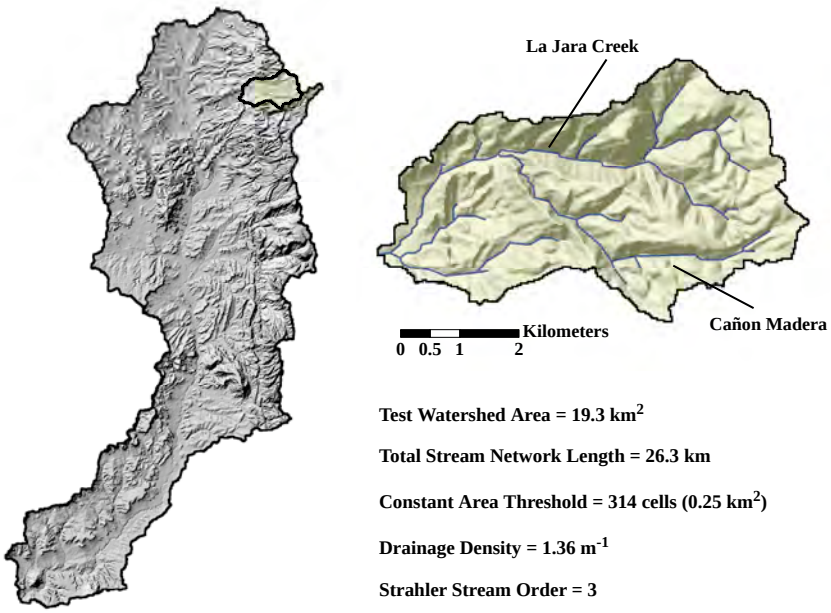

Figure 5.1 Test Watershed Location

5.2 Test Basin Experimental Design: Constant Width Relationship

The test basin is a small 19.3 km^2 watershed delineated from the northeastern corner of the Upper Río Puerco watershed within the Arroyo San José (Figure 5.1). The two main tributaries in the test watershed are La Jara Creek and Cañon Madera. La Jara Creek is the larger of the two networks and drains the Sierra Nacimiento mountain front in a southwest direction until it reaches the Upper Río Puerco near Cuba, NM. Within the calibrated Upper Río Puerco tRIBS model, reclassified soil types for La Jara Creek and Cañon Madera included loam, clay loam, and sandy loam. Reclassified land use types included forest with additional minor areas of grassland and shrubland.

Although accurate representation of land surface properties was important for model calibration, the synthetic model experiments apply a simplified condition of clay loam soil texture and forest land cover to the test basin. Parameter values assigned to soil

and land use grids correspond to the values determined in the Upper Río Puerco calibration exercise. Likewise, both the initial water table depth and the depth to bedrock use the same input files as the calibrated Upper Río Puerco model. For each synthetic model run, tRIBS resamples the initial water table and bedrock grids to the test watershed boundary.

The first synthetic model simulation used NEXRAD rainfall data. However, radar forcing failed to generate streamflow in the La Jara Creek/Cañon Madera subbasin. This was not completely unexpected since September 2003 NEXRAD rainfall estimates in this area of the watershed are low relative to other portions of the Upper Río Puerco (see section 4.6). As an alternative, each test watershed simulation was forced with hourly rain gauge data from the NCDC station at Cuba, NM. The rainfall time series begins on June 1, 2003 and ends October 14, 2003 (Figure 5.2). In addition, the meteorological data gathered from various New Mexico NCDC stations used in the Upper Río Puerco was also used for the La Jara Creek/Cañon Madera test basin model runs.

Seven TINs with different test basin drainage densities were generated to investigate streamflow response to network variation associated with arroyo incision. The initial TIN stream network uses the constant area threshold (314 DEM cells; 0.25 km^2) determined from orthophotograph sampling locations throughout the Upper Río Puerco. Additionally, the portion of the floodplain coverage created for Upper Río Puerco that coincides with the test watershed area was imbedded into the La Jara Creek/ Cañon Madera TIN. In this TIN representation, La Jara Creek forms a third order stream network based upon the Strahler method of classification. Total length of all stream

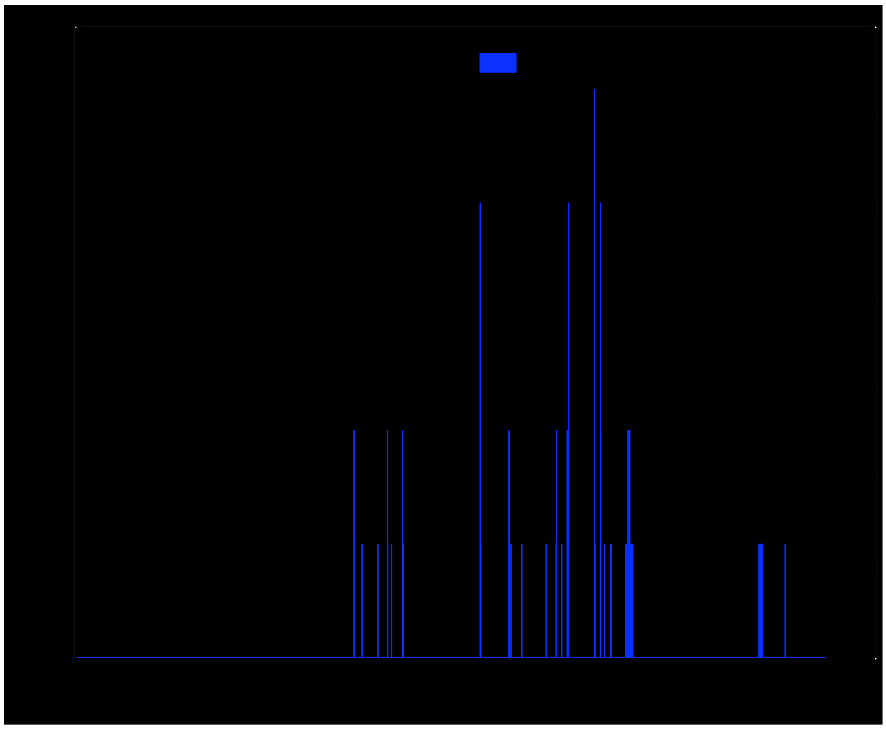

Figure 5.2 Hyetograph NCDC Raingauge Cuba, NM 6/1/03 - 10/14/03. The rainfall time series is used to force test basin simulations.

network links (ΣL) is 26.3 km. Dividing ΣL by the basin area produces a drainage density of 1.36 km^{-1}.

The six other TINs generated for the La Jara Creek/Cañon Madera watershed utilize higher constant area threshold values for stream network delineation. As a result, the total length of the stream network gradually decreases across different TINs. In Figure 5.3, drainage networks are labeled using the percentage of total stream length removed from the orthophotgraph-based network (shown in blue). However, it is more convenient to identify each test watershed TIN by its ΣL value. This method is used for the remainder of the study. The ΣL that corresponds to each new drainage network is provided in Figure 5.3.

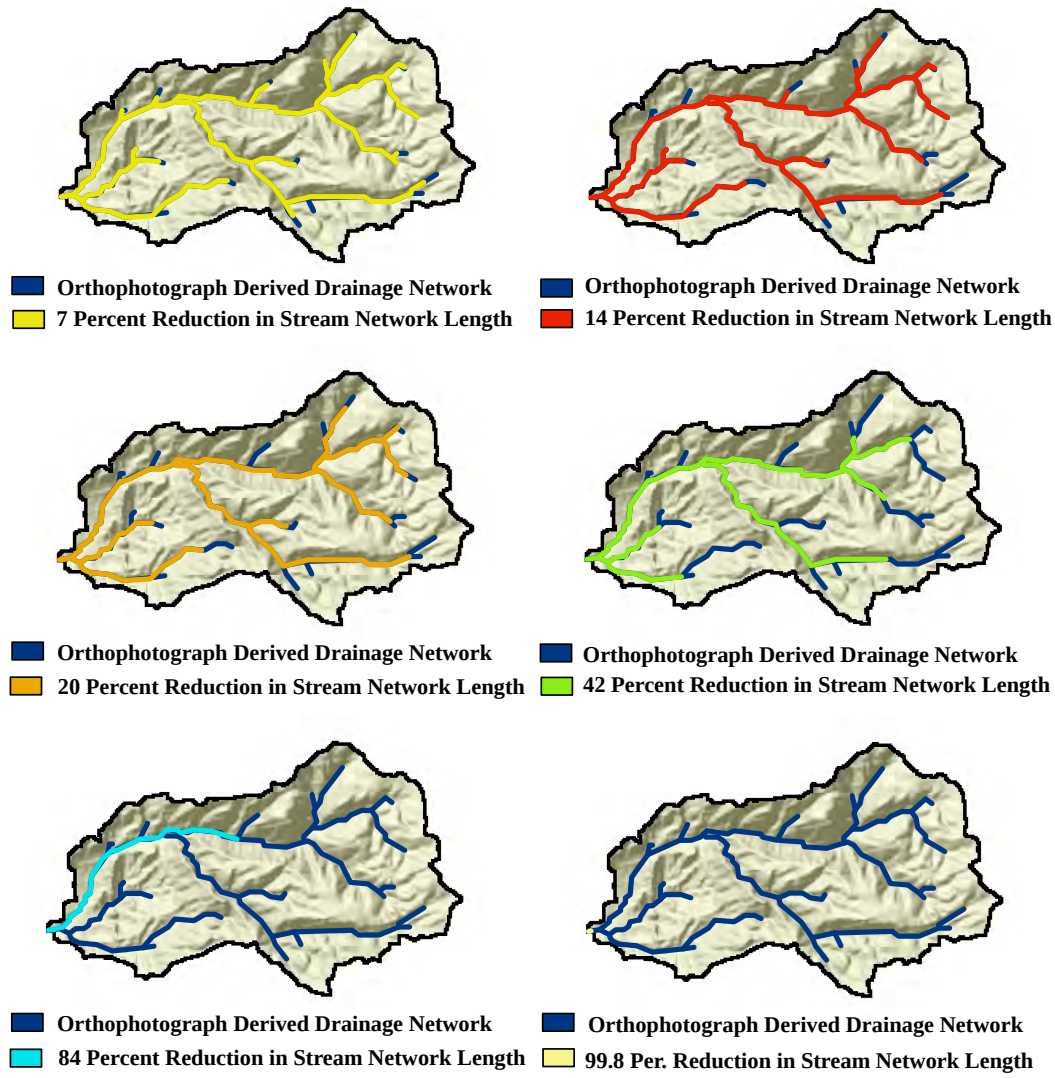

Figure 5.3 Different test watershed drainage network representations.

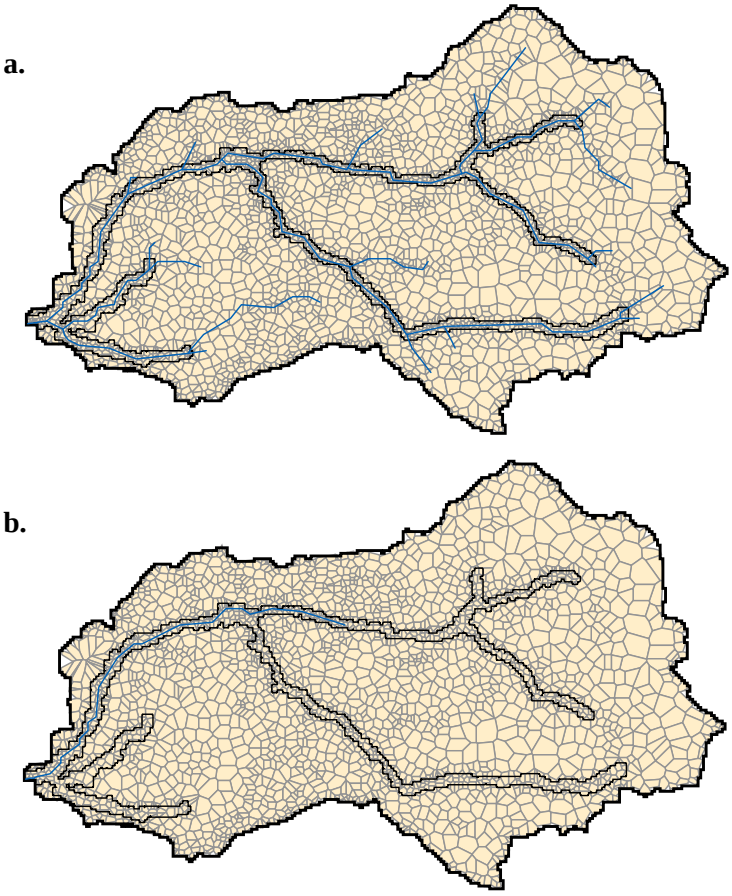

Figure 5.4 High resolution floodplain across different drainage network representations. a) Voronoi mesh with ΣL = 26.3 km b) Voronoi mesh ΣL = 15.4 km. Despite the different drainage network densities the high resolution floodplain remains identical.

All test watershed TINs maintain a Z_r resolution of 10 m and utilize the same floodplain coverage to preserve high terrain resolution over the identical portion of the watershed. Figure 5.4 shows the Voronoi mesh created by tRIBS for two different ΣL values of 26.3 km and 15.4 km respectively. The Voronoi mesh with ΣL equal to 15.4 km preserves the entire high resolution floodplain even though the channel network does not extend throughout the watershed. Including the entire floodplain ensures topographic representation is consistent across all the TINs. Consequently, the test watershed's total network length is the only significant variation between the TINs.

Simulation Number	**ΣL 26.3 km**	**ΣL 24.4 km**	**ΣL 22.8 km**	**ΣL 21.0 km**	**ΣL 15.4 km**	**ΣL 4.34 km**	**ΣL 0.04 km**
η = 0.0625	***1.***	***2.***	***3.***	***4.***	***5.***	***6.***	***7.***
η = 0.045	***8.***	***9.***	***10.***	***11.***	***12.***	***13.***	***14.***
η= 0.035	***15.***	***16.***	***17.***	***18.***	***19.***	***20.***	***21.***
η= 0.020	***22.***	***23.***	***24.***	***25.***	***26.***	***27.***	***28.***

Table 5.1 La Jara/Cañon Madera Watershed Test Basin Experimental Design: Constant Width. Each simulation uses variable combinations of Manning's roughness coefficient (η) and stream network length (ΣL) along with the contributing area - stream width geomorphic power law relationship derived from Upper Río Puerco orthophotographs

The first series of model experiments conducted within the La Jara/Cañon Madera test watershed vary ΣL and Manning's roughness coefficient (η), but retain the contributing area - stream width relationship derived from the Upper Río Puerco orthophotographs (Figure 4.2). Table 5.1 provides a convenient list of all model runs within this series. In the horizontal direction, Manning's roughness coefficient is held constant for different stream network lengths. In the table's vertical direction, model simulations preserve total network length but introduce different values for Manning's roughness coefficient.

Manning's roughness coefficients were chosen based upon values determined from channel field studies. *Simcox* (1983) found Manning's η ranges from 0.018 to 0.028 for a wide braided section of the Río Salado just above its confluence with the Río Grande. At a transect along the Río Puerco north of the Bernardo USGS streamgauge, *Griffin et al.* (2005) calculated a Manning's η value of 0.028 from streamflow data while

model results based upon average reach shapes and silt flow lines gave values as high as 0.036. Thus, in this study, $\eta = 0.020$ and $\eta = 0.035$ are considered typical values for Manning's roughness coefficients in arroyo networks. Within the suite of model simulations, Manning's roughness coefficient equal to 0.045 provides a transition value between the 0.0625 value used in the calibrated Upper Río Puerco and more realistic values for Manning's η found in *Simcox* (1983) and *Griffin et al.* (2005). A Manning's roughness coefficient of 0.045 is indicative of a winding stream network that forms shallow pools, has a bed of stoney material, and supports in-stream vegetation (*Dingman*, 2002). Consequently, Manning's η values of 0.0625 and 0.045 may not be reflective of actual arroyo stream network values unless higher values are a result of meandering networks, dense vegetation, or irregular channel cross sections.

The test basin simulation that uses $\eta = 0.0625$ and $\Sigma L = 26.3$ km is referred to as the "standard model run". Five different statistical metrics are used to compare the remaining twenty-seven simulations to the standard model run: correlation coefficient (*CC*), coefficient of efficiency (*E*), the deviation of runoff volume (*Dv*), the mean absolute error (*MAE*), and the root mean square error (*RMSE*). Statistics are calculated using the entire 3,263 hour simulation period. The correlation coefficient is defined as:

$$CC = \frac{\sum_{i=1}^{N}(O_i - \bar{O})(S_i - \bar{S})}{\left[\sum_{i=1}^{N} O_i - \bar{O})^2\right]^{0.5}\left[\sum_{i=1}^{N} S_i - \bar{S})^2\right]^{0.5}}, \qquad 5.1$$

where variables with an overbar are mean values, *O* is the standard simulation value, *S* denotes a new simulation, and *N* is the number of time steps. The correlation coefficient

indicates the degree of linearity between two datasets. Correlation, as defined above, may vary from -1 to 1 where a value of zero implies no correlation. The coefficient of efficiency, or a variation thereof, has been widely used to determine the degree of similarity between predicted hydrographs and stream gauge data (*Legates and McCabe*, 1999). Efficiency is equal to:

$$E = 1.0 - \frac{\sum_{i=1}^{N}(O_i - S_i)^2}{\sum_{i=1}^{N}(O_i - \bar{O})^2}, \qquad 5.2$$

where higher values indicate similarity between the observed and predicted runoff time series. If the efficiency coefficient is negative, the observed mean is a better predictor of rainfall-runoff transformation than the results provided by the hydrologic model. The deviation of runoff volume is determined as:

$$Dv = \frac{\sum_{i=1}^{N}(O_i - S_i)}{\sum_{i=1}^{N} O_i}. \qquad 5.3$$

The mean absolute error and the root mean square error indicate differences between model simulations and observed data in dimensions of the variable. Mean absolute error is calculated as:

$$MAE = N^{-1}\sum_{i=1}^{N}\left|O_i - S_i\right|, \qquad 5.4$$

where *MAE* has the units of m^3/sec. *RMSE* is given by

$$RMSE = \sqrt{\frac{1}{N}\sum_{i=1}^{N}(O_i - S_i)^2}, \qquad 5.5$$

where *RMSE* is also in units of m^3/sec. The following section provides the results of simulations found in Table 5.1.

5.3 Test Basin Results: Constant Width Relationship

Hydrographs and stage diagrams for ΣL values of 26.3 km, 22.8 km, 15.4 km, 4.34 km, and 0.04 km are provided in Figures 5.5 through 5.9. Only a small segment of each 3,263 hour tRIBS simulation is shown because differences between the standard model run and subsequent simulations are not easily recognizable when the entire simulation period is considered. Each discharge and stage diagram shows the maximum flood event for the test basin simulation during hours 2415 to 2440. Within each subplot, the black discharge or stage hydrograph corresponds to the standard model run (Simulation #1) in Table 5.1.

Figure 5.5 shows results for ΣL = 26.3 km and η of 0.045, 0.035, and 0.020 respectively. Timing of the hydrograph peak (t_p) is not significantly altered, but t_p does occur slightly earlier in time with decreasing Manning's η. Additionally, as Manning's η decreases, the hydrograph peak (Q_p) increases and stage decreases. Because the network channel width is held constant for all contributing area values, the reduction in stage height implies streamflow occurs through a smaller cross sectional area at the channel outlet. Consequently, the diminished stage height associated with decreasing Manning's η must be accompanied by increased flow velocity in order to maintain similar Q_p values observed across all simulations.

Figure 5.6 illustrates changes in the stage and discharge hydrographs where ΣL =

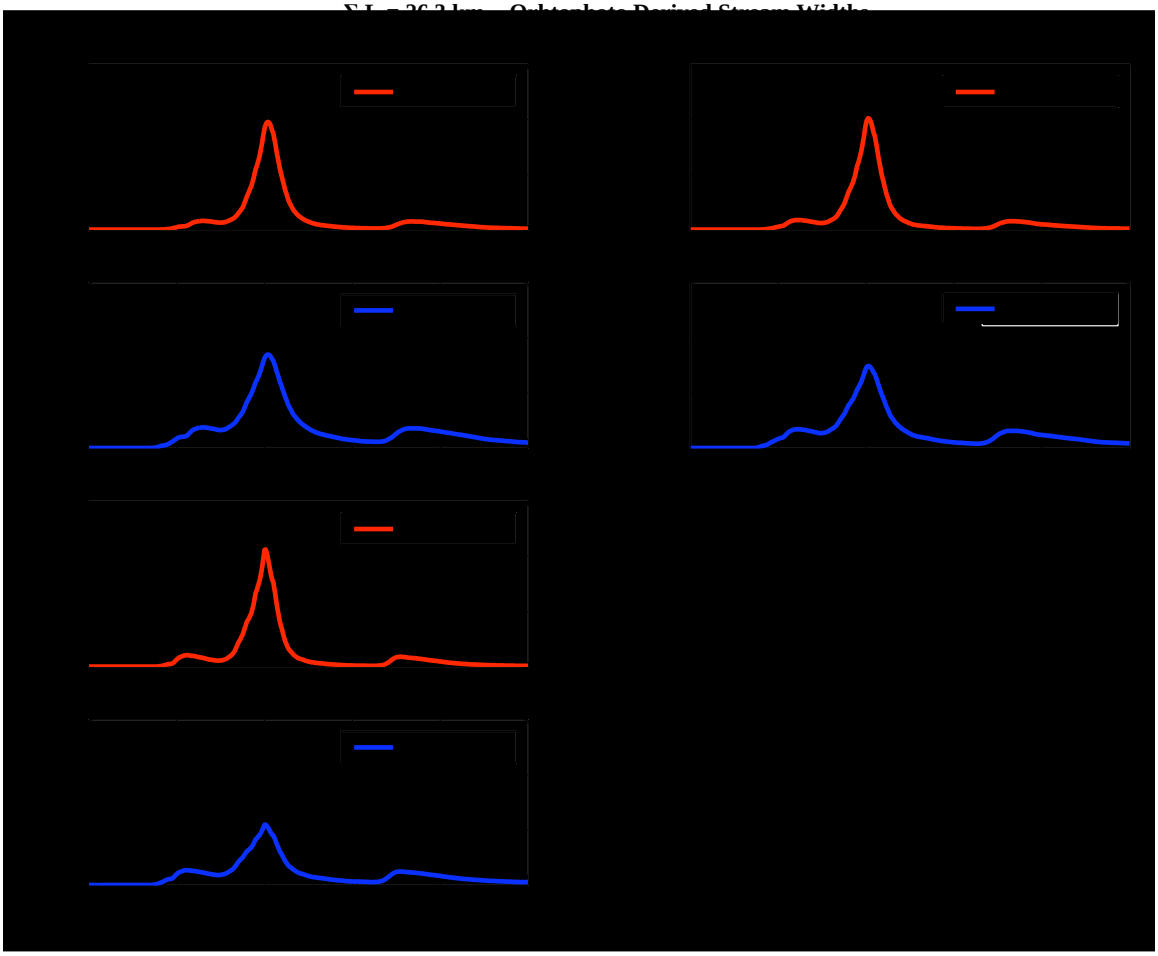

Figure 5.5 Discharge and Stage Hydrographs for ΣL = 26.3 km, Orhtophotograph derived stream widths, and variable Manning's η

22.8 km. As observed when ΣL = 26.3 km, a decrease in Manning's η results in both an increase in Q_p as well as a small shift of Q_p to an earlier time step. Furthermore, streamflow depth decreases with smaller Manning's η, but increased flow velocity maintains similar Q_p across all ΣL = 22.8 km simulations.

Note that in Figure 5.6, the discharge hydrographs produced from lower Manning's η provide a similar, if not improved, approximation to the standard hydrograph. This is due to the balance achieved between channel length, hillslope length, and the time required to route water from the basin. As the stream network shortens, the

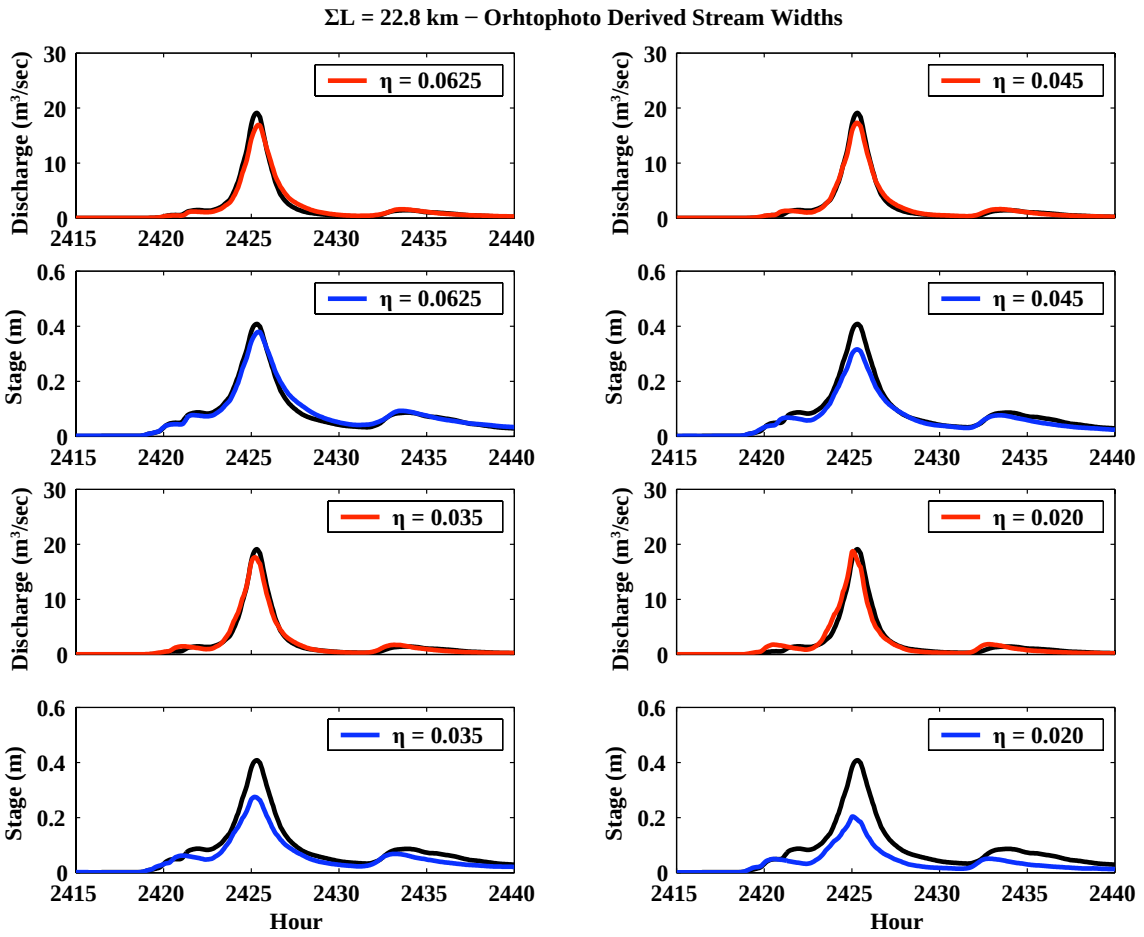

Figure 5.6 Discharge and Stage Hydrographs for ΣL = 22.8 km, Orhtophotograph derived stream widths, and variable Manning's η

average distance from the point of runoff production on the hillslope to the stream network increases. If the hillslope length is extended and Manning's η remains high, both channel and hillslope velocities[1] remain relatively slow. Consequently, runoff arrival at the channel is distributed over a wider time period and in-channel velocities fail to route late arriving runoff swiftly through the channel. Accordingly, the hydrograph becomes wider and Q_p decreases. However, as Manning's η decreases, both in-channel and hillslope velocities increase which compensate for the longer hillslope travel paths.

[1] Hillslope velocities are a function of Manning's η because discharge (Q) appears in the numerator of the hillslope runoff equation and Q is a function of 1/η. See eqs. 2.31 and 2.33

As a result, when ΣL = 22.8 km, a lower Manning's η provides a reasonable approximation to the standard model hydrograph.

At this time, previous research has not examined the sensitivity of hillslope velocity to Manning's η. However, based upon Figure 4.13b, hillslope runoff velocities appear to remain similar across a wide range of contributing areas and discharge values for the given hillslope velocity coefficient and exponent parameters. As a result, the primary effect of variation in Manning's η is likely alteration of streamflow velocity while any consequences for hillslope velocity are secondary in terms of tRIBS model sensitivity.

Figure 5.7 demonstrates changes in the stage and discharge hydrographs for ΣL = 15.4 km. The additional reduction in total network length substantially increases hillslope length and leads to a lower Q_p. Longer hillslope runoff paths and increased overland travel times are no longer balanced by higher streamflow velocities associated with low Manning's η. Consequently the hydrographs for ΣL = 15.4 km do not appear similar to the standard simulation.

Figures 5.8 and 5.9 show tRIBS model results for the La Jara Creek/Cañon Madera test watershed where ΣL = 4.34 km and ΣL = 0.04 km respectively. Although flood peaks are appreciably reduced, runoff volumes remain similar across all simulations as indicated in Table 5.2. These results suggest network extension associated with arroyo incision captures runoff from the hillslope that would have previously reinfiltrated into the soil column, evaporated, or required a longer time period to reach the watershed

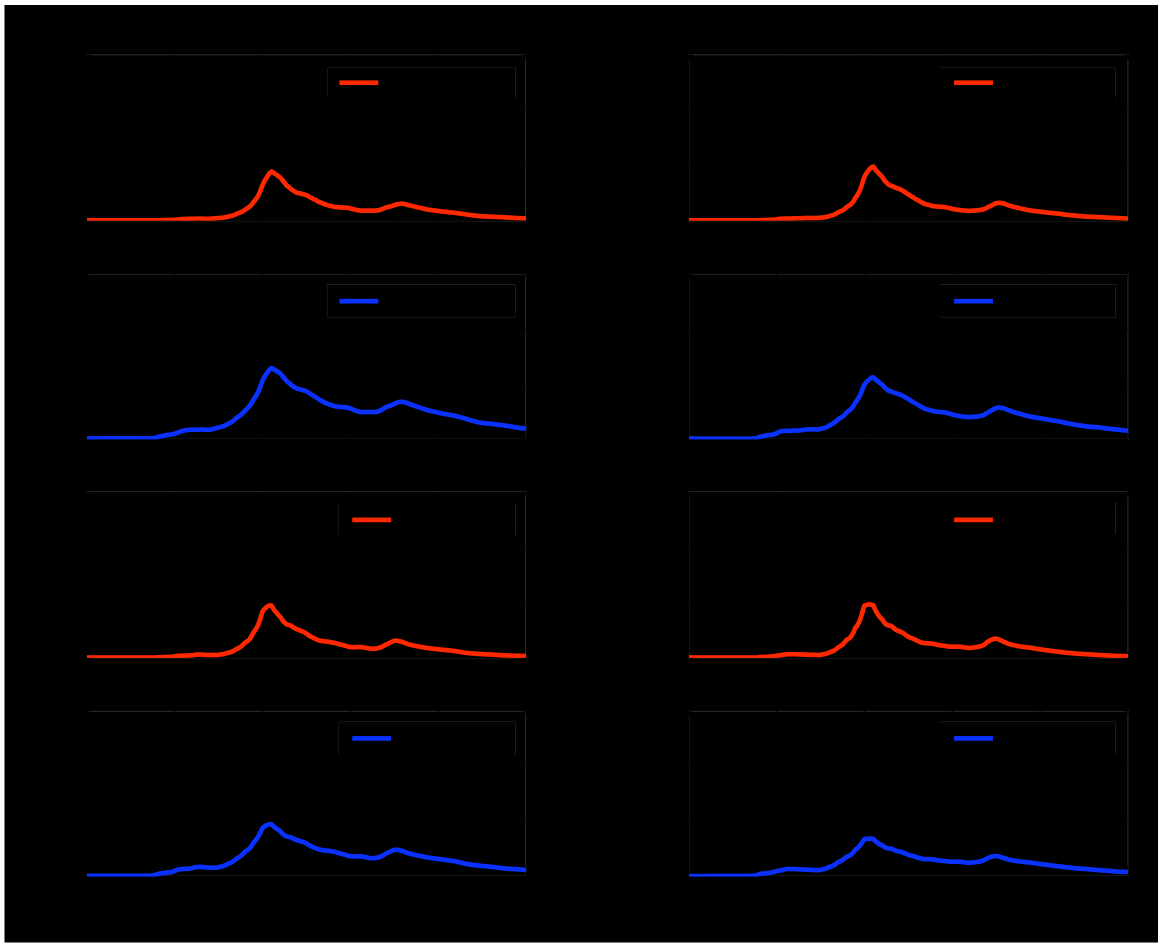

Figure 5.7 Discharge and Stage Hydrographs for ΣL = 15.4 km, Orhtophotograph derived stream widths, and variable Manning's η

outlet. Thus, short channels tend to support smaller Q_p and distribute streamflow volumes over longer time durations whereas extended stream networks concentrate hillslope runoff in the channel and are capable of producing larger floods over limited periods of time.

Finally, Figure 5.10 provides the statistical metrics for all discharge hydrographs listed in Table 5.1. In the following discussion, the terms "error" and "sensitivity" are used interchangeably to describe statistical differences between the various tRIBS simulations performed and the standard model run. Again, the standard simulation uses a

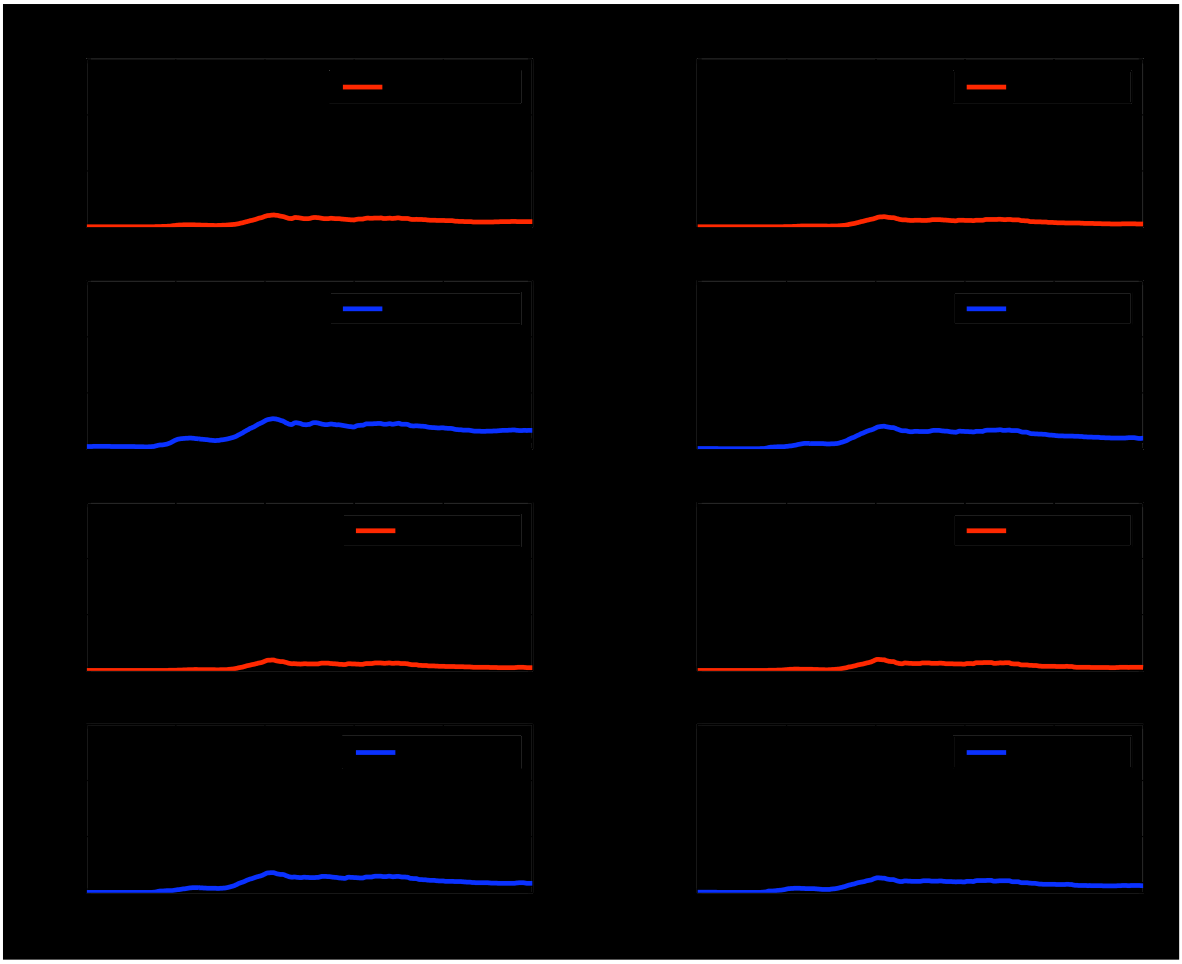

Figure 5.8 Discharge and Stage Hydrographs for ΣL = 4.34 km, Orhtophotograph derived stream widths, and variable Manning's η

Manning's η = 0.0625 and ΣL = 26.3 km. Consequently, the standard simulation will have both the slowest in-channel velocities and the shortest hillslope lengths.

The *RMSE* and *MAE* indicate that for long channel lengths (i.e., ΣL = 26.3 km, 24.4 km), simulations using low Manning's η have more error than simulations using higher Manning's η (Figure 5.10a and 5.10e). For these test basin simulations, the total stream network length remains long and the decrease in Manning's η merely leads to an increase in streamflow velocities and Q_p (refer to Figure 5.5). However, as ΣL decreases to 22.8 km, models using Manning's η of 0.045 and 0.035 possess lower error than

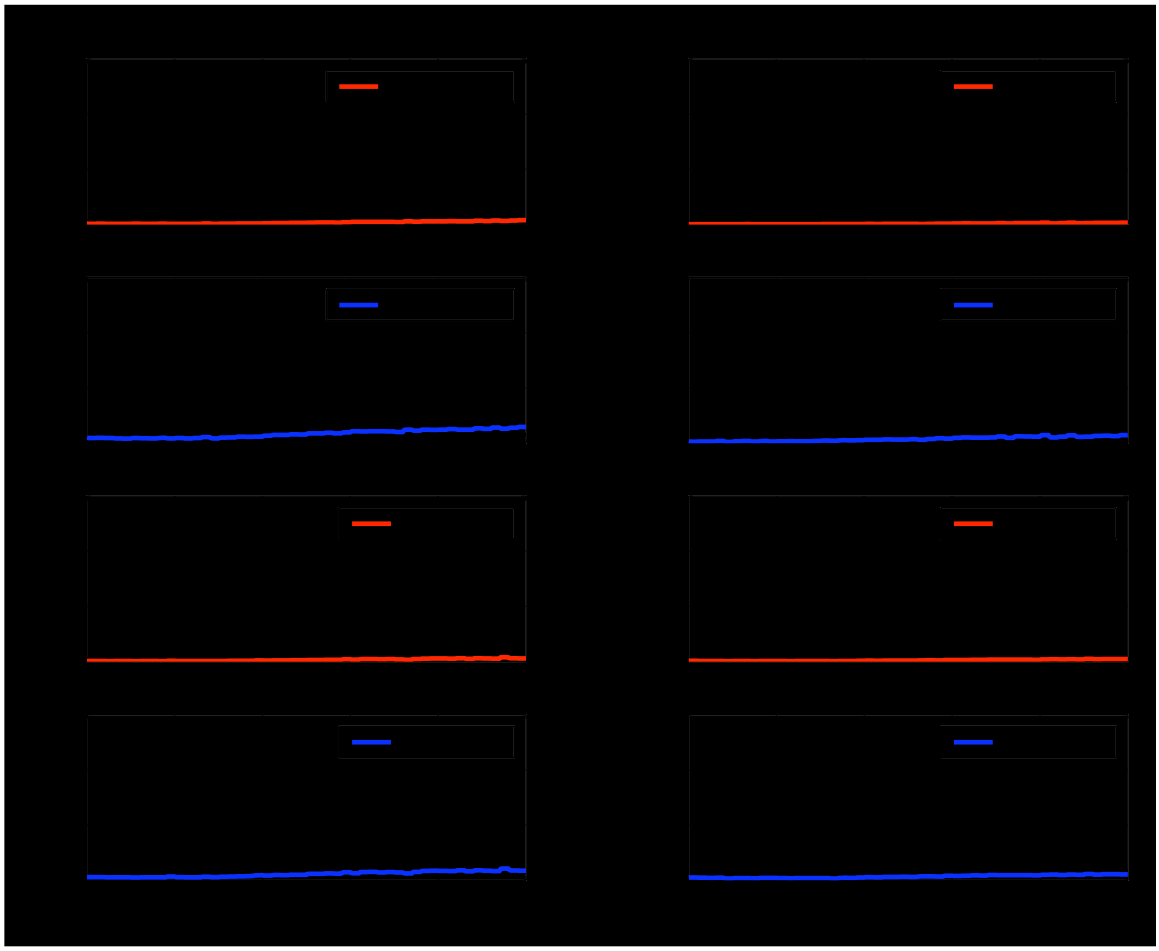

Figure 5.9 Discharge and Stage Hydrographs for ΣL = 0.04 km, Orhtophotograph derived stream widths, and variable Manning's η

models with Manning's η of 0.0625. For these simulations, a balance is reached between the increased time required for runoff to reach the channel and the increase in channel velocity as water is routed through the stream network. As the network shortens to ΣL of 21.0 m, simulations with Manning's η equal to 0.020 also improve over test basin runs with Manning's η of 0.0625. Once the channel network is pruned shorter than 21 km, *RMSE* and *MAE* increase for all Manning's η.

Efficiency and the correlation coefficient provide similar information as the *MAE* and *RMSE* statistics (Figure 5.10b and Figure 5.10c). For Manning's η of 0.045, *E* and

	ΣL 26.3 km	ΣL 24.4 km	ΣL 22.8 km	ΣL 21.0 km	ΣL 15.4 km	ΣL 4.34 km	ΣL 0.04 km
η= 0.0625	3.5134	3.5110	3.5156	3.5097	3.4968	3.5318	3.5290
η = 0.045	3.5125	3.5102	3.5131	3.4969	3.5402	2.9617	3.5364
η= 0.035	3.5142	3.5136	3.5148	3.5012	3.5200	2.9366	3.5388
η= 0.020	3.5129	3.5132	3.5153	3.5209	3.5253	2.9847	3.5395

x 10^5 m^3

Table 5.2 La Jara/Cañon Madera Watershed Test Basin Simulations - Streamflow volume comparisons in units of 10^5 m^3. Note the differences in volumes for ΣL = 4.34 km and η = 0.045, 0.035, and 0.020 respectively when compared to other simulations. Differences may be due to model error or a mistake during model setup.

CC reach a maximum value for ΣL of 22.8 km. Simulations with Manning's η of 0.020 and 0.035 reach a maximum *CC* and *E* value for ΣL of 21.0 km. Once the network is clipped shorter than ΣL = 20.0 km, *E* and *CC* decrease steadily. As the efficiency coefficient approaches zero, the mean of the standard simulation is as good a predictor of runoff as the network with ΣL of 0.04 km. This occurs because the coefficient of efficiency is biased by the extended periods of low discharge common to all performed simulations.

Deviation of runoff volume reaches a maximum for Manning's η equal to 0.045, 0.035, and 0.020 when ΣL is 4.34 km (Figure 5.10d). High values for the deviation coefficient occur when substantial volumetric differences are present between observed and simulated data over the modelling duration. Inspection of Table 5.1 shows that for ΣL = 4.34 km and Manning's η of 0.045, 0.035, and 0.020, model streamflow volume is

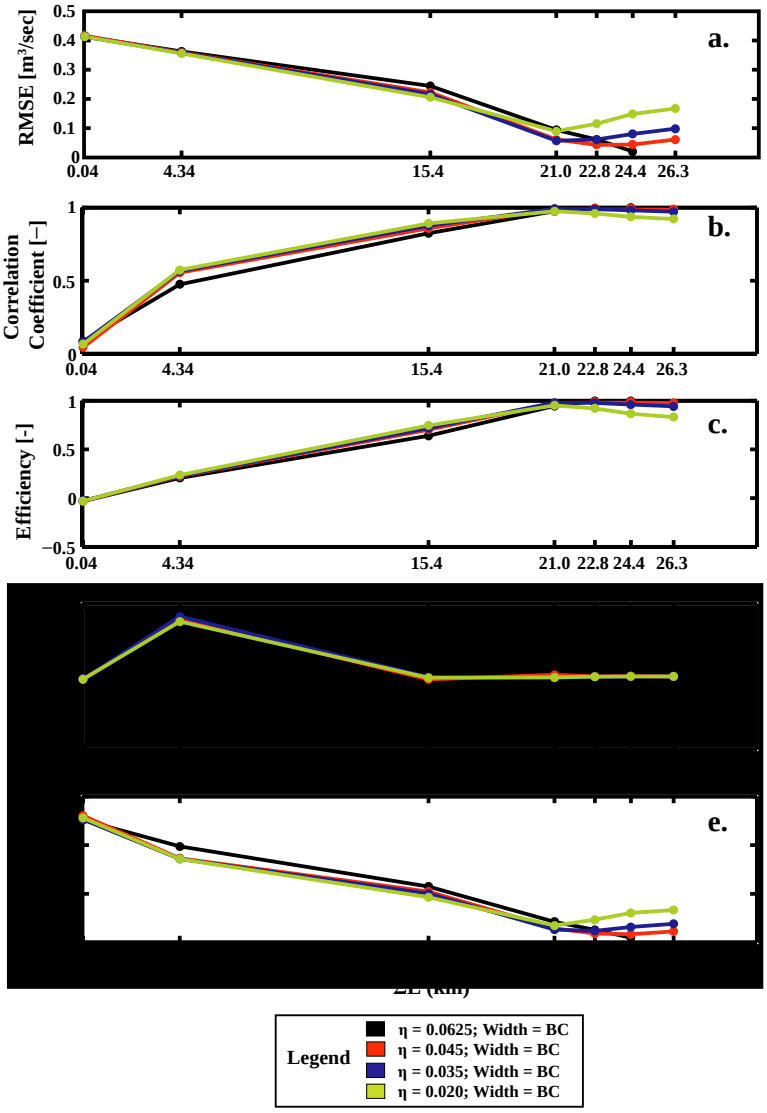

Figure 5.10 Statistical Metrics for La Jara Creek/Cañon Madera test watershed using the orthophotograph derived contributing area - stream width relationship

underestimated compared to all other runs. Underestimation may have resulted from tRIBS model error or a mistake in model setup. If flow volumes or cumulative discharge are the same between two model simulations, overestimations will eventually balance underestimations and the numerator in Equation 5.3 will sum to zero. Only when streamflow totals vary between simulations will the deviation statistic provide a value other than zero.

Finally, all metrics converge to a common value as the network is removed from the test watershed. Within these simulations, extracting the stream network from the Voronoi topographic representation minimizes any model variability due to changes in Manning's η. The observed error is a manifestation of transferring the dominant routing mechanism in the model from the channel to the hillslope.

5.4 Test Basin Experimental Design: Arroyo Development Scenarios

The next series of simulations utilize stream network lengths and Manning's η values discussed previously, but introduce additional changes in channel network width. The added variability in stream width is designed to quantify streamflow response for the different conceptual stages of arroyo development described in Section 3.2.3. To alter the channel widths, new contributing area - stream width power laws were created based upon the Upper Río Puerco derived geomorphic power law.

Figure 5.11 shows the original Upper Río Puerco contributing area-stream width relationship (BC) along with two curves that apply a wider network condition (W1 and W2) and two curves that utilize a narrower condition (N1 and N2). The additional power laws allow stream width at the Upper Río Puerco outlet to vary from 21.0 m (68.9 ft) to 51.3 m (186 ft). If power laws are applied to the La Jara Creek/Cañon Madera test watershed where ΣL is 26.3 km, channel widths at the watershed outlet vary from 12.5 m (41.0 ft) to 21.1 m (69.0 ft) due to smaller basin area. Geomorphic power laws W1 and W2 are utilized in model simulations designed to approximate streamflow response of arroyo networks experiencing inner floodplain development. Geomorphic power laws

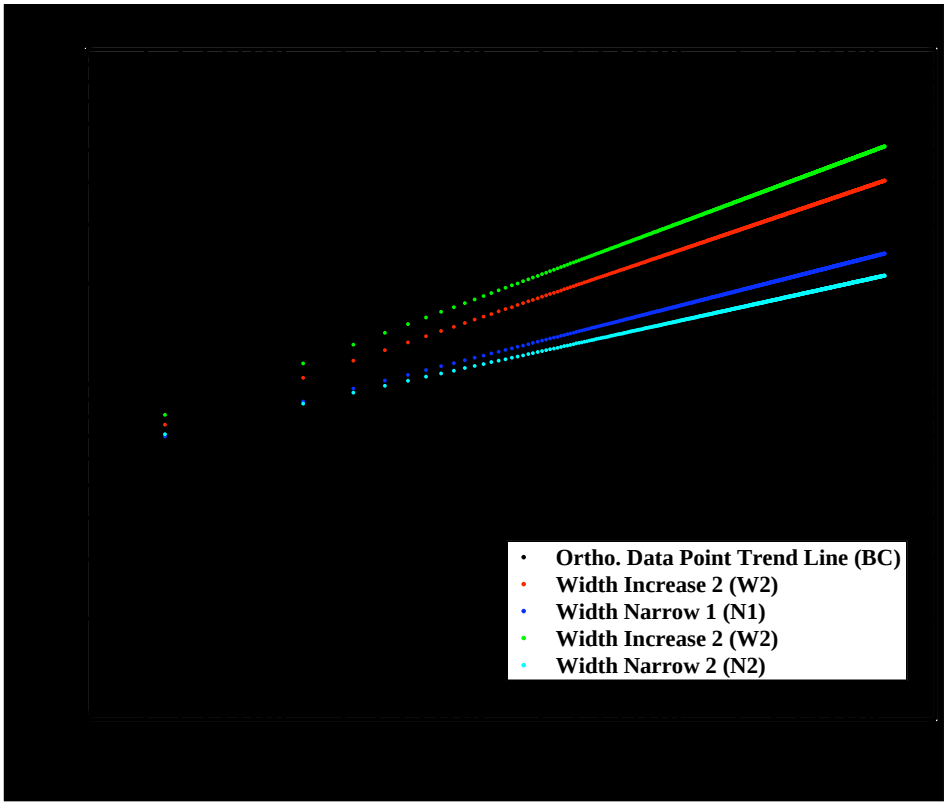

Figure 5.11 Geomorphic power laws used for investigating runoff response across different stages of arroyo development.

N1 and N2 are used during simulations aimed at replicating watershed response to lateral erosion, vertical channel incision, and stream network extension. The number *2* provides indication that the power law applies either the narrowest (N2) or widest (W2) channel widths within this study.

Channel widths are not reflective of the entire arroyo extent that stretches from one remnant of the pre-incision valley floor to another. Instead, widths are designed to represent the location of streamflow concentration within arroyo channel walls (e.g., active inner channel). Channel widths at high contributing areas are considered reasonable based upon stream width measurements for large arroyo networks (*Elliott et al.*, 1999). However, widths at low contributing areas (i.e., 0.25 km^2) may be

overestimated.

Headwater stream channel widths are based upon measurements from Upper Río Puerco orthophotographs conducted in a GIS. Lower stream order sampling locations are concentrated in the northwest section of the basin where underlying geology is comprised of easily eroded sandstone and shales. Readily eroded sediments may explain why tributaries resemble exceedingly wide ephemeral washes within the orthophotographs. Although lower order reaches appear broad, flow events may be localized to a smaller cross section of the wash. Identifying the typical streamflow location within the wash is difficult based upon orthophotographs alone. Consequently, stream channel widths of ~7 m (~23 ft) may be an overestimation for arroyos with upstream contributing areas of ~ 0.25 km^2.

In addition to changing network widths and lengths, altering Manning's η allows the representation of different phases of arroyo development. Because the calibrated Manning's η was exceedingly high in the Upper Río Puerco, it is assumed that elevated roughness is perhaps due to the establishment of vegetation on the inner floodplain of the channel. This would suggest that on average, the Upper Río Puerco is in a stage of channel and inner-floodplain stabilization. However, it is known that sections of the Upper Río Puerco stream network still propagate back and forth across the inner-floodplain and contribute to additional channel widening through lateral erosion (personal communication, *Love* 2007). Consequently, specific reaches in the Upper Río Puerco could be classified within different stages of arroyo development.

	ΣL 26.3 km	ΣL 24.4 km	ΣL 22.8 km	ΣL 21.0 km	ΣL 15.4 km	ΣL 4.34 km
η= 0.0625	23. BC	x	x	x	x	x
η = 0.045	22. BC 21. W1	x	x	x	x	x
η= 0.035	20. W1 19. W2	16. BC	14. BC 12. N1	10. N1 9. N2	6. N1 5. N2	2. N2
η= 0.020	18. W1 17. W2	15. BC	12. BC 11. N1	8. N1 7. N2	4. N1 3. N2	1. N2

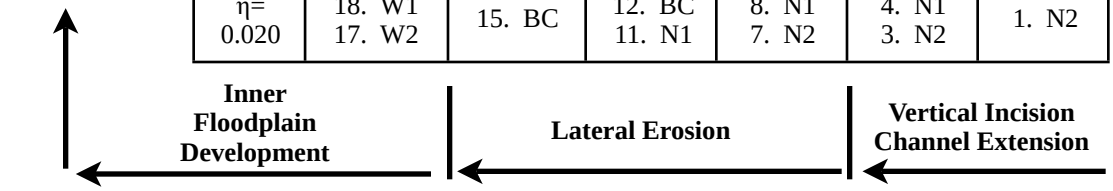

Table 5.3 La Jara/Cañon Madera Watershed Test Basin Arroyo Development Experimental Design. Each simulation utilizes various combinations of contributing area - stream width geomorphic power laws, Manning's η, and total stream network length (ΣL).

Nonetheless, assigning the calibrated Upper Río Puerco tRIBS model a channel and inner-floodplain development arroyo stage designation provides a starting point for investigating the effects of arroyo development. Simulations are first performed using the La Jara Creek/ Cañon Madera test watershed. Different phases of arroyo development applied to the test basin are then considered in the Upper Río Puerco watershed.

Table 5.3 provides a listing of all model simulations performed for the arroyo development simulations in the La Jara Creek/Cañon Madera test watershed. Simulation #23 possess Manning's η of 0.0625, the BC channel width power law, and ΣL of 26.3 km. It is identical to simulation #1 in Table 5.1 and is considered the standard model run. Discharge and stage hydrographs for the standard model run appear in black behind discharge and stage plots for the remaining 22 simulations listed Table 5.3 (see Figure 5.12 as an example). Maintaining the standard model run in all figures facilitates

hydrograph comparison between simulations. Statistical metrics provided at the end of this section are based upon the standard simulation.

Following the arrows found in Table 5.3 traces the stages of arroyo development towards a period of channel and inner floodplain stabilization. Simulations #1 through #6 represent the vertical incision and channel extension phase of arroyo evolution. Within this particular conceptual stage, arroyos are confined to narrow channels and headcuts migrate upslope. The various model runs allow multiple transitional pathways within a given stage of arroyo development. For example, an acceptable arroyo parameterization could be achieved using the N2 power law, ΣL = 4.34 km, and Manning's η of 0.035 (Simulation #2). As the headcut progresses upstream (ΣL = 15.4 km), the channel may widen to the N1 condition due to increased shear stress on channel walls associated with larger flood events. Furthermore, Manning's η may decrease to 0.020 as vegetation is removed from the riparian corridor. However, if the dominant mechanism within this stage is merely channel extension and the network does not widen appreciably, then transition from Simulation #2 to Simulation #5 could be more reasonable (N2; Manning's η = 0.035; ΣL = 15.4 km). Thus, different simulations allow variability in streamflow response within each geomorphic stage of arroyo development. In addition, altering model parameterization allows investigation into tRIBS model sensitivity for different combinations of channel lengths, Manning's η, and geomorphic width relationships.

Despite using geomorphic power laws that apply narrower stream widths to watershed representations with smaller ΣL, headwater stream widths may be overestimated within these simulations. As ΣL decreases, the contributing area at the

position of the head water streams increases (see Figure 5.3). Unfortunately, this was not considered in the new geomorphic power law contributing area - width relationships. For example, headwater stream networks that use the N2 relationship along with ΣL values of 4.34 km possess channel widths of ~11 m (36 ft) rather than the intended value of ~7 m (22 ft). It may be argued that the head water streams for ΣL = 4.34 should be wider because these networks have more cells contributing runoff than headwater streams delineated using lower constant area thresholds. Nonetheless, N2 and N1 power laws likely overestimate channel widths for shorter stream networks (i.e. ΣL = 4.34 and ΣL = 15.4).

Simulation #7 through #16 attempt to approximate the lateral erosion period within the conceptual arroyo evolution model. Again, test watershed simulation design allows this entire phase to progress through various combinations of ΣL, Manning's η, and stream widths. The stream network is considered in the early stages of lateral erosion when ΣL is 21.0 km. As erosion of arroyo walls continues, network extension slows and channel widths gradually widen to the BC width (Simulationsl #11 through #16).

Lateral erosion is followed by inner floodplain development and stabilization (Simulations #17 through #23). Models in the inner floodplain development stage use a slightly extended network while channel widening continues (Simulations #17 through #20). With the establishment of riparian vegetation and contributions of sediment from upstream incising reaches, the channel begins to narrow and aggrade (Simulations #21 through #23). Channel and inner floodplain stabilization reflects the continued recovery of incised river networks, however, streambed elevation may not reach the pre-incision

valley floor. The following section describes results for different model representations of the various stages of the arroyo geomorphic sequence for the La Jara Creek/Cañon Madera test watershed.

5.5 Test Basin Results: Arroyo Development Scenarios

Discharge and stage hydrographs for Manning's η of 0.035, the N2 geomorphic power law, and ΣL of 4.34 km are provided in Figure 5.12a and 5.12b. Also shown in Figure 5.12c and 5.12d are the discharge and stage hydrographs for Manning's η of 0.020, the N2 geomorphic power law, and ΣL of 4.34 km. These runs correspond to an arroyo network within the vertical incision and network extension phase of arroyo evolution. As seen in the previous series of test runs with constant channel width, a shorter channel network decreases Q_p and distributes runoff over a prolonged time period. Constricting the channel width from the BC (Figure 5.8) to the N2 condition (Figure 5.12) does not alter tRIBS modelled streamflow response such that a rising or falling limb of the hydrograph is well defined. Furthermore, comparison of Figures 5.12b and 5.12d suggest that decreasing Manning's η results in a slight decrease in stage. However, examination of Figures 5.12a and 5.12c reveal that the variability in stage imparts minimal effect on discharge hydrographs. Thus, within this stage of the geomorphic sequence, limited channel length is the major controlling factor on hydrograph shape and short networks reduce the potential for large flood generation.

In Figure 5.13 the channel is extended to 15.4 km. Four model runs are performed for this channel length: (1) Manning's η of 0.035 and the N1 geomorphic law;

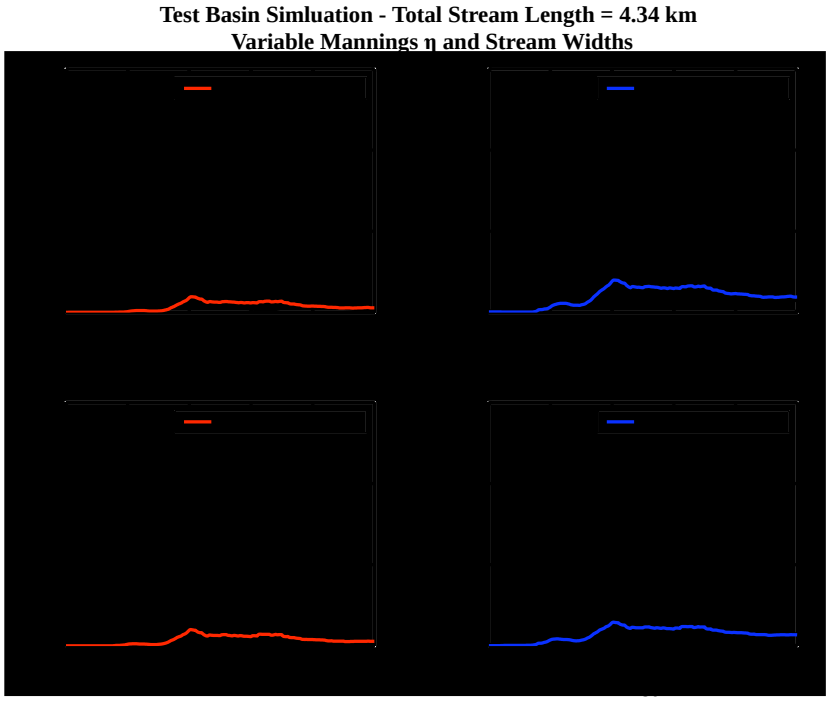

Figure 5.12 Discharge and stage hydrographs for ΣL = 4.34 km, Manning's η of 0.035 and 0.020, and N2 geomorphic power law contributing area - stream width relationship

(2) Manning's η of 0.035 and the N2 geomorphic power law; (3) Manning's η of 0.020 and the N1 geomorphic power law; and (4) Manning's η of 0.020 and the N2 geomorphic power law. These simulations correspond to a channel that is continuing to extend up slope. Increase in channel width may occur as longer channel networks lead to larger flood magnitudes which impart greater shear stresses on channel walls. Comparison of Figure 5.12 and 5.13 demonstrate that channel network extension diminishes average hillslope length and leads to a hydrograph with improved definition on the rising and falling limbs.

Examination of Figure 5.13 reveals that for a given Manning's η and ΣL = 15.4 km, there is a slight decrease in Q_p for the narrower channel. As an example, when

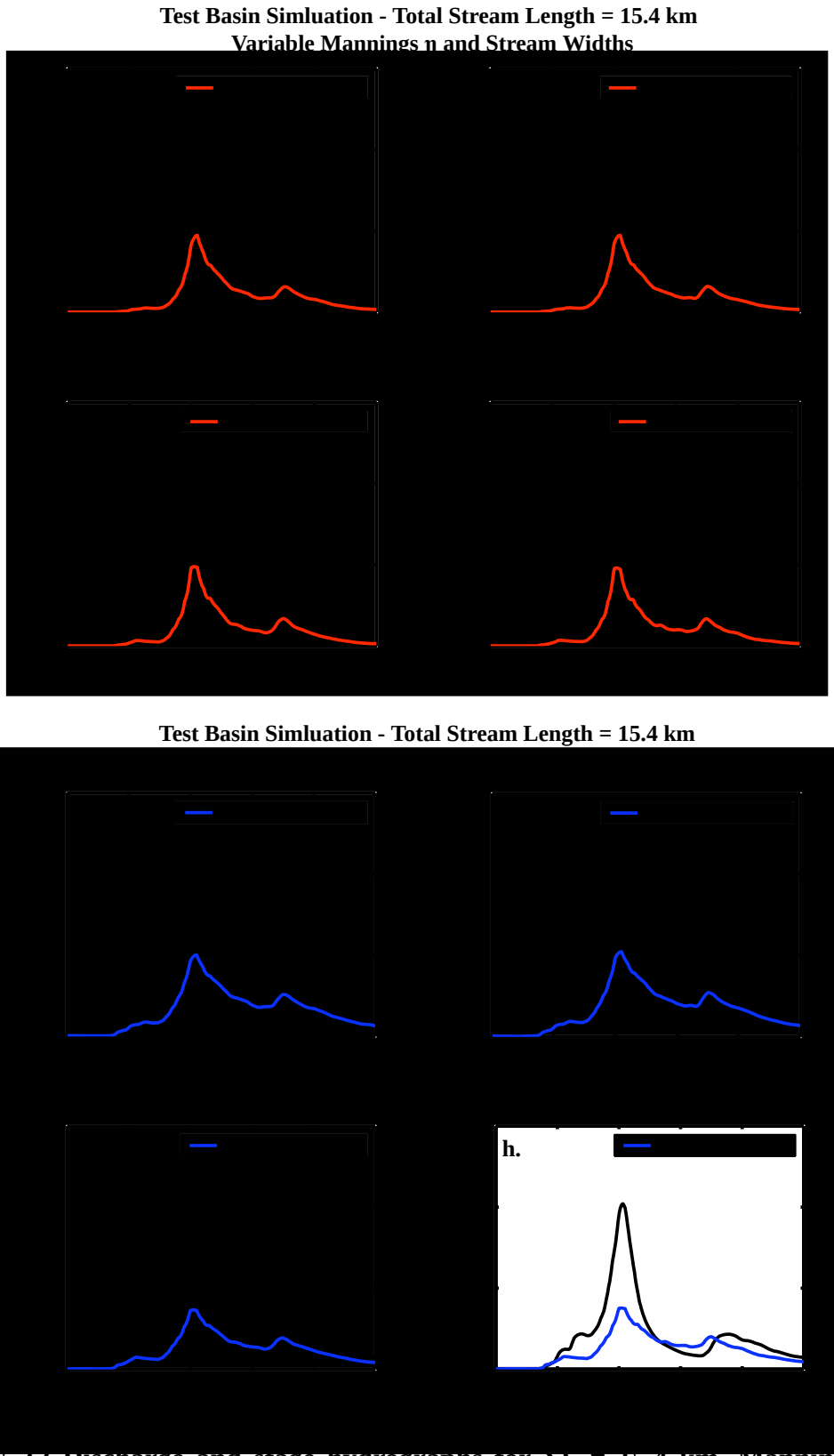

Figure 5.13 Discharge and stage hydrographs for ΣL = 15.4 km, Manning's η of 0.035 and 0.020, and N1 and N2 geomorphic power law contributing area - stream width relationships

Manning's η = 0.020 and channel widths are applied using the N1 power law, Q_p is equal to 9.77 m^3/sec (Figure 5.13c). If Manning's η remains constant and the N2 relationship is used instead, Q_p decreases to 9.60 m^3/sec (Figure 5.13d).

The decrease in Q_p may be small but it also proved to be unexpected. The assumption prior to conducting simulations was that narrower channels would constrict flow and generate higher streamflow velocities, stage, and discharge peaks. Within actual arroyo networks, narrowing of the channel may lead to overbank flow, which is not currently simulated in the model. As a result, decreasing Q_p with narrower channels cannot be attributed to overbank losses.

To investigate possible causes for declining Q_p associated with narrower stream widths, streamflow velocity, and streamflow cross sectional area are estimated at the time corresponding to Q_p (Table 5.4a). Because streamflow depth, stream discharge, and channel width are all known at the outlet, streamflow velocity can be easily approximated given:

$$\bar{V} = \frac{Q_p}{WD}, \qquad 5.6$$

where V overbar is velocity, Q_p is peak discharge, W is channel width, and D is stage. The denominator in equation 5.6 represents the streamflow cross sectional area.

Results in Table 5.4a show that as channel width decreases (i.e., N2), stage and streamflow velocity increase. However, the increased velocity and channel depth observed for the narrower channel simulation is not sufficient to cause an increase in Q_p.

a.

η = 0.020	Q_p (m^3/sec)	Stage (m)	Outlet Channel Width (m)	Velocity (m/s)	Flow Cross Sectional Area (m^2)
N1	9.77	0.146	24.7 m	2.7	3.6
N2	9.60	0.151	21.1 m	3.0	3.2

b.

η = 0.020	Streamflow Volume Rising Limb (m^3)	Streamflow Volume Falling Limb (m^3)	Streamflow Volume Entire Simulation (m^3)
N1	4.32×10^4	1.27×10^5	3.53×10^5
N2	4.04×10^4	1.27×10^5	3.51×10^5

Table 5.4 a. Comparison of hydrograph characteristics for two different channel width representation and Manning's η = 0.020 with ΣL = 15.4 b. Comparison of flow volume distribution for rising and falling limbs of Q_p at hour 2425 as well as entire simulation flow volumes

For the N2 simulations, introducing smaller widths in Manning's equation yields a lower Q_p despite higher velocity and stage values.

Streamflow volumes were calculated for the total simulation period to ensure that both model runs generate similar total discharge and the resulting differences in the hydrograph peaks are not due to model error (Table 5.4b). Over the entire simulation period, the N1 model generates 2,000 m^3 more streamflow volume than the model run using N2. This translates to a difference between model runs of only 0.5%, so the slight variation may be regarded as minimal.

In addition, flow volumes were calculated under the rising and falling limbs of both N1 and N2 simulations to examine whether changes in channel width redistributes water to different segments of the flood event hydrograph (Table 5.4b). Beneath the

rising limb, streamflow volumes are only slightly higher for the N1 simulation. Under the descending limb, discharge volumes are the same. Thus, application of a narrower channel condition (N2) does not significantly alter tRIBS hydrograph shape or flood event discharge volumes.

One additional possibility that could explain the observed decrease in Q_p for the N2 simulation, is the reallocation of discharge from the major flood event that occurred over hours 2415 - 2440 to one of the earlier secondary discharge peaks. Figure 5.14 shows the entire period of simulation with two secondary flood events and the primary flood peak magnified in figure insets. For the two early flood events at hours 2158 and 2272 (Figure 5.14a and 5.14b), the N2 simulation hydrograph peaks are slightly higher than the N1 hydrograph peaks. However, in later time (Figure 5.14c), the N2 Q_p is less than N1 Q_p as discussed above.

Results suggest that for a particular watershed, a narrower channel condition may alter tRIBS discharge hydrographs such that streamflow peaks in earlier time are larger relative to a model with a wider channel representation. In contrast, flood event peaks in later time are smaller relative to simulations using broader stream networks. However, the differences in Q_p for different flood events across both N1 and N2 simulations are minimal. Consequently, alteration of channel width for simulations using a short channel network does not have a significant effect on hydrograph character although slight redistribution of discharge to earlier flood events may occur.

Figure 5.15 provides the discharge and stage hydrographs for ΣL of 22.8 km.

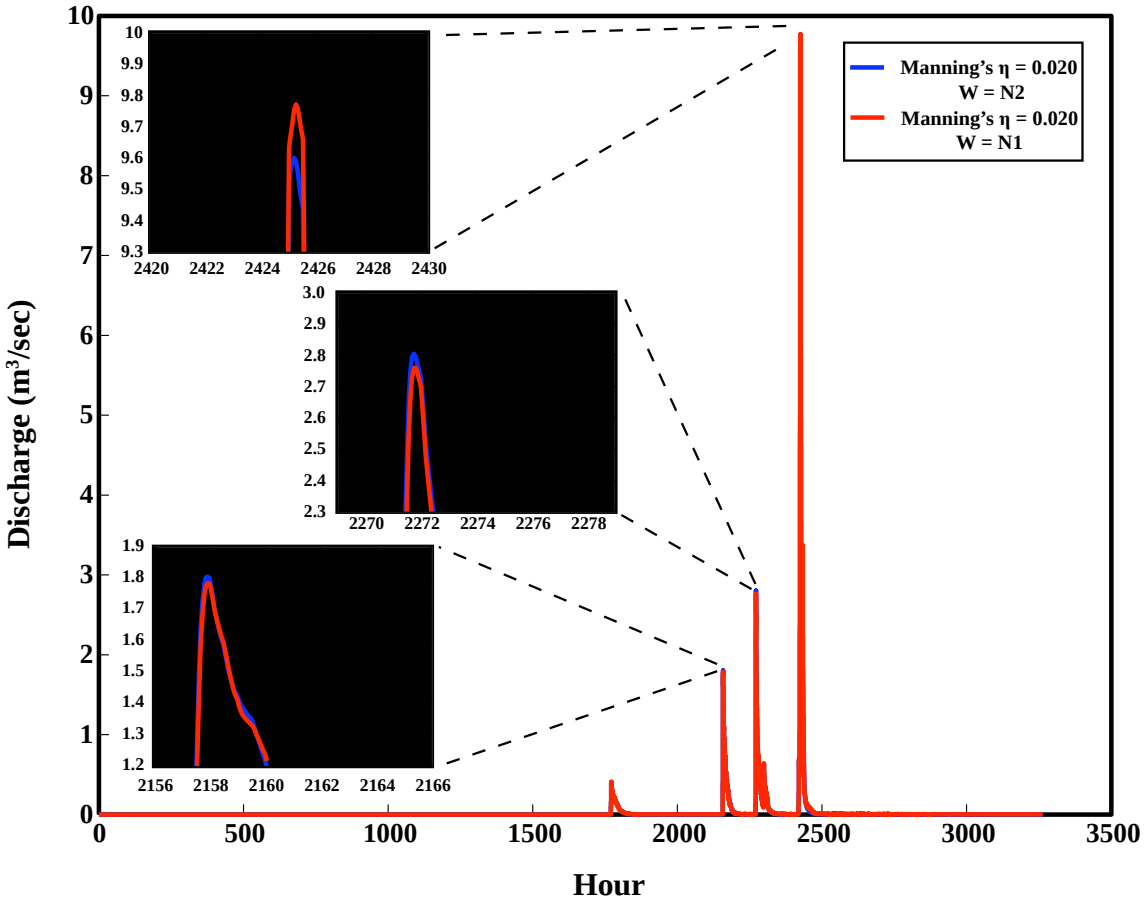

Figure 5.14 Comparison of main flood event as well as secondary flood pulses for N1 and N2 simulations with Manning's η = 0.020

Simulations are performed using Manning's η of either 0.020 or 0.035 and geomorphic power laws of either N1 or BC. Longer stream network length in these model runs is designed to replicate channel extension up slope. As the channel grows longer and concentrates runoff in the channel network, flood event magnitude increases as does the shear stress imparted on channel walls. Thus, the transition from N1 to BC represents gradual channel widening as increased discharge imparts greater erosive forces on the channel walls.

Figure 5.15 allows comparison of discharge or stage for constant Manning's η and

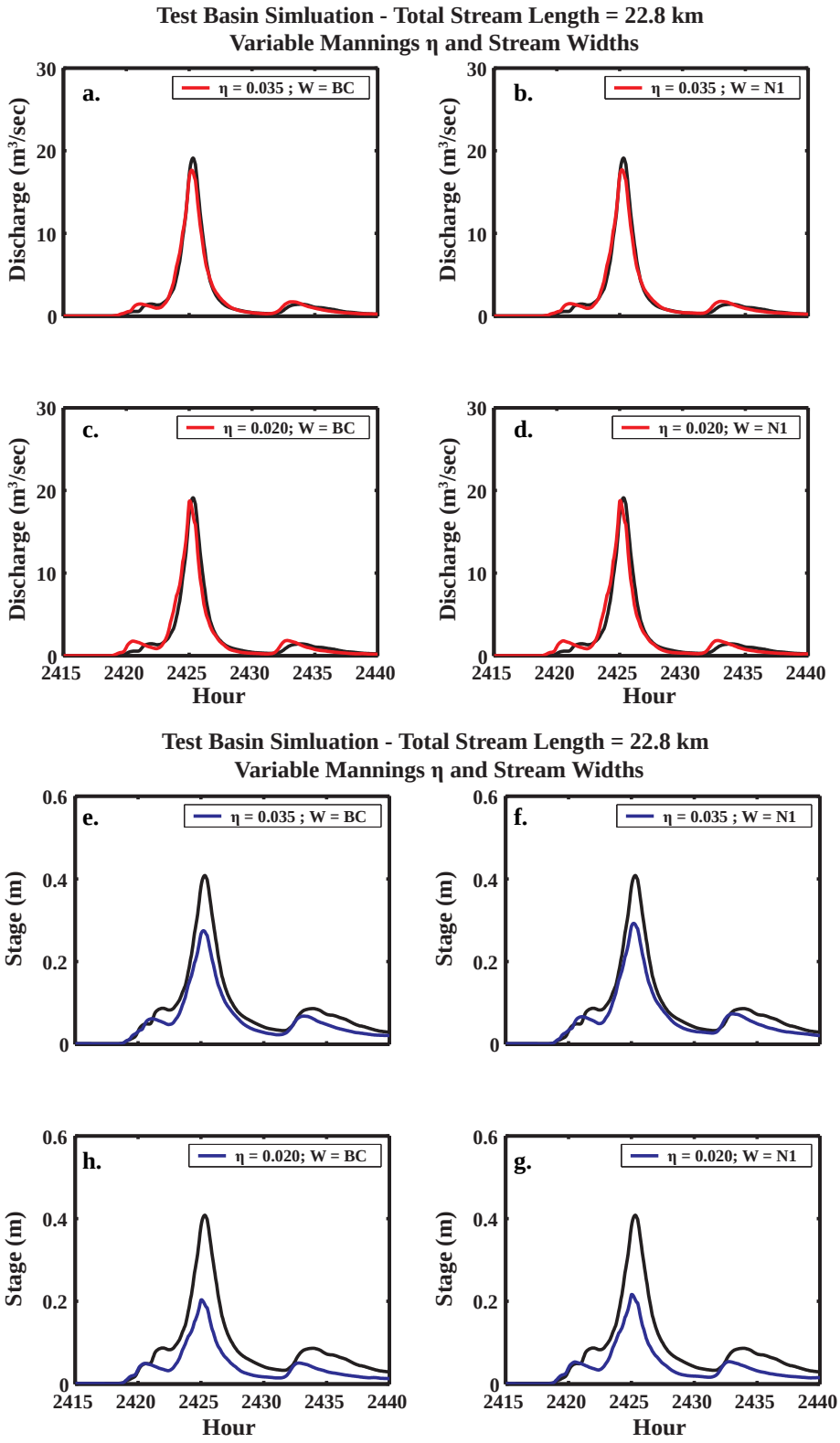

Figure 5.15 Discharge and stage hydrographs for ΣL = 22.8 km, Manning's η of 0.035 and 0.020, and BC and N1 geomorphic power law contributing area - stream width relationships

varying channel widths (i.e., horizontal direction) or constant channel width and varying Manning's η (i.e. vertical direction). For a given Manning's η and ΣL = 22.8 km, channel width alteration has minimal effect on the shape of the discharge hydrograph. (Figure 5.15a versus 5.15b or Figure 5.15c versus 5.15d). However, comparison of 5.15a with respect to 5.15c reveals that a decrease in Manning's η results in an increase in the main hydrograph peak at hour 2425 as well as a rise in the small flood events at hour 2420 and 2432. Examination of 5.15e and 5.15h shows that this increase in discharge corresponds with a decrease in stage. Similar results are observed when comparing Figures 5.15b and 5.15d with respect to 5.15f and 5.15g.

Figure 5.16 shows the last two simulations in the lateral erosion phase of arroyo development. The channel network has extended slightly upslope (ΣL = 24.4 km) while additional widening of the arroyo is reflected by the BC stream width contributing area power law relationship. The growth in channel length again imparts an observable change in the hydrograph. For example, Figure 5.15a and Figure 5.16a maintain constant Manning's η, utilize the same geomorphic stream width - contributing area power law, but lengthens the network by ~ 7%. The additional channel length dissects the basin terrain, decreases hillslope lengths, and concentrates runoff in the channel shortly after rainfall events. This results in an increase in the hydrograph peak. Comparing Figures 5.16a and Figure 5.16c demonstrates that the increase in channel velocity associated with a decrease of Manning's η from 0.035 to 0.020, shifts the hydrograph to slightly earlier time steps and leads to a modest increase in $Q_{p.}$

The next group of simulations correspond to the inner flood plain development

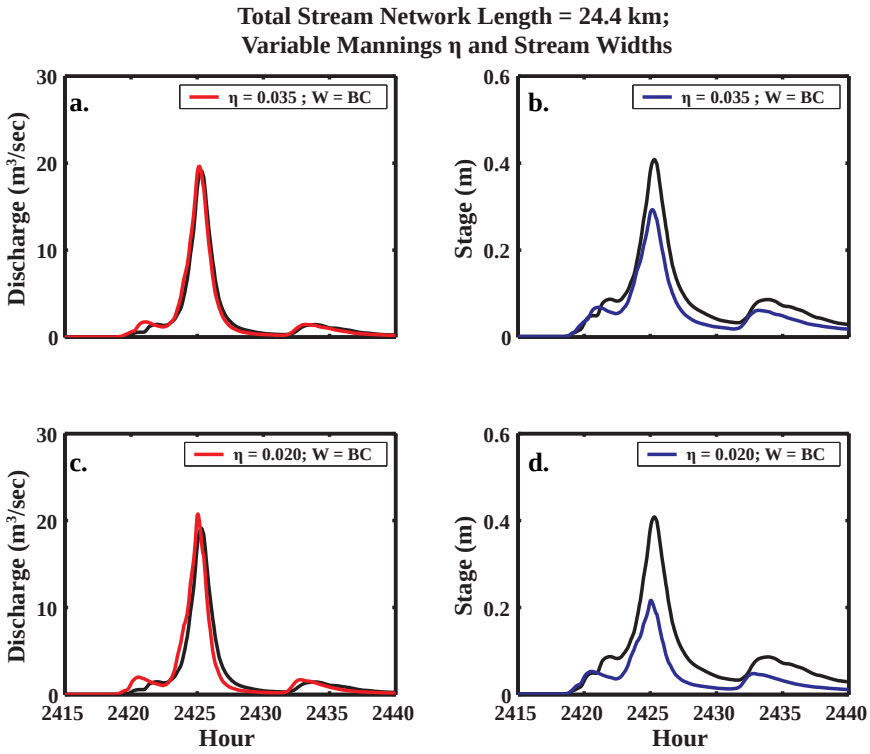

Figure 5.16 Discharge and stage hydrographs for ΣL = 24.4 km, Manning's η of 0.035 and 0.020, and BC geomorphic power law contributing area - stream width relationship

stage of the arroyo geomorphic sequence. At this point of arroyo evolution, the network has reached its widest state. Arroyo widening is reflected through the W1 and W2 power laws used within these tRIBS simulations. All model runs within this phase assume channel network extension is now minimal and the main geomorphic response is channel width adjustment. Accordingly, total channel length is held constant at 26.3 km.

Figures 5.17a through Figure 5.17d show discharge hydrographs corresponding to arroyo inner floodplain development. Simulations with Manning's η = 0.020 possess the highest discharge peaks (Figure 5.17a and Figure 5.17b). If Manning's η increases to 0.035 the discharge peak decreases slightly (Figure 5.17c and Figure 5.17d). Comparison of Figure 5.17a and 5.17b or Figure 5.17c and Figure 5.17d demonstrates that for a given

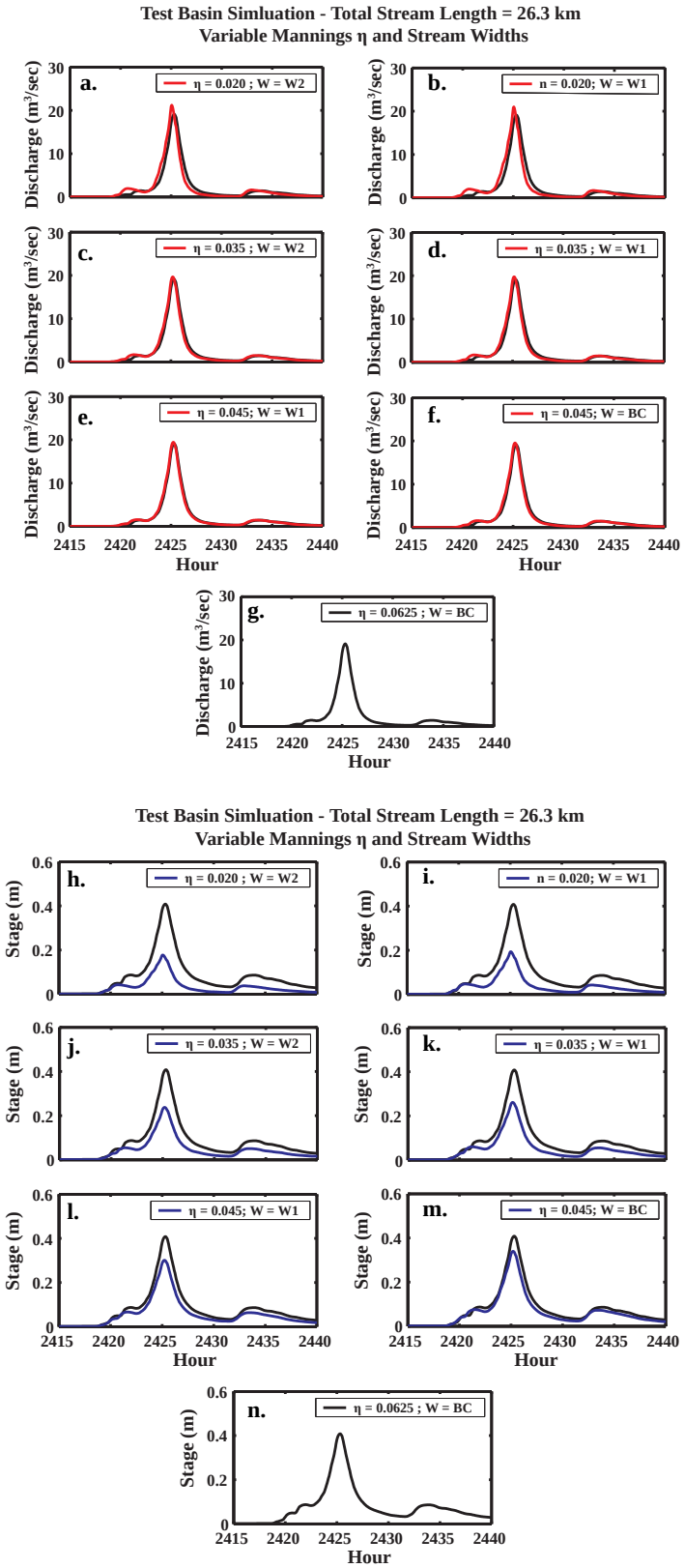

Figure 5.17 Discharge and stage hydrographs for ΣL = 26.3 km, variable Manning's η and geomorphic power law contributing area - stream width relationships

Manning's η value, variation in channel width does not have a substantial impact on the discharge hydrograph.

Figure 5.17h through Figure 5.17k provide the stage hydrographs for the inner floodplain development phase of the arroyo geomorphic sequence. Examination of Figure 5.17h and Figure 5.17j reveal that for a given channel width, stage increases with Manning's η. Similar trends are observed when comparing Figure 5.17i and Figure 5.17k. For constant Manning's η, a decrease in channel width results in a slightly higher stage value, however the increase in stage does not have a substantial impact on the discharge hydrograph.

The final phase of arroyo development considered in this study is channel and inner floodplain stabilization. The establishment of vegetation in riparian areas decreases shear forces on channel sediment and reduces local streamflow velocities. Consequently, vegetation may limit streamflow erosive potential and contribute to sediment deposition as well as channel aggradation (*Simon and Darby*, 1999). *Griffin et al.* (2005) showed that Manning's η increases with stage as flood events interact with riparian vegetation. Thus, Manning's η is allowed to vary from 0.035 to 0.0625 with progressively narrower channel representation in this group of tRIBS model simulations.

Figure 5.17e through 5.17f show the discharge hydrographs for the channel and inner floodplain test basin simulations. As observed previously, hydrographs do not vary for simulations using constant Manning's η across different contributing area-stream width geomorphic relationships (Figure 5.17d and Figure 5.17e). However, inspection of

Figure 5.17l and Figure 5.17m shows that narrowing channel widths result in an increase in stage. Although the stage increases, it is not substantial enough to cause meaningful alteration of the discharge hydrograph.

Figure 5.18 provides summary statistics for simulations #1 through #18 found in Table 5.3. These simulations have a gradually increasing network length as well as increasing channel widths for Manning's η of 0.020 and 0.035. Note, within Figure 5.18, the *x* axis plots increasing stream network length to the right. For multiple stream network width simulations, the narrower network is plotted first followed by the wider representation for that particular channel network length. All statistics are calculated against the standard model run which uses the BC geomorphic power law, Manning's η of 0.0625, and ΣL = 26.3 km.

The Root Mean Square Error (*RMSE*; Figure 5.18a) and Mean Absolute Error (*MAE*; Figure 5.18c) indicate that short channel lengths (ΣL = 4.34 km) possess similar error despite differences in Manning's η. As observed in the suite of La Jara Creek/ Cañon Madera test simulations that utilize a constant geomorphic power law, error associated with shorter channel networks represents the transfer of the dominant tRIBS routing mechanism from the channel to the hillslope.

When channel length is extended to 15.4 km, *MAE* and *RMSE* errors decrease indicating that simulation accuracy improves with respect to the standard model run. Changes in channel width between the N2 and N1 representation do not substantially alter *RMSE* or *MAE* values.

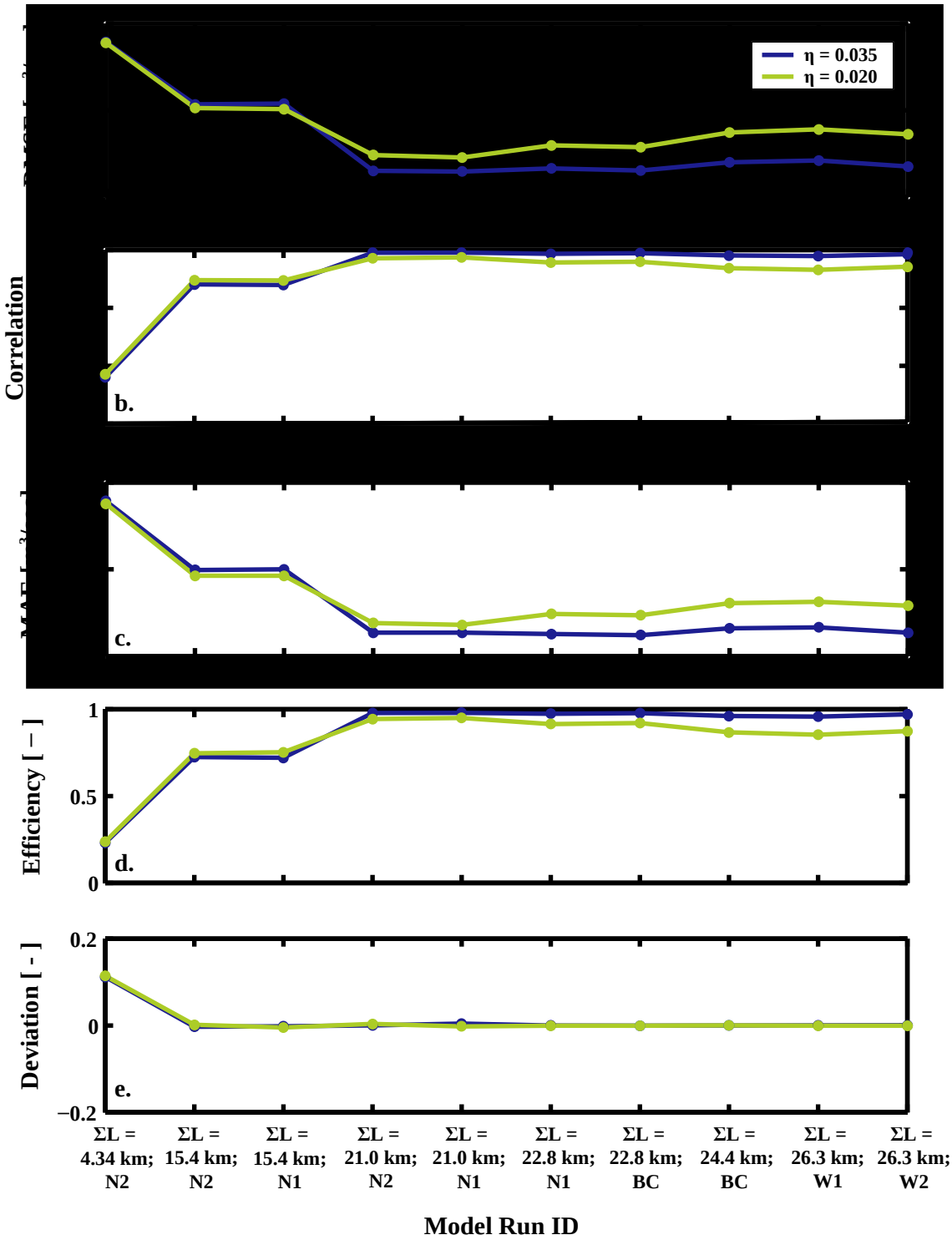

Figure 5.18 Statistical metrics for La Jara Creek/Cañon Madera test watershed using variable total channel lengths (ΣL), contributing area - stream width relationships, and Manning's η of either 0.020 or 0.035

Additional increase in ΣL to 21.0 km further improves simulation performance compared to the standard simulation. At this point, statistical variation across different Manning's η emerges. Specifically, more error is associated with Manning's η of 0.020 than Manning's η of 0.035. Furthermore, simulations using Manning's η of 0.020 and the N1 geomorphic power law exhibit the least amount of error with respect to the standard model for all simulations with Manning's η equal to 0.020. A minimum is achieved because watershed representations with ΣL of 21.0 km possess longer hillslope lengths and runoff travel times in comparison to the standard model simulation. When ΣL is 21.0 km, lower Manning's η of 0.020 increases streamflow velocity, which compensates for the additional time required for runoff to reach a channel node. Differences in model performance across the two different channel width geomorphic power laws for ΣL of 21.0 km and Manning's η of either 0.035 or 0.020 are minimal.

For simulations using a channel length of 22.8 km and Manning's η of 0.035, *MAE* and *RMSE* possess a minimum error value using the BC power law. When compared to the minimum achieved for Manning's η of 0.020, Manning's η of 0.035 requires a longer channel network to reduce hillslope length before increased streamflow velocities can adequately compensate for a shorter stream network. In general, for constant channel slope, stage, and channel width, streamflow velocities are slower when Manning's η is 0.035 as compared to simulations using Manning's η of 0.020

For longer channel networks (ΣL of 24.4 km and 26.3 km) error increases for both values of Manning's η. As the hillslope length decreases, runoff reaches the channel nodes earlier in time and low Manning's η causes swift routing of streamflow through the

channel network. Consequently, simulations with lower Manning's η cannot approximate the standard model run as well as previous simulations that utilized shorter channel networks. Interestingly, simulations for the longest network (26.3 km) have the closest approximation to the standard model run using wider channel widths. The lower *RMSE* and *MAE* values suggests that the reduction in stage associated with a wider channel compensates for a lower Manning's η. Consequently, simulations using W2 better approximate the standard model run for total channel network lengths of 26.3 km.

Efficiency (Figure 5.18d) and Correlation Coefficients (Figure 5.18d) calculations for different simulations are provided but not discussed since they lead to the same conclusions presented immediately above. However, the Deviation statistic again suggests that total streamflow volumes for simulations with ΣL equal to 4.34 km are less than all other model runs.

Figure 5.19 provides the statistical metrics for simulations #17 through #23 in Table 5.3, which correspond to the inner floodplain development as well as the channel and inner floodplain stabilization phases of the modelling sensitivity study. *RMSE* (Figure 5.19a) and *MAE* (Figure 5.19c) show that for ΣL of 26.3 km, model runs with wider networks better approximate the standard model run across all values of Manning's η (0.020, 0.035, and 0.045). As shown in previous simulations, lower Manning's η values introduce faster modelled streamflow velocities in comparison to the standard model run, which uses a Manning's η of 0.0625. Because all simulations shown in Figure 5.19 use the same channel length as the standard model run, average hillslope lengths are also the same. Consequently, tRIBS no longer maintains the compensating

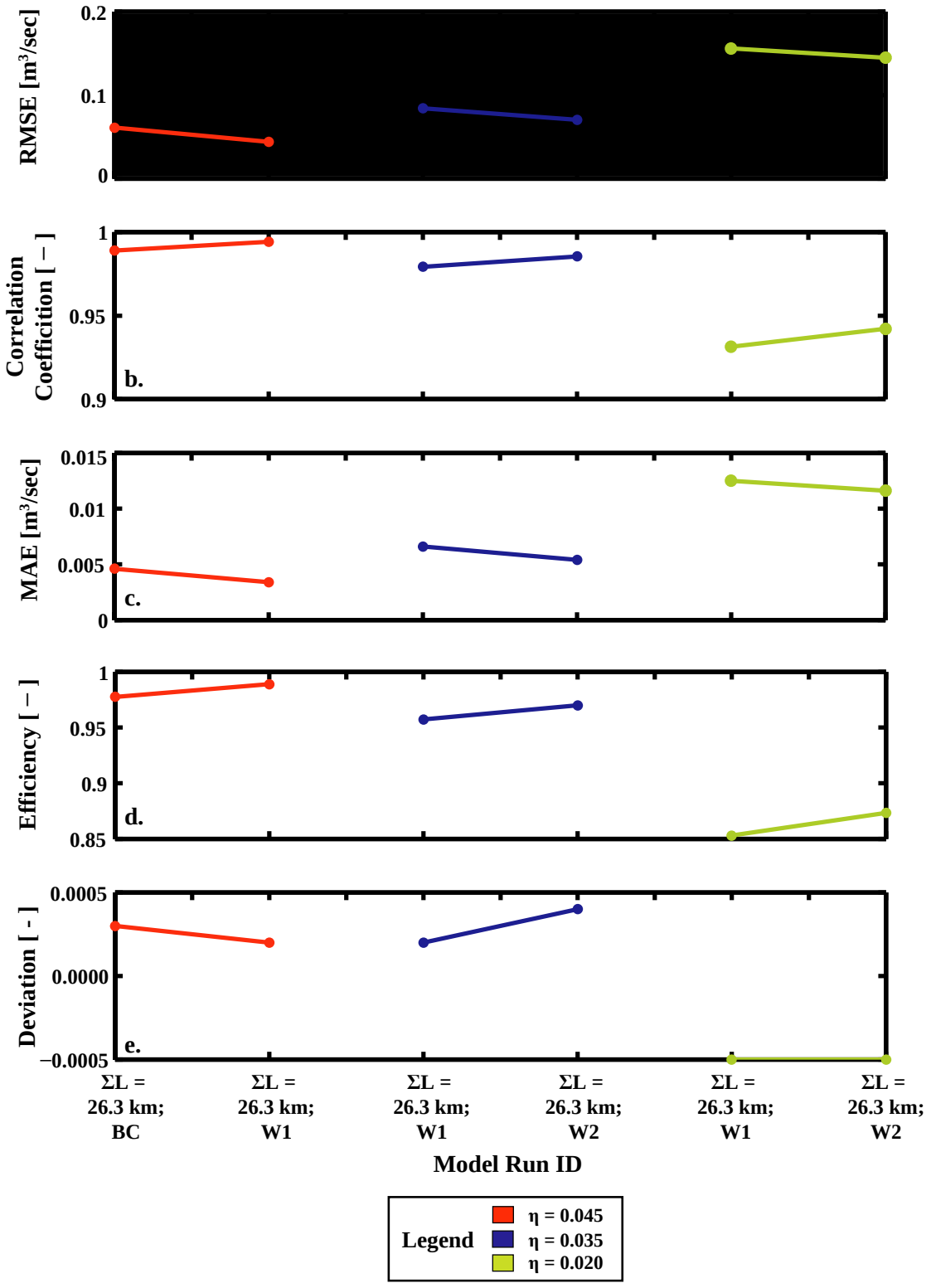

Figure 5.19 Statistical metrics for La Jara Creek/Cañon Madera test watershed using total channel length (ΣL) of 26.3 km, contributing area - stream width relationships, and Manning's η of either 0.020, 0.035, or 0.045

balance between increased streamflow velocity and longer hillslope travel paths observed for simulations with shorter networks and reduced Manning's η. For simulations #17 through #23, the wider stream network length balances decreased Manning's η in Manning's equation and provides a better approximation to the standard model in comparison to simulations with narrower channel width representations.

As before, Correlation Coefficient (Figure 5.19b) and Efficiency (Figure 5.19d) are provided in Figure 5.19 but not discussed since they lead to the same conclusion as interpretations based upon the *RMSE* and *MAE* statistics. The Deviation statistic shows tRIBS streamflow volumes are consistent across this group of simulations.

Overall, simulations designed to reveal differences in watershed response due to arroyo geomorphic change demonstrate total channel length is the major controlling factor on flood generation in semi-arid basins. As the channel progresses upslope, average hillslope length decreases and runoff requires less time to travel from the point of production to the channel network. Furthermore, for longer networks, hillslope runoff tends to arrive at the channel within a narrow period of time. This is reflected in the hydrograph at the watershed outlet where streamflow is concentrated within one large event.

Variation in Manning's η does not create significant differences between model hydrographs. These results agree with previous studies performed in the Río Puerco near Bernardo, NM. In *Griffin et al.* (2005), different representations of vegetation stem size and density along the lower Río Puerco did not have significant effects on model -

calculated discharge. Within the *Griffin et al*. (2005) study, form drag due to woody vegetation is explicitly represented in the streamflow model whereas tRIBS uses an empirical Manning's η parameter that incorporates various types of streamflow resistance. Nonetheless, assuming form drag on woody vegetation is a major component within the Manning's η resistance term, results from *Griffen et al.* (2005) are in agreement with tRIBS results that exhibit marginal discharge sensitivity to variations in Manning's η. Consequently, calibration efforts focused on Manning's η will not substantially alter model timing or peak discharge estimates in smaller watersheds. Calibration of Manning's η should only be used to fine tune the model hydrograph after a reasonable simulated hydrograph is achieved using soil parameter calibration.

Finally, varying channel width using the geomorphic power laws in Figure 5.11 does not significantly influence La Jara Creek/Cañon Madera test basin discharge hydrographs. In contrast, narrower stream channel representation results in a slight increase in stage. However, the increase in stage is not large enough to significantly alter the discharge hydrograph. Thus, discharge remains consistent across different contributing area - stream width power laws.

Results for variation in channel width simulations should only be considered in terms of the model sensitivity study. Because overbank flow is an important component of the arroyo geomorphic cycle, tRIBS may not accurately represent potential streamflow losses associated with watersheds exhibiting narrowing channel widths while maintaining high drainage densities. As observed in this study, high drainage densities capture hillslope runoff and lead to large flood events. However, as channels narrow and the

channel network length is lengthened, the likelihood for overbank flow may increase. Interpretations with respect to streamflow response to different arroyo channel widths are further limited by the narrow range of geomorphic power laws considered within this study. Thus, while tRIBS shows minimal sensitivity to the channel width representations in the La Jara Creek/Cañon Madera test watershed, these results cannot be interpreted in the framework of arroyo channel width evolution.

5.5 Upper Río Puerco Arroyo Development Scenarios: Experimental Design

The following group of simulations apply changes in channel length, channel width, and Manning's η to the Upper Río Puerco. Simulations are designed to approximate later stages of arroyo incision in a large semi-arid watershed. Unlike the La Jara Creek/Cañon Madera test watershed, model setup for each simulation is exactly the same as the calibrated Upper Río Puerco model discussed in Section 4.8.2 except for the specified changes in channel width, channel length, and Manning's η.

Four different total channel lengths are used in the Upper Río Puerco sensitivity study: the calibrated model length based upon orthophotgraphs (ΣL = 1760 km); an 8% reduction in total channel length (ΣL = 1513 km); a 15% reduction in total channel length (ΣL = 1358 km); and a 25% reduction in total channel length (ΣL = 1229 km). Based upon visual inspection of the derived network, a 25% reduction in the total network results in an average shortening of first order stream networks by a few hundred meters but no more than 1 km. These values agree with *Peterson* (1950) who observed a 160 ft increase in channel length in Deadmans Wash near Shiprock, NM from 1944 - 1948 and a

Drainage Network	Constant Area Threshold - DEM Cells (Area)	Total Stream Network Length (ΣL)	Drainage Density
Orthophotograph	314 (0.25 km^2)	1646 km	1.47 km^{-1}
8 Percent Reduction	380 (0.30 km^2)	1513 km	1.35 km^{-1}
15 Percent Reduction	450 (0.35 km^2)	1398 km	1.21 km^{-1}
25 Percent Reduction	600 (0.47 km^2)	1229 km	1.10 km^{-1}

Table 5.5. Upper Río Puerco Drainage Network Representations

200 ft extension of Hogback Wash also near Shiprock, NM from 1936 - 1946. From 1910 to 1948, *Peterson* (1950) estimated Deadmans Wash had extended about 2 miles, while from 1920 to 1946 Hogback Wash elongated roughly 1 mile. Both these drainages lie outside the Río Puerco watershed. Because Peterson's account of arroyo extension postdates the period of major incision in the Río Puerco, it is assumed that arroyo extension slowed by the early 1900s and the major geomorphic change during this period was channel widening. Since actual changes in stream network length for the Upper Río Puerco are unknown, model sensitivity studies conducted here begin in the lateral erosion phase of arroyo development based upon Peterson's observations from northwestern New Mexico.

Individual maps of each new tRIBS Upper Río Puerco stream channel representation does not provide the resolution required to see the changes in lower stream order network length. Thus, the reduction associated with increasing constant area thresholds observed for the 19.3 km^2 test basin in Figure 5.3 is regarded as typical for basins of similar size throughout the Upper Río Puerco. Table 5.5 provides summary statistics for each new stream network delineated for the Upper Río Puerco.

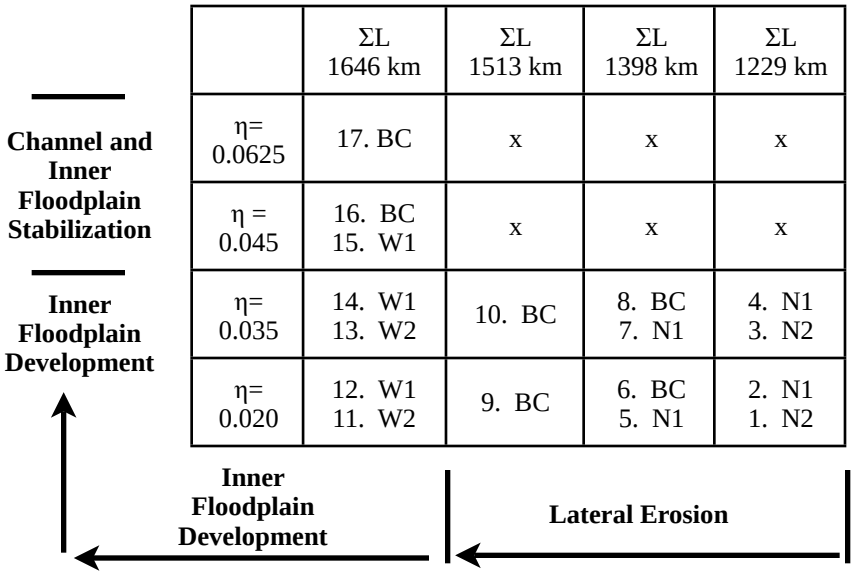

	ΣL 1646 km	ΣL 1513 km	ΣL 1398 km	ΣL 1229 km
η= 0.0625	17. BC	x	x	x
η = 0.045	16. BC 15. W1	x	x	x
η= 0.035	14. W1 13. W2	10. BC	8. BC 7. N1	4. N1 3. N2
η= 0.020	12. W1 11. W2	9. BC	6. BC 5. N1	2. N1 1. N2

Table 5.6 Upper Río Puerco Arroyo Development Scenarios: Variable Manning's η, Stream Network Length (ΣL), and Channel Widths

As in the La Jara Creek/Cañon Madera test watershed, different channel widths are represented using the various geormorphic power laws shown in Figure 5.11. Different Manning's η values of 0.0625, 0.045, 0.035, 0.020 are also used to estimate variation in streamflow response due to different tRIBS parameterizations associated with the arroyo geomorphic sequence. Table 5.6 shows the various model simulations conducted for the Upper Río Puerco. For each stage and hydrograph figure in the following section, the calibrated tRIBS model hydrograph is provided in black. Statistics calculations at the end of section 5.6 are determined based upon the calibrated Upper Río Puerco simulation (Model Run #17 in Table 5.6).

5.6 Upper Río Puerco Arroyo Development Scenarios: Model Results and Discussion

The first set of simulations in the Upper Río Puerco examine changes in the discharge and stage hydrographs for ΣL of 1,229 km with narrow channel widths and

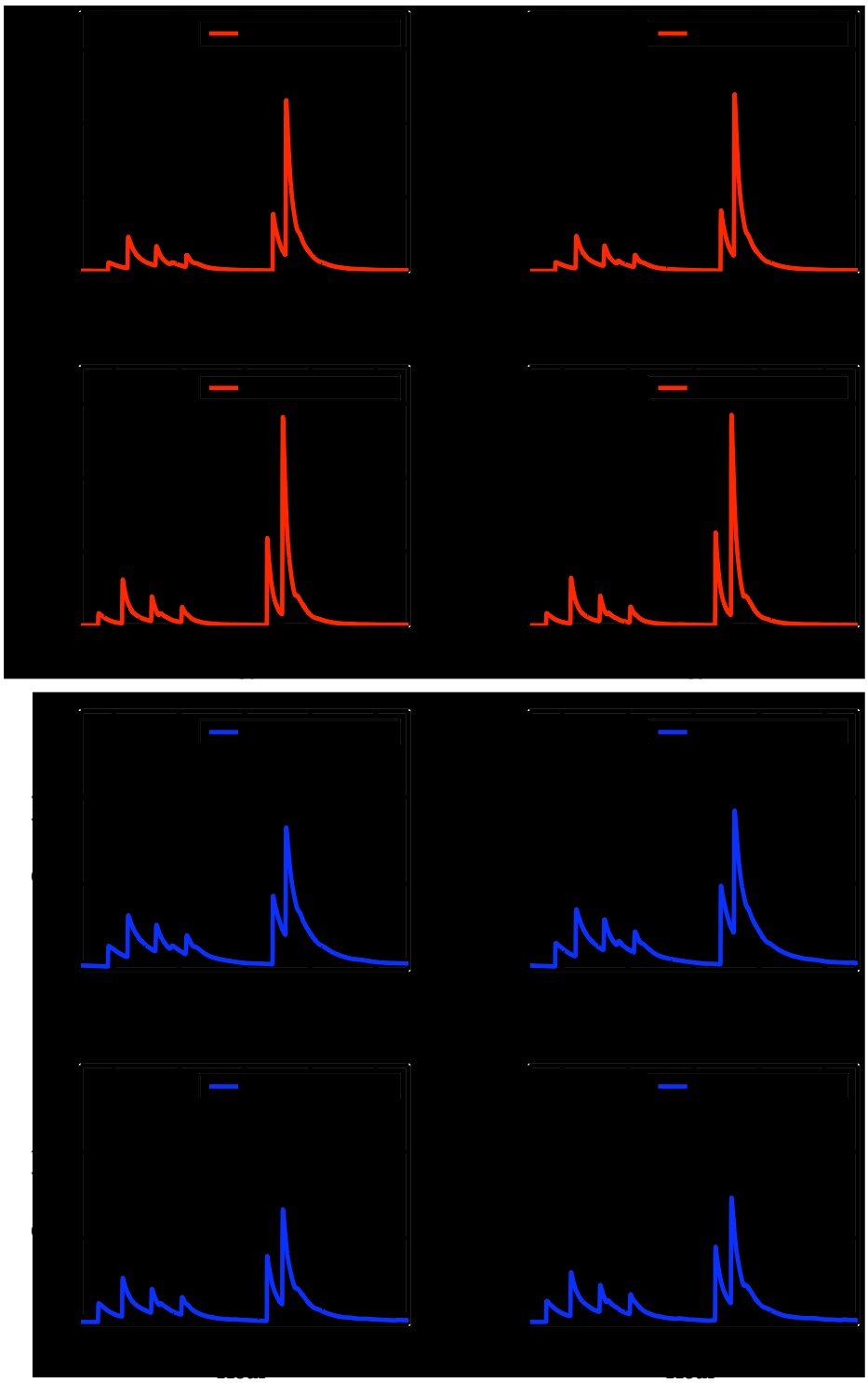

Figure 5.20 Discharge and stage hydrographs for ΣL = 1,229 km, variable Manning's η, and geomorphic power law contributing area - stream width relationships

variable Manning's η. Figure 5.20 shows tRIBS model discharge and stage hydrographs corresponding to simulations #1 through #4 in Table 5.6. Comparisons of discharge hydrographs across constant Manning's η (i.e., Figure 5.20a versus figure 5.20b; Figure 5.20c versus Figure 5.13d) show that narrower channels (N2) lead to slightly higher hydrograph peaks. However, the increase in hydrograph peaks due to contracted channel width is secondary compared to increased discharge peaks associated with decreasing Manning's η (Figure 5.20a compared to Figure 5.20c; Figure 5.20b compared to Figure 5.20d). Furthermore, decreasing Manning's η also results in flood events that occur slightly earlier in time.

Stage hydrographs demonstrate that for a given value of Manning's η, streamflow depth is greater for a narrower channel (i.e., Figure 5.20e versus figure 5.20f; Figure 5.20g versus Figure 5.13h). Increase in stage associated with the N2 power law corresponds to a slight increase in discharge. In contrast, decreasing Manning's η for a specific channel width causes a decrease in stage (i.e. Figure 5.20e versus figure 5.20g; Figure 5.20f versus Figure 5.13h). Although stage decreases, the associated hydrograph peak increases due to the increased channel velocity associated with lower Manning's η.

The next series of simulations use a ΣL value of 1,398 km and apply a slightly wider stream network condition in combination with Manning's η of 0.035 and 0.020. Figure 5.21 demonstrates that despite the increased channel length, changes in the contributing area - stream width power law have little impact on the tRIBS discharge hydrographs for constant Manning's η (i.e., Figure 5.21a versus Figure 5.21b; Figure 5.21c versus Figure 5.21d). The most substantial change in discharge hydrograph occurs

Upper Río Puerco - Total Stream Length = 1,398 km
Variable Mannings η and Stream Widths

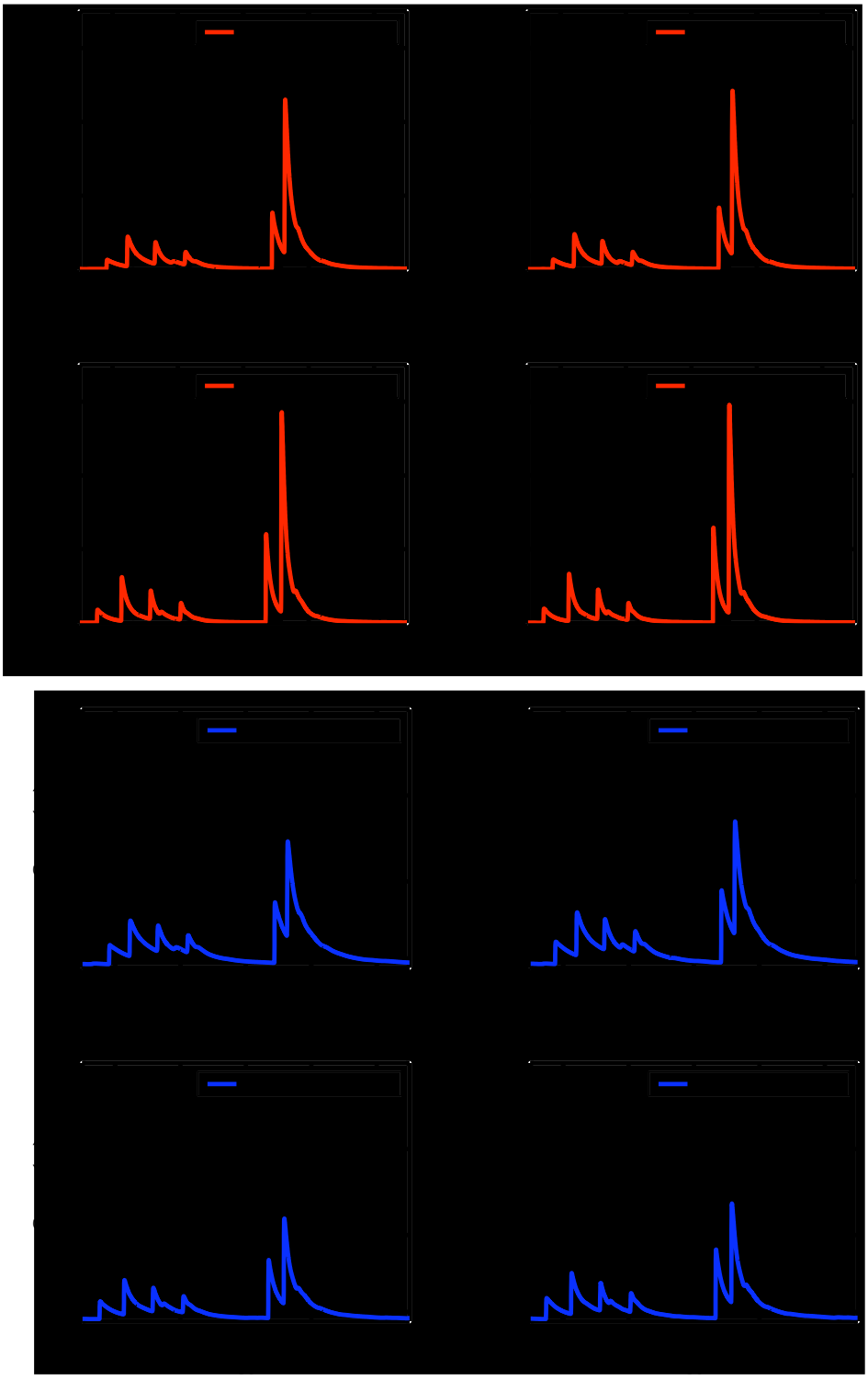

Figure 5.21 Discharge and stage hydrographs for ΣL = 1,398 km, variable Manning's η, and geomorphic power law contributing area - stream width relationships

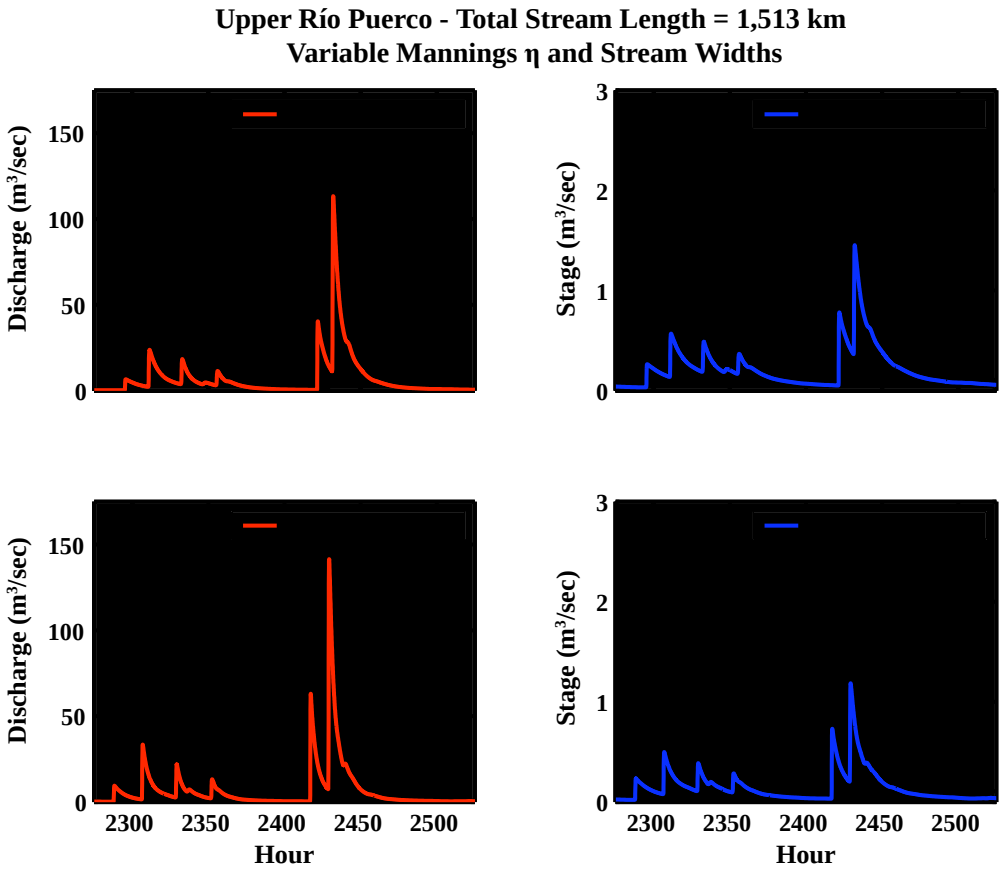

Figure 5.22 Discharge and stage hydrographs for ΣL = 1,513 km, variable Manning's η, and the BC geomorphic power law contributing area - stream width relationship

when Manning's η is decreased from 0.035 to 0.020. As observed previously, lowering Manning's η causes an increase hydrograph peak discharge while stage decreases. The decrease in stage is compensated by an increase in streamflow velocity, which results in the increase in flood magnitude for reduced values of Manning's η. Finally, comparison of the N1 simulations found in Figure 5.20 and Figure 5.21 show that the additional stream network length does not substantially influence discharge or stage hydrographs.

Figure 5.22 shows the stage and discharge hydrographs for ΣL of 1,513 km, the BC geomorphic power law, and Manning's η of 0.020 and 0.035. These two simulations account for the final model runs within the lateral erosion phase of the arroyo geomorphic

sequence. Decrease in Manning's η from 0.035 to 0.020 results in an increase in the discharge hydrograph peak but a decrease in stage. Because channel widths are not varying, the increase in discharge peaks occurs as a result of an increase in streamflow velocity. Additionally, reducing Manning's η results in flood events occurring slightly earlier in time.

Figure 5.23 provides the discharge and stage hydrographs for simulations corresponding to the Upper Río Puerco orthophotograph ΣL values of 1,646 km. Figure 5.23a through Figure 5.23d along with Figure 5.23h through Figure 5.23k represent different scenarios of arroyo development within the inner floodplain development phase. In these cases, increasing Manning's η results in a decrease in the discharge hydrograph peak and a shift in flood events to later periods in time. When Manning's η is 0.035, narrowing of the channel from W2 to W1 results in a slight increase in the hydrograph peak as well as a shift in flood events to earlier periods in time (Figure 5.23c compared to Figure 5.23d).

Inspection of the stage hydrographs shows that increasing Manning's η while holding stream widths constant causes an increase in stage as well as a shift in stage peaks to later periods in time (Figure 5.23h versus Figure 5.23j; Figure 5.23i versus Figure 5.23k). If Manning's η remains constant and smaller channel widths are applied to the drainage network, peak stage values increase and shift to a slightly earlier period in the simulation (i.e. Figure 5.23j compared to Figure 5.23k).

Figure 5.23e through Figure 5.23g provides discharge hydrographs for the

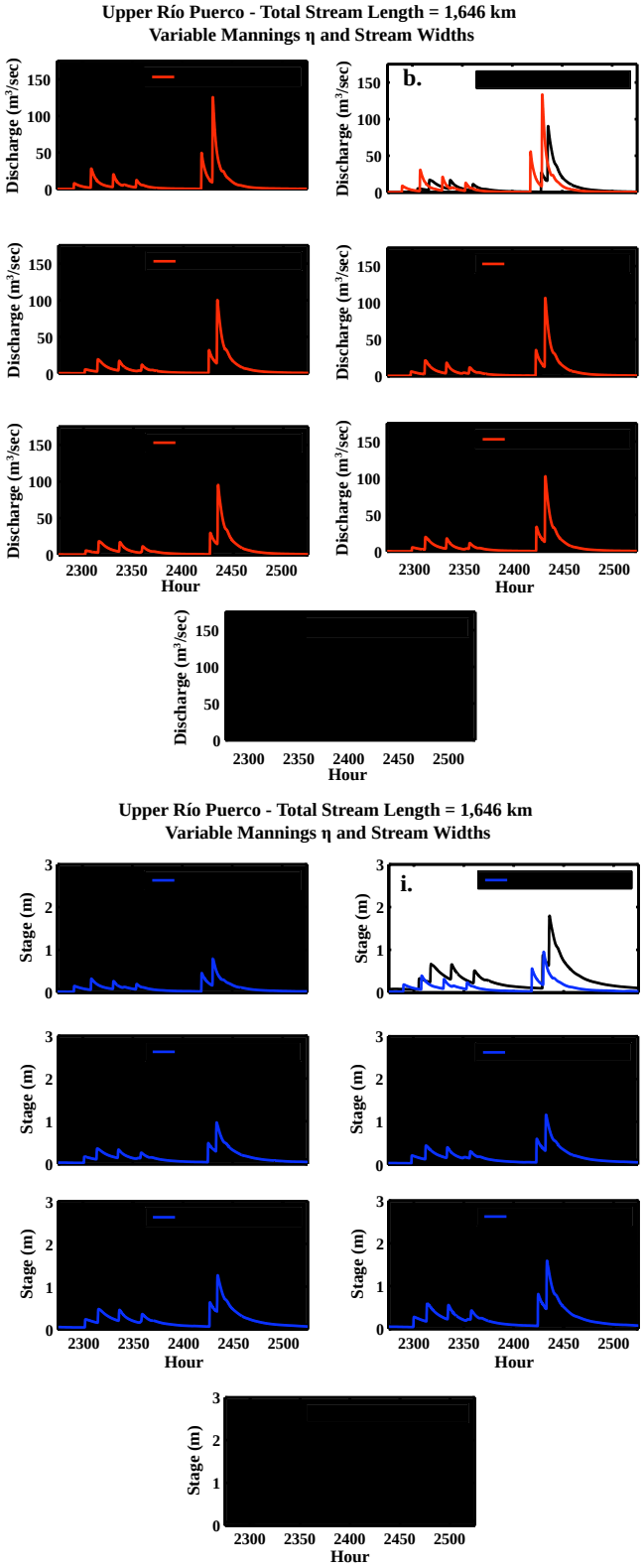

Figure 5.23 Discharge and stage hydrographs for ΣL = 1,646 km, variable Manning's η, and geomorphic power law contributing area - stream width relationships

channel and inner floodplain stabilization stage of arroyo development. Figure 5.23e and Figure 5.23f show the discharge hydrographs for Manning's η of 0.045. The increase in Manning's η from a previous value of 0.035 causes a decrease in the hydrograph peak. Furthermore, comparison of Figure 5.23e and Figure 5.23f shows that decreasing channel width representation from W1 to BC causes an increase discharge peaks. Additionally, channel constriction increases streamflow velocities such that flood waves arrive at the channel outlet earlier in time. Finally, Figure 5.23g shows the flood hydrograph for the calibrated Upper Río Puerco tRIBS model. Increasing Manning's η from 0.045 causes slightly lower hydrograph peaks as well as a small lag in flood pulse arrival time at the watershed outlet.

Figure 5.23l through Figure 5.23n show the stage hydrographs that correspond to the channel and inner floodplain stabilization portion of the arroyo geomorphic sequence. For Manning's n of 0.045, stage increases with narrowing of the channel. The increase in stage corresponds to an increase in the hydrograph peak observed in Figure 5.23f. In addition, channel constriction increases channel velocities such that the flood pulse arrival at the outlet occurs earlier in time as observed in the discharge hydrographs. Figure 5.23n increases Manning's η from 0.045 to 0.065. As a result, streamflow velocities decrease and water accumulates in the channel leading to a slight increase in stage at the watershed outlet.

Figure 5.24 provides the statistical results for simulations #1 through #14 in Table 5.6. This group of simulations correspond to the lateral erosion and inner floodplain development portion of the sensitivity study. Within this subset of model runs, the total

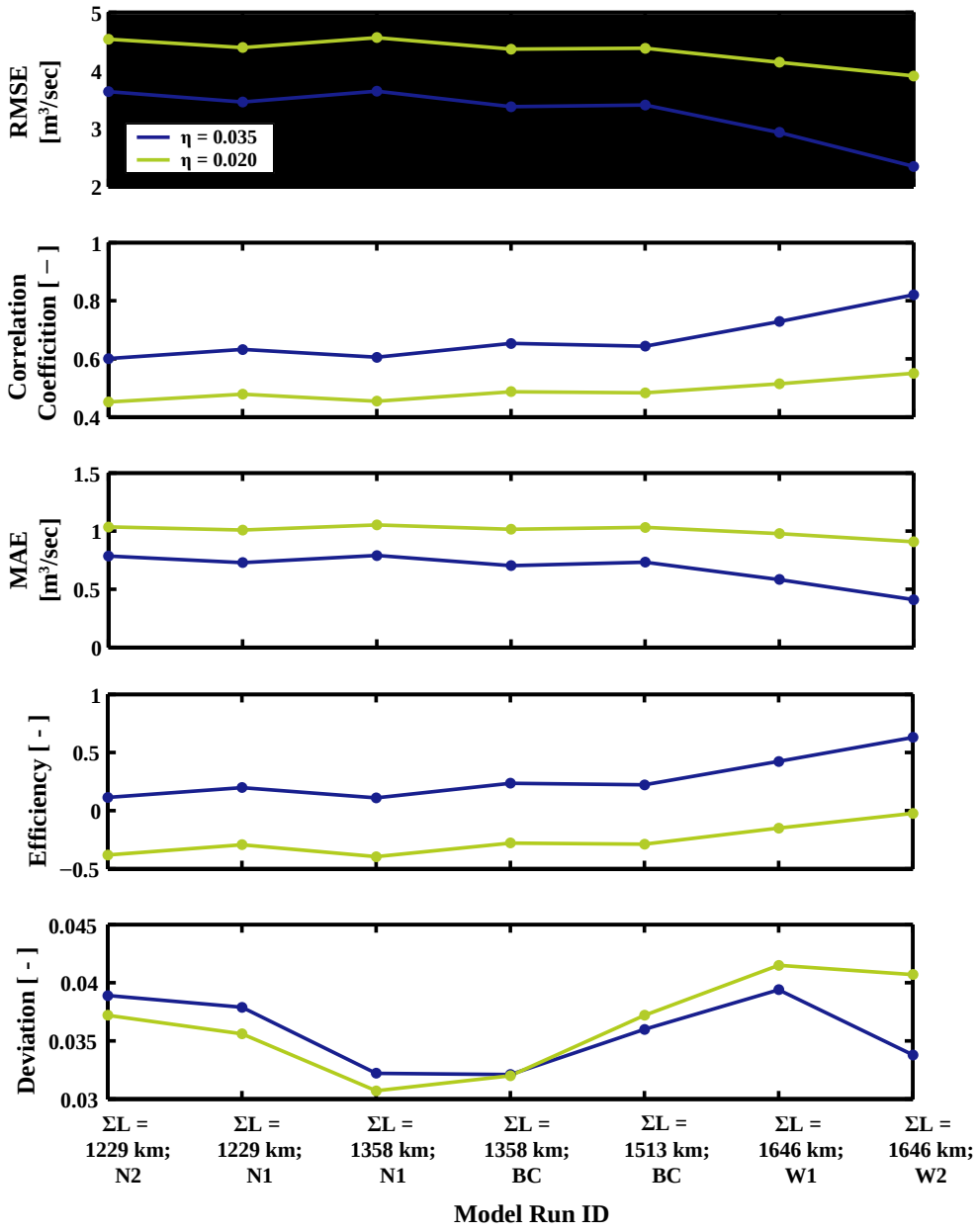

Figure 5.24 Statistical metrics for Upper Río Puerco watershed using variable total channel lengths (ΣL), contributing area - stream width relationships, and Manning's η of either 0.020 or 0.035

channel network length gradually increases along with channel width. Examination of Figure 5.24 shows that as channel network length approaches the calibrated model ΣL of 1646 km, *RMSE* and *MAE* statistics decrease. Comparisons for constant channel length and Manning's η but different contributing area - stream width geomorphic power laws suggest that wider networks better approximate the Upper Río Puerco calibrated model hydrograph. As noted before, shorter network representation in tRIBS has the additional effect of increasing hillslope lengths. Under certain conditions, faster in-channel velocities due to either lower Manning's η or narrower channel representation can compensate for the increase time period required for runoff to reach channel nodes due to the longer hillslope runoff paths. However, for this set of simulations, the channel network is not reduced enough to require the increase of in-channel velocities created by Manning's η of 0.020 or 0.030. Consequently, Manning's η of 0.035 is always a better approximation to the calibrated model than simulations performed with Manning's η of 0.020. In addition, wider channels better approximate the calibrated model within this group of simulations especially for ΣL of 1646 km. Wider channel widths increase stream cross sectional area and decrease flood stage assuming discharge volumes do not significantly change in time across the model duration. The decrease in stage in the numerator of Manning's equation balances the reduced values of Manning's η (i.e., 0.020 or 0.035) and as a result, simulations with wider network widths better approximate the Upper Río Puerco calibrated model hydrograph.

Again, the Efficiency and Correlation Coefficient trends reveal the same information as the *RMSE* and *MAE* statistics. Therefore, *E* and *CC* statistical values are

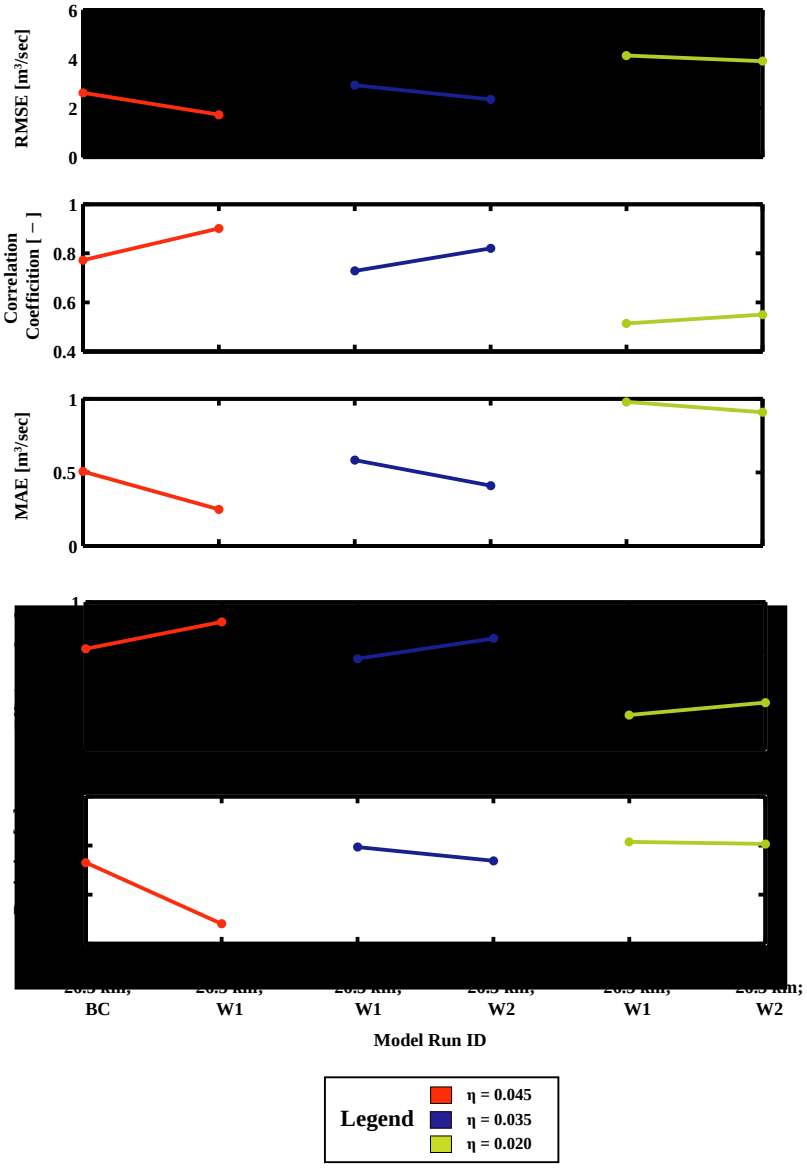

Figure 5.25 Statistical metrics for Upper Río Puerco watershed using total channel length (ΣL) of 26.3 km,contributing area - stream width relationships, and Manning's η of either 0.020, 0.035, or 0.045

provided in Figure 5.24 but are not discussed. Additionally, the Deviation statistic demonstrates flow volumes are comparable across all performed simulations.

Figure 5.25 shows the statistical trends for simulations corresponding to simulations #11 through #17 in Table 5.6. Increasing Manning's η value results in a

better tRIBS approximation to the calibrated simulation as indicated by lower *RMSE* and *MAE* values. In comparison to narrower networks, wider channel widths for a given Manning's η also improves hydrograph approximation to the Upper Río Puerco calibrated model. As discussed previously, for constant channel length and Manning's η, wider channels distribute flow volumes across a larger channel cross sectional area. This causes a reduction in stream stage. Since stage appears in the numerator of Manning's equation, decreasing stage mitigates the effects of lower Manning's η in the equation denominator. Consequently, for constant Manning's η and ΣL of 26.3 km, wider channel widths provide a better approximation to the tRIBS calibrated hydrograph than narrower stream widths. Correlation Coefficient and Efficiency statistics demonstrate similar results as *RMSE* and *MAE* statistics. The Deviation statistic shows cumulative streamflow volumes across all simulations remain similar.

tRIBS model sensitivities within this section should viewed cautiously in the context of arroyo geomorphic change. Poor model replication of the Upper Río Puerco USGS hydrograph following model calibration suggests that the rainfall-runoff transformation process is not accurately replicated by the current watershed representation in the tRIBS model. As mentioned previously, this could be due to a combination of problems including poor calibration, omission of semi-arid hydrologic processes within the model, or inappropriate NEXRAD temporal resolution used to force the model. Nonetheless, this series of model runs using different stream network representations can aid future studies in model parameterization efforts.

Because model simulations within this section began with an already long

network length, additional network extension did not significantly effect discharge timing or magnitudes, However, tRIBS watershed representations with longer stream networks appear to possess greater sensitivity to changes in channel width and Manning's η when compared to simulations performed for the smaller La Jara Creek/Cañon Madera test watershed. For longer networks, smaller values of Manning's η forces modelled streamflow events to earlier time steps. Furthermore, a decrease in Manning's η can also lead to considerable increases in the hydrograph peak.

Decrease in channel width also tends to result in a slight increase in maximum discharge values. Additionally, smaller channel widths move streamflow events to earlier time steps. For the simulations performed, when Manning's η decreases and channel width increase for a given network length (i.e., Figure 5.23), simulated discharge moves to an earlier time step and peak flow increases suggesting model sensitivity to changes in Manning's η are more significant than changes in network width.

Furthermore, the overall shape of the hydrograph is not significantly altered by changes in channel length, Manning's η, or stream network width for simulations using the entire Upper Río Puerco. This suggests that soil parameterization is likely the primary control on tRIBS simulated flood events and model sensitivity to channel network representations can only be used to effect small changes on the modelled response. Consequently, alternative channel network representations or geomorphic power laws will only slightly improve model calibration. If stream network density and channel widths are considered reasonable for a particular watershed and tRIBS still possesses difficulty replicating stream gauge data, more effort should be placed on soil

parameter calibration. Likewise, Manning's η should not be viewed as a parameter that will substantially alter the hydrograph shape. Variation of Manning's η within reasonable parameter values will only cause moderate shifts in timing and peak discharge and will not change the overall shape of the tRIBS hydrograph.

CHAPTER 6 - CONCLUSIONS AND FUTURE WORK

6.1 Conclusions: Model Calibration for Monsoon Events 2003

Results from the Upper Río Puerco model calibration exercise demonstrate that for the parameter values used in this study, tRIBS reproduces flood sequences and watershed lag times observed in the USGS discharge hydrograph during September 2003. Instances of delayed model response are relatively small when compared to the time periods required for watershed flood generation and wave propagation following the monsoon rainfall events considered within this study. While tRIBS was able to replicate flood event order and reasonable lag times, simulated events contain discrepancies for flow event volumes, peak discharge, and peak timing. In addition, tRIBS also produces extended hydrograph recession limbs that are not observed in the USGS discharge dataset. Results suggest that model physics, model parameter values, or data sources used to force the tRIBS model can be improved.

The placement of interior hydrograph nodes reveals minimal streamflow generation in the southern portion of the watershed. Estimates of flood contributions based upon hydrographs from internal watershed locations can focus parameter calibration efforts on regions of the watershed critical to runoff production and lead to improved model results. Streamflow estimates upstream of the watershed outlet indicate

that the majority of runoff produced in the Upper Río Puerco during the simulation period occurred in the Señorito, San Pablo, and San Miguel Canyons subwatershed and the Arroyo San Jose subbasin. Runoff production is primarily a function of the spatial distribution and rainfall intensities present in the NEXRAD dataset as well as soil parameterizations that generate runoff predominantly through the infiltration excess mechanism. Furthermore, the lack of tributary streamflow production close to the watershed outlet suggests the likelihood for discharge transmission losses through the channel streambed as flood waves travel through the main stem of the Upper Río Puerco.

6.2 Conclusions: Arroyo Development Numerical Experiments

Numerical experiments designed to replicate a conceptual hypothesis of arroyo development demonstrate that channel extension associated with network incision increases flood magnitude and decreases time to peak. As arroyo headcuts migrate upslope, the distance from the hillslope to the channel decreases leading to quick runoff arrival at the stream network. Once in the network, the longer channels efficiently route water through the watershed to the basin outlet.

Model simulations also revealed that lower Manning's η leads to a slight increase in peak discharge magnitude as well as a small decrease in time to peak. However, model sensitivity to channel roughness is limited for the network representations, basin scales, and flood events explored within this work. Although sensitivity to Manning's η was minimal, various combinations of total channel network lengths and roughness coefficients produced similar results despite different model scenarios.

Simulations designed to approximate arroyo development scenarios also demonstrated minor sensitivities to the different contributing area - channel network width representations used within this study. The lack of model sensitivity is likely due to either tRIBS model physics that do not currently allow overbank flow (all discharge is contained within channel walls) or the limited range of geomorphic power law parameters (exponent and coefficient) tested in this study.

In summary two major conclusions may be drawn from this study. First, tRIBS exhibits the greatest model sensitivity to alterations in total channel length followed by changes in channel roughness and channel width, respectively. Second, with respect to semi-arid environments, the effect of arroyo development is to amplify flood events primarily through the dissection of the landscape with secondary contributions from changes in channel roughness or width.

6.3 Future Work

To expedite the model calibration process, a parameter optimization routine is needed for future tRIBS watershed modelling studies. An optimization routine would more evenly sample the parameter space and limit the time invested on model calibration efforts. For the current version of tRIBS, comprehensively investigating the multitude of parameter value combinations through a manual approach is difficult. Even for basin representations containing only a few soil texture and land cover classes, the number of different parameter combinations is high and only a limited number of parameters and potential values are typically investigated.

Although a parameter optimization routine is needed, it may not ensure improved model results if significant hydrological processes are not represented accurately (or at all) within the model. Important semi-arid physical processes that are currently absent within the tRIBS model include: (1) hillslope runoff reinfiltration (runon); (2) discharge attenuation through streambed transmission losses; (3) and overbank flow. However, adding model components is not sufficient to ensure accurate model representation of hydrological processes in semi-arid environments. Parameter uncertainty increases as model components are added so it is essential to minimize the range of potential values through field-based measurements.

An iterative processes should be conducted that combines field work with model calibration and additional model development. Field work provides the opportunity to ensure that widely available spatial maps (i.e., land cover and soils) accurately describe the watershed of study. In addition, field-based parameter measurements also constrain the parameter space sampled within the optimization routine and improve a researcher's conceptual model of important hydrological processes within the watershed of interest.

Finally, future tRIBS applications should focus on smaller watersheds in comparison to the Upper Río Puerco. Watersheds with less area provide an opportunity to map soil texture and vegetation distributions and obtain field measured parameter values at higher spatial resolutions. In addition, higher temporal and spatial resolution precipitation forcing may be required for improving hydrologic simulations in the southwestern United States due to properties of convective monsoon thunderstorms. Smaller watersheds would also reduce data storage requirements and model simulation

times when using higher resolution NEXRAD radar products. Improved watershed characterization within the model setup phase can provide further confidence in model accuracy, especially if simulation results improve as additional hydrologic processes are represented within tRIBS model physics.

REFERENCES

Adams, D.K., and A.C. Comrie. 1997. The North American Monsoon. *Bulletin of the American Meteorological Society,* 78(10), 2197-2213.

Anderson, O. J., and Jones, G. E. 1994. *Geologic Map of New Mexico*: New Mexico Bureau of Mines and Mineral Resources, Open-file Report 408-A. Digitally available http:/rgis.unm.edu.

Assouline, S., J.S. Selker, and J.Y. Parlange. 2007. A simple accurate method to predict time of ponding under variable intensity rainfall. *Water Resources Research,* 43, doi: 10.1029/2006WR005183.

Antevs, E. 1952. Arroyo Cutting and Filling. *Journal of Geology*, 60, 375-385.

Bailey, R.W. 1935. Epicycles of erosion in the valleys of the Colorado Plateau. *Journal of Geology*, 43, 337-355.

Betancourt, J.L., 1980, Historical overview of the lower Rio Puerco and Rio Salado, central New Mexico: in Wimberly, M. and Eidenbach, P. (eds), *Reconnaissance study of the archeological and related resources of the lower Puerco and Salado drainages*: Albuquerque, U.S. Army Corps of Engineers, p. 23-58.

Beven, K.J. 1984. Infiltration into a class of vertically non-uniform soils. *Hydrology Science Journal, 29*, 425-434.

Beven, K.J. 1989. Changing Ideas in hydrology - The case of physically-based models, *Journal of Hydrology*, 105, 157 - 172.

Beven, K.J. 2001. How far can we go in distributed hydrological modelling? *Hydrology and Earth Systems Sciences*, 5(1), 1 - 12.

Beven, K.J. 2002. Runoff Generation in Semi-arid Areas. In: L.J. Bull and M.J. Kirkby (Eds.), *Dryland Rivers: Hydrology and Geomorphology of Semi-arid Channels*, John Wiley and Sons: New York, 57- 105.

Beven, K.J. 2006. A manifesto for the equifinality thesis. *Journal of Hydrology*, 320 (1-2), 18-36.

Bogaart, P.W. and P.A. Troch. 2006. Curvature distribution within hillslopes and catchments and its effect on they hydrological response. *Hydrology and Earth System Sciences,* 10(3), 925 - 936.

Branson, F.A. and A. Janicki. 1986. *Botanic and Hydrologic Changes on Rangelands of the Rio Puerco Basin, New Mexico*. United States Geological Survey Water-Resources Investigation Report, 86-4021.

Bras, R.L. 1990. *Hydrology: An Introduction to Hydrologic Science*. Addison-Wesley-Longman, Reading: Massachusetts 643 pp.

Brenner, I.S. 1974. A Surge of Maritime Tropical Air - Gulf of California to the Southwestern United States. *Monthly Weather Review,* 102, 375-389.

Brooks, R.H. and A.T. Corey. 1964. *Hydraulic properties of porous media*. Hydrology Paper 3, Colorado State Universtiy, Fort Collins.

Bryan, K. 1925. Date of Channel Trenching (Arroyo Cutting) in the Arid Southwest. *Science*, 62(1607), 338-344.

Bryan, K. 1928. Historic Evidence on Changes in the Channel of Rio Puerco, A Tributary of the Rio grand in New Mexico. *Journal of Geology*, 36, 265-282.

Bryan, K. and F.T. McCann. 1936. Successive Pediments and Terraces of the Upper Rio Puerco in New Mexico. *The Journal of Geology*, 44(2), 145-172.

Bull, L.J. and M.J. Kirkby. 2002. Channel Heads and Channel Extension. In: L.J. Bull and M.J. Kirkby (Eds.), *Dryland Rivers: Hydrology and Geomorphology of Semi-arid Channels*, John Wiley and Sons: New York, 263-296.

Bull, W.B. 1979. Threshold of critical power in streams. *Geological Society of America Bulletin*, 90, 453-464.

Bull, W.B. 1997. Discontinuous Ephemeral Streams. *Geomorphology*, 19, 227-276.

Cabral, M.C., L. Garrote, R.L. Bras, and D. Entekhabi. 1992. A kinematic model of infiltration and runoff generation in layered and sloped soils. *Advances in Water Resources*, 15, 311-324.

Childs, E.C. and M. Bybordi. 1969. The vertical movement of water in stratified porous material: 1. Infiltration, *Water Resources Research*, 5, 446-459.

Cooke, R.U, and R.W. Reeves. 1976. *Arroyos and environmental change in the American Southwest*. Clarendon Press, Oxford, 213 pp.

Coppus, R. and A.C. Imeson. 2002. Extreme Events Controlling Erosion and Sediment Transport in a Semi-Arid Sub-Andean Valley. *Earth Surface Processes and Landforms,* 27, 1365-1375.

Deardorff, J.W. 1978. Efficient prediction of ground surface temperature and moisture with inclusion of a layer of vegetation. *Journal of Geophysical Research*, 82, 1889-1903.

Dellenbaugh, F.S. 1912. Cross-cutting and retrograding of streambeds. *Science*, 47, 450-452.

Dingman, S.L. 2002. *Physical Hydrology*. Prentice Hall: Upper Saddle River, New Jersey, 646p.

Douglas, M.W., R.A. Maddox, and K. Howard. 1993. The Mexican Monsoon. *Journal of Climate*, 6(8), 1665-1677.

Douglas, M.W. 1995. The Summertime Low-Level Jet over the Gulf of California. *Monthly Weather Review,* 123, 2334-2347.

Douglas, M.W. 1998. Diurnal Variation and Horizontal Extent of the Low-Level Jet over the Northern Gulf of California. *Monthly Weather Review*, 126(7), 2017 - 2025.

Downer, C.W., F.L. Ogden, W.D. Martin, and R.S. Hannon. Theory, 2002. Development, and Applicability of the Surface Water Hydrologic Model *CASC2D*. *Hydrological Processes*, 16(2), 255 - 275.

Duce, J.T. 1918. The effect of cattle on the erosion of canyon bottoms. *Science*, 47, 450-452.

Ebel, B.A. and K. Loague. 2006. Physics-based hydrologic-response simulation: Seeing though the fog of equifinality. *Hyrological Processes*, 20, 2887 - 2900.

Ellis, L.A. 2004. *The Morphological Representation of Channel-Forming Flow in Arroyos*. Ph. D. Dissertation, University of Nottingham, 294 pp.

Elliott, J.G. 1979. *Evolution of Large Arroyos The Rio Puerco of New Mexico*. M.S. Thesis, Colorado State University, 106 pp.

Elliott, J.G., A.C. Gellis, and S.B. Aby. 1999. *Evolution of Arroyos: Incised Channels of the Southwestern United States*. In: Darby, S.E. and A. Simon (Eds.), *Incised River Channels*, John Wiley and Sons: New York, 19-33.

Eltahir, E.A.B and R.L. Bras. 1993. A description of rainfall interception over large areas. *Journal of Climate*, 6, 1002-1008.

Environmental Research Systems Institute (ESRI). 1983-2002. Arc 8.3

Fawcett, P.J, J.R. Stalker, and D.S. Gutzler. 2002. Multistage moisture transport into the interior of northern Mexico during the North American summer monsoon, *Geophysical Research. Letters*, 29(23) 2094, doi:10.1029/2002GL015693.

Formento-Trigilio, M.L. and F.J. Pazzaglia. 1998. Tectonic Geomorphology of the Sierra Nacimiento: Traditional and New Techniques in Assessing Long-Term Landscape Evolution in the Southern Rocky Mountains. *The Journal of Geology*, 106, 433-453.

Francis, R.E. 1986. *Phyto-Edaphic Communities of the Upper Rio Puerco Watershed*, New Mexico, USDA Rocky Mountain Forest and Range Experiment Station Fort Collins, CO., 72 pp.

Freeze, R.A. and R. L. Harlan. 1969. Blueprint for a physically-based digitally-simulated hydrologic response model. *Journal of Hydrology*, 9, 237 - 258.

Garotte, L. and R.L. Bras. 1995. A distributed model for real-time flood forecasting using digital elevation models. *Journal of Hydrology*, 167, 279-306.

Gellis, A.C. 1998. History of Streamflow and Suspended-Sediment Collection in the Rio Puerco Basin, New Mexico. In: Harrison, J.B.J. (Ed.), *Soil, Water, and Earthquakes around Socorro, New Mexico*, Rocky Mountain Cell, Friends of the Pleistocene Field Trip Guidebook, 14.

Goodrich, D.C., D.A. Woolhiser, and T.O. Keefer. 1991. Kinematic routing using finite elements on a triangular irregular network. *Water Resources Research*, 27(6), 995-1003.

Goodrich, D.C., L.J. Lane, R.M. Shillito, and S.N. Miller. 1997. Linearity of basin response as a function of scale in a semiarid watershed. *Water Resources Research*, 33 (12), 2951-2965.

Gochis, D.J., L. Brito-Castillo, and W.J. Shuttleworth. 2006. Hydroclimatology of the North American Monsoon Region in Northwest Mexico. *Journal of Hydrology*, 316, 53-70.

Goodrich, D.C., D.A. Woolhiser, and T.O. Keefer. 1991. Kinematic Routing Using Finite Elements on a Triangular Irregular Network. *Water Resources Research,* 27(6), 995-1003.

Gorbach, C.D., D. Love, S. Piper, R. Davis, and A. Cross. 1996. *Río Puerco sedimentation and water quality study: Preliminary findings report*, Bureau of Reclamation, United States Department of the Interior, Washington, D.C., 40 pp.

Grayson, R.B. Moore I.D., and T.A. McMahon, 1992a. Physically based hydrologic modelling: I. A terrain based model for investigative purposes. *Water Resources Research*, 26(10): 2639-2658.

Grayson R.B., I.D. Moore, and T.A. McMahon. 1992b. Physically Based Hydrologic Modeling 2. Is the Concept Realistic? *Water Resources Research,* 26(10), 2659 - 2666.

Griffin, E.R., J.W. Kean, K.R. Vincent, J.D. Smith, and J.M. Friedman. 2005. Modeling effects of bank friction and woody bank vegetation on channel flow and boundary shear stress in the Rio Puerco, New Mexico. *Journal of Geophysical Research*, 110, F04023, 10.1029/2005JF000322.

Hales, J.E., Jr. 1972. Surges of Maritime Tropical Air Northward Over the Gulf of California. *Monthly Weather Review*, 100(4), 298-306.

Heath, D.L. 1983 Flood and Recharge Relationships of the Lower Rio Puerco, New Mexico. *New Mexico Geological Society Guidebook,* 34th Field Conference, 329-337.

Hillel, D. 1998. *Environmental Soil Physics*. Academic Press: San Diego, California, 771 pp.

Hooke, J.M. and J.M. Mant. 2000. Geomorphological impacts of a flood event on ephemral channels in SE Spain. *Geomorphology*, 34, 163-180.

Huntington, E. 1914. The climatic factor as illustrated in arid America. *Carnegie Institute Washington*, Publication 192, 341 pp.

Ivanov, Y.V. 2002. *A Continuous Real-Time Interactive Basin Simulator*. M.S. Thesis, Massachusetts Institute of Technology, 158 pp.

Ivanov, Y.V., E.R. Vivoni, R.L. Bras, and D. Entekhabi. 2004a. Catchment hydrologic response with a fully distributed triangulated irregular network model. *Water Resources Research*, W11102, doi:10.1029/2004WR003218.

Ivanov, V.Y., Vivoni E.R., Bras, R.L. and Entekhabi, D. 2004b. Preserving high-resolution surface and rainfall data in operational-scale basin hydrology: A fully-distributed pysically-based approach. *Journal of Hydrology*, 298(1-4): 80-111.

Jakeman, A.J. and G.M. Hornberger. 1993. How much complexity is warranted in a rainfall-runoff model? *Water Resources Research*, 29(8), 2637-2650.

Kienzle, S. 2004. The Effect of DEM Raster Resolution on First Order, Second Order and Compound Terrain Derivatives. *Transactions in GIS,* 8(1), 83-111.

Kumler, M.P. 1994. An Intensive Comparison Of Triangulated Irregular Networks (TINs) and Digital Elevation Models (DEMs). *Cartographica 31(2),* Monograph 45, 1-48.

Lee, J. 1991. Comparison of existing methods for building triangular irregular network models of terrain from grid digital elevation models. *International Journal of Geographical Information Systems,* 5(3), 267-285.

Legates, D.R. and G.J. McCabe. 1999. Evaluating the use of "goodness of fit" measures in hydrologic and hydroclimatic model validation. *Water Resources Research*, 35, 233-241.

Leopold, L.B. 1951a, Vegetation of Southwestern Watersheds in the Nineteenth Century, *Geographical Review,* 41(2), p.295-316.

Leopold, L.B. 1951b. Rainfall Frequency and Climatic Variation. *Transactions, American Geophysical Union,* 32(3), 347-357.

Liston, G.E. and K. Elder. 2006. A Distributed Snow-Evolution Modeling System (SnowModel). *Journal of Hydrometeorology, 7(6),* 1259 - 1276.

Little, J. J. and P. Shi. 2001. Structural Lines, TINs, and DEMs. *Algorithmica, 30,* 243-263.

Loague, K. and J.E. Vanderkwaak. 2004. Physics-based hydrologic response simulation: platinum bride, 1958 Edsel, or useful tool. *Hydrological Processes,* 18, 2949 - 2956.

Love, D.W. 1997. Implications for Models of Arroyo Entrenchment and Distribution of Archaeological Sites in the Middle Rio Puerco. In: Duran, M.S. and D.T. Kirkpatrick (Eds.), *Layers of Time: Papers in Honour of Robert H Weber,* Archaeological Society of New Mexico, 69-84.

Love, D.W. and S.D. Connell. 2005. Late Neogene Drainage Developments on the Southeastern Colorado Plateau, New Mexico. In: Lucas, S.G., G.S. Morgan, and K.E. Zeigler (Eds.), *New Mexico's Ice Ages,* New Mexico Museum of Natural History and Science Bulletin, No. 28, 151-169.

Love, D.W. and Young, J.D. 1983. Progress Report on the Late Cenozoic Geolgoic Evolution of the Lower Rio Puerco: *New Mexico Geological Society Guidebook*, 34th Field Conference (Socorro Region II), 277-284

Michaud J., and S. Sorooshian. 1994. Comparison of simple versus complex distributed runoff models on a midsize semiarid watershed. *Water Resources Research*, 30(3), 593-605.190190

Molnár, P. 2001. *Precipitation and Erosion Dynamics in the Río Puerco Basin*. PhD Dissertation, Colorado State University, Fort Collins, Colorado. 258 pp.

Molnár, P. and J.A. Ramirez. 2001. Recent trends in precipitation and streamflow in the Río Puerco basin. *Journal of Climate*, 14, 2317 - 2328.

Monteith, J.L. 1965. Evaporation and environment. *Symposium Society for Experimental Biology*, 19, 205-234.

Nelson, E.J., N.L. Jones, and R.J. Barrett. 1999. Adaptive Tessellation Method for Creating Tins from GIS Data. *Journal of Hydrologic Engineering*, 4(1), 2 - 9.

New Mexico Geographic Information System Program (RGIS). 2007. http//rgis.unm.edu

Nordin, C.F. 1963. A preliminary study of sediment transport parameters, Rio Puerco near Bernardo, New Mexico. *United States Geological Survey Profession Paper*, 462-C. 21 pp.

Penman, H.L. 1948. Natural evaporation from open water, bare soil and grass. *Proceedings of the Royal Societ of London*, A193, 120-145.

Peterson, H.V. 1950. The Problem of Gullying in Western Valleys. In: P.D. Trask (Ed.) *Applied Sedimentation*: New York, John Wiley & Sons, 707 pp.

Rawls, W.J., D.L. Brakensiek, and K.E. Saxton, 1982. Estimation of soil water properties. *Transactions of the American Society of Agricultural Engineers*, 25, 1316-1330.

Rawls, W.J., D.L. Brakensiek, and N. Miller. 1983. Green-Ampt infiltration parameters from soils data. *Journal of Hydraulic Engineering*, 109, 62 - 70.

Refsgaard, J.C., S.M. Seth, J.C. Bathurst, M. Erlich, B. Storm, G.H. Jørgensen, and S. Chandra. 1992. Application of the SHE to Catchments in India Part 1. General Results. *Journal of Hydrology*, 140, 1 - 23.

Reggiani, P. and J. Schellekens. 2003. Modelling of hydrological responses: the representative elementary watershed approach as an alternative blueprint for watershed modelling. *Hydrological Processes*, 17, 3785 - 3789.

Rich, J. L. 1911. Recent Stream Trenching in the Semi-arid Portion of Southwestern New Mexico, a Result of Removal of Vegetation Cover. *American Journal of Science*, 32(190), 237-245.

Rutter, A.J., K.A. Kershaw, P.C. Robbins, and A.J. Morton. 1971. A predictive model of rainfall interception in forests: 1. Derivation of the model from observation in a plantation of Corsican. *Agricultural Meteorology*, 9, 367-384.

Rutter, A.J., A.J. Morton, and P.C. Robins. 1975. A predictive model of interception in forests. 2. Generalization of the model and comparison with observations in some coniferous and hardwood stands. *Journal of Applied Ecology*, 12, 367-380.

Schumm, S.A. 1999. Causes and Controls of Channel Incision. In: Darby, S.E. and A. Simon (Eds.), *Incised River Channels*, John Wiley and Sons: New York, 19-33.

Schumm, S.A. and R.F. Hadley, 1957. Arroyos and the Semiarid Cycle of Erosion. *American Journal of Science*, 255, 161-174.

Schwarz , F.W. and H. Zhang. 2002. *Fundamentals of Groundwater*. John Wiley and Sons Inc: New York, 583 pp.

Shannon, J., R. Richardson, and J. Thornes. 2002. Modelling Event-based Fluxes in Ephemeral Streams. In: L.J. Bull and M.J. Kirkby (Eds.), *Dryland Rivers: Hydrology and Geomorphology of Semi-arid Channels*, John Wiley and Sons: New York, 129-172.

Shields, F.D., S.S. Knight, and C.M. Cooper. 1998. Rehabilitation of aquatic habitats in warmwater streams damaged by channel incision in Mississippi. *Hydrobiologica* 382 (1-3), 63-86.

Shuttleworth, W.J. 1979. *Evaporation*, Report 56, Institute of Hydrology, Wallingford, U.K, 63 pp.

Simcox, A.C. 1983. The Rio Salado at Flood. *New Mexico Geological Society Guidebook*, 34th Field Conference, 325-337.

Simon A. and S.E. Darby. 1999. The Nature and Significance of Incised River Channels. In: Darby, S.E. and A. Simon (Eds.), *Incised River Channels*, John Wiley and Sons: New York, 19-33.

Stensrud D.J., R.L. Gall, S.L. Mullen, and K.W. Howard. 1995. Model Climatology of the Mexican Monsoon. *Journal of Climate*, 8(7), 1775-1794.

Stensrud D.J., R.L. Gall, and M.K. Nordquist. 1997. Surges over the Gulf of California during the Mexican Monsoon. *Monthly Weather Review*, 125, 417-436.

Tarboton, D. G., R. L. Bras, and I. Rodriguez-Iturbe. 1991. On the Extraction of Channel Networks from Digital Elevation Data. *Hydrologic Processes* 5(1), 81-100.

Tarboton, D. G. 1997. A New Method for the Determination of Flow Directions and Contributing Areas in Grid Digital Elevation Models. *Water Resources Research*, 33(2), 309-319.

Thornthwaite, C,W., C.F.S. Sharpe, and E.F. Dosch. 1942. *Climate and Accelerated Erosion in the Arid and Semi-arid Southwest, with special reference to the Polacca Wash Drainage Basin, Arizona*. U.S. Department of Agriculture Technical Bulletin, 108, 134 pp.

Tucker G.E., S.T. Lancaster, N.M. Gasparini, R.L. Bras, and S.M. Rybarcyk. 2001. An object-oriented framework for distributed hydrologic and geomorphic modeling using triangulated irregular networks. *Computers and Geosciences*, 27, 959-973.

Tsai, V. J. D. 1993. Delaunay Triangulations in TIn Creation: An Overview And a Linear-Time Algorithm. *International Journal of Geographic Information Systems*, 7(6), 510-524.

USGS National Water Information System. 2007. http://waterdata.usgs.gov/nwis.

USGS Seamless Data Distribution System, Earth Resources Observation and Science (EROS) 2007. http://seamless.usgs.gov

Vivoni, E.R., V.Y. Ivanov, R.L. Bras, and D. Entekhabi. 2004. Generation of Triangulated Irregular Networks Based on Hydrological Similarity. *Journal of Hydrologic Engineering*, 4, 288 - 302.

Vivoni, E.R., V.Y. Ivanov, R.L. Bras, and D. Entekhabi. 2005. On the Effect of Triangulated Terrain Resolution on Distributed Hydrologic Modeling, *Hydrological Processes* 19(11), 2101-2122.

Vivoni, E.R., R.S. Bowman, R.L. Wyckoff, R.T. Jakubowski, and K.E. Richards. 2006. Analysis of a monsoon flood event in an ephemeral tributary and its downstream hydrologic effects. *Water Resources Research*, 42(3), W03404, doi: 10.1029/2005WR004036,

Wagener, T., D.P. Boyle, M.J. Lees, H.S. Wheater, H.V. Gupta, and S. Sorooshian. 2001. A framework for development and application of hydrological models. *Hydrology and Earth System Sciences*, 5(1), 13 - 26.

Williams, W.A., M.E. Jensen, J.C. Winne, and R.L. Redmond. 2000. An automated technique for delineating and characterizing valley-bottom settings. *Environmental Monitoring and Assessment*, 64, 105-114.

Wilcox, B.P., B.D. Newman, D. Brandes, D.W. Davenport, and K. Reid. 1997. Runoff from a semi-arid ponderosa pine hillslope in New Mexico. *Water Resources Research*, 33, 2301 - 2314.

Wigmosta, M.S., S.L.W. Vail, and D.P. Lettenmaier. 1994. A distributed hydrology-vegetation model for complex terrain. *Water Resources Research*, 30, 1665-1679.

Xie, H., X. Zhou, E.R. Vivoni, J.M.H. Hendrickx, and E.E. Small. 2005. GIS-based NEXRAD Stage III precipitation database: automated approaches for data processing and visualization. *Computers and Geosciences*, 31, 65-76.

Xie, H., X. Zhou., J.M.H. Hendrickx, E.R. Vivoni, H. Guan, Y.Q. Tian, and E.E. Small. 2006. Evaluation of NEXRAD Stage III Precipitation Data Over A Semiarid Region. *Journal of the American Water Resources Association*, 2, 237-256.

Zhang, W. and D. R. Montgomery. 1994. Digital Elevation Model Grid Size, Landscape Representation, and Hydrologic Simulations. *Water Resources Research*, 30(4), 1019-1028.